Influence of cooling rate on microsegregation behavior of magnesium alloys

Md. Imran Khan

A thesis submitted in partial fulfillment

of the requirements for the degree of Master of Applied Science (Mechanical Engineering) at

Concordia University

Montreal, Quebec, Canada

August 2013

ABSTRACT

Influence of cooling rate on microsegregation behavior of magnesium alloys

Md. Imran Khan

Magnesium castings are widely used in automotive sector due to their high strength to weight ratio. Solidification of these alloys always results in inhomogeneous distribution of alloying elements (microsegregation), which can have adverse effect on the microstructure. To control the microstructure obtained from different solidification conditions, and thus attain desired properties, in-depth understanding of microstructure evolution and the resulting microsegregation is of paramount importance.

The effect of cooling rate on microstructure and microsegregation of three commercially important magnesium alloys was investigated in the current research. Wedge ('V' shaped) castings of AZ91D, AM60B and AE44 alloys were made using water cooled permanent copper mold to obtain range of cooling rates from a single casting. Variation of microstructure and microsegregation was studied using a combination of experiments and thermodynamic modeling. Chemical inhomogeneities of alloying elements in dendritic length scale at different cooling rates were examined using scanning electron microscope. Solute redistribution profiles were drawn from the experimentally obtained data and then compared with established models. Microstructural and morphological features such as dendrite arm spacing, secondary phase particle size were also analyzed using both optical and scanning electron microscopy. Thermodynamic calculations were performed using FactSage to obtain data regarding two solidification extremities- equilibrium and non-equilibrium Scheil cooling. Dendrite arm spacing and secondary phase particle area have an increasing trend with decreasing cooling rate for the

three alloys. Area percentage of secondary phase particles decreased with decreasing cooling rate for AE44 alloy. The trend was different for AZ91D and AM60B alloys, for both alloys, area percentage of β-$Mg_{17}Al_{12}$ increased with decreasing cooling rate up to location 4 and then decreased slightly. Microsegregation tendency was more severe at slower cooling rate, possibly due to prolonged back diffusion. At slower cooling rate, the minimum concentration of aluminum at dendritic core was lower compared to faster cooled locations. Segregation deviation parameter and partition coefficient were calculated from the experimentally obtained data. These data would be valuable input for solidification modeling of microstructure of these alloys and can also be used to validate present models.

ACKNOWLEDGMENTS

First and foremost I would like to express my sincere gratitude and appreciation to my supervisor Dr. Mamoun Medraj for his patience in guiding me throughout the course of this thesis and for providing financial support. I would also like to thank Dr. Mohammad Jahazi for his small but important suggestion, which helped me to focus on this particular aspect of research.

The financial support from AUTO21 is gratefully acknowledged. I would also like to thank my group mates, past and present, for their help in different phases of my research. The names I should mention, Md. Mezbahul Islam for helping in FactSage learning, Nazmul H Khan, Shabnam Konica, Abu Syed Humayun Kabir for teaching me how to polish samples perfectly, Mohammad Shamekh, Ahmad Omar Mostofa, Guy Joel Rocher, and Wei Chen. Special thanks to Dr. Dmytro Keverkov and Dr. Pampa Ghosh. And last but not the least; Mazen Samara deserves heartfelt thanks for maintaining the lab supplies.

Very special thanks to Ahmad Omar Mostafa, for all his supports. For ruining his weekends to assist me in my experimental works. Any problems I had; be it related to academic life or not, he was always ready to help with his warm smile.

Finally, I would like to thank my parents and siblings, for their unblemished love and support from more than 12,000 kilometers distance. And special thanks to my wife Tammeen Siraj for helping me in formatting my life and this thesis.

Table of content

List of Figures

List of Tables

Chapter 1 **Introduction**

Though magnesium was discovered almost two hundred years ago, only the last two decades saw the boom of magnesium alloys. Environmental concern was the key motivating factor behind this escalation. The world, abode of approximately 6.91 billion people, is getting warmer due to global warming which will eventually lead to many natural disasters. Burning of fossil fuels and deforestation are liable for the increasing concentration of greenhouse gases. A significant amount of fossil fuel is burnt by automobiles. The equation is simple, reduce the fuel consumption and the pollution will be less. Better aerodynamic design of the vehicles or engines with improved combustion efficiency can lessen fuel consumption but weight reduction seems to be the most effective way to achieve a substantial fuel saving [1, 2]. According to automotive designers and engineers, for any given vehicle, ten percent reduction in vehicle weight will ultimately result in six to eight percent drop in fuel consumption [3].

When lightness is the key, magnesium takes the centre stage. With a density of 1.74 g/cm^3, it is the lightest of all the engineering structural metals [4]. Magnesium's close competitor, aluminum has a density of 2.7 g/cm^3 and steel is almost five times heavier than magnesium with a density of 7.86 g/cm^3 [5]. Magnesium has the highest strength-to-weight ratio of all structural metals. Magnesium alloys have an excellent combination of properties which justifies their usage in transportation applications. These properties include excellent strength-to-weight ratio, good fatigue and impact strengths, and relatively large thermal and electrical conductivities [6].

All the commercial magnesium alloys are multicomponent and they form a variety of phases during solidification and subsequent processing stages. The casting process determines shape and distribution of the different phases. Magnesium alloy components are usually produced by various casting processes, among them the most applicable methods are high-pressure die casting and gravity casting, particularly sand and permanent mold casting. Other pertinent production technologies include: squeeze casting, thixocasting and thixomolding [3]. The wide ranges of operational conditions existing in foundry and casting processes generate, as a direct consequence, a diversity of solidification microstructures. Because microstructure determines the final properties of the material, proper understanding of the microstructure formation mechanism is extremely important. Detailed understanding of microstructure formation and reliable databases for all the relevant properties will allow the designers to control the solidification conditions via deliberate selection of alloy composition and processing parameters, so that the intended level of mechanical strength required for particular applications could be attained. Such a knowledge-based approach will improve the efficiency in industrial arena by reducing the cost and time of product development.

After casting, metallic alloys are generally used in one of the four conditions: as-cast, heat treated, mechanically worked, and worked and heat treated. In all cases, the casting process has a significant influence upon the mechanical properties, especially in the former two cases. Mechanical properties depend on the microstructural arrangement defined during solidification such as the amount and distribution of eutectic phases, grain size, dendrite spacing, and porosity [7]. Segregation or redistribution of solutes during solidification is closely linked with dendrite spacing, interdendritic porosity, and the

amount and distribution of eutectic phases. It is evident from the literature review that there have been very few experimental investigations to study the influence of cooling rate on microsegregation in magnesium alloys. The mechanism of microsegregation during solidification of aluminum alloys has received considerable attention but microsegregation during solidification of magnesium alloys has not been systematically studied.

1.1 Objectives

To understand the influence of cooling rate on microsegregation of magnesium alloys, the aim of this thesis is to carry out experimental investigation using wedge cast samples of AZ91D, AM60B and AE44 alloys. By applying wedge casting solidification technique, it is possible to produce a range of cooling rates in one casting.

The specific objectives of this research are

- to measure the variation of microsegregation with cooling rate,
- to measure the area percentages of phases formed during solidification using quantitative image analysis,
- to measure the weight percentages of phases formed at different cooling rates using XRD,
- microstructural mapping, and
- to examine the variation in microhardness due to microsegregation.

Chapter 2 **Literature Review**

The following literature survey is focused on segregation, specifically on microsegregation. Microsegregation is intimately linked with dendrite arm spacing and formation and distribution of secondary phases. These topics are also addressed.

2.1 Mg-Al alloys

Magnesium is very soft in its pure form. For structural applications, magnesium is alloyed to obtain required strength, ductility, corrosion resistance and castability. Magnesium alloying elements can be grouped into two categories:

Elements that actively influence the melt: They are added in relatively small quantities and extensive solubility in the melt is not required. Beryllium and manganese fall in this group.

Elements that modify the microstructure of the alloy: These elements must be relatively soluble in liquid magnesium. Commercially interesting alloying elements include aluminum, cerium, copper, lanthanum, lithium, manganese, neodymium, silver, yttrium, zinc, calcium, strontium, and zirconium [8].

Main commercial magnesium alloys include AZ series (Mg-Al-Zn), AM series (Mg-Al-Mn), AE series (Mg-Al-RE), EZ series (Mg-RE-Zn), ZK series (Mg-Zn-Zr), WE series (Mg-RE-Zr), AS series (Mg-Al-Si), AX or AXJ series (Mg-Al-Ca), and AJ series (Mg-Al-Sr) [1, 9].

For automotive applications, alloys of AM and AZ series are mainly used. AZ91D is the most widely used magnesium die-casting alloy. It has good combination of room-temperature strength and ductility, good salt-spray corrosion resistance and excellent die-

castability. Introduction of the high ductility, energy absorbing alloys in the AM-series is a major driving force behind the expansion of the automotive use of magnesium die-castings. These alloys are used for components that are subjected to deformation during a crash. Examples of applications include steering wheel cores, instrument panel substrates, seats, doors, and body parts. The lower aluminum content of AM20 compared with AM50 and AM60 results in increased elongation and impact strength with reduced yield and tensile strength as well as substantially reduced flow and die-filling abilities [5].

For powertrain applications, specifically for the transmission case and the engine block, high creep resistance is required at elevated temperature (150-200°C) [10]. The alloys of AM and AZ series do not possess the required elevated temperature properties. This is mainly due to the formation of brittle β-$Mg_{17}Al_{12}$, as the poor creep resistance of Mg-Al alloys is generally attributed to the poor thermal stability of this phase at elevated temperatures [11] and its incoherency with the hcp matrix. To increase the creep resistance at elevated temperature it is mandatory to suppress the formation of β-$Mg_{17}Al_{12}$ and alloying should be done in such a way so that stable second phase particles form at grain boundaries and microstructural stability of the alloy is increased through a reduction in the amount of supersaturated α-Mg that could decompose during elevated service temperature [12]

AE series alloys have good creep resistance properties. These alloys are based on addition of 2 to 5% rare earth elements to Mg-Al binary alloys. The rare earth elements are either added as misch-metal (natural mixture of rare earth elements) or as individual elements. Usually misch-metal is considered for economic reasons as it is cheaper than individual elements. The general assumption is that all of the elements found in misch-

metal behave in the same way when added to Mg alloys. That is why the symbol E is used to denote all RE elements in the standard alloy nomenclature [13]. The required reduction in solute aluminum occurs as a result of the formation of aluminum consuming Al–RE phases (Al_4RE, Al_3RE, $Al_{11}RE_3$) during solidification. The addition of RE elements improves corrosion resistance but reduces castability. These alloys have good creep properties up to 150°C but the creep resistance is degraded at engine operating temperatures (200-250°C) [1].

Rare earth elements are costly, hence search is going on for cheaper alternatives. Addition of silicon to Mg-Al binary alloys forms the basis of AS series. The formation of Mg_2Si phase pins the grain boundaries and improves creep resistance above 150°C but not at ambient temperatures. Though the creep resistance is marginally improved by Si addition, the corrosion resistance of these alloys is not up to the mark. Another alternative is adding Ca to Mg-Al, which is the basis of AX or AXJ series. Calcium is very reactive and forms thermally stable Al_2Ca, and Mg_2Ca which provide effective grain boundary strengthening at a low cost. But the corrosion resistance of these alloys decreases with increasing amount of calcium.

The increasing demand for light weight vehicles is the major driving force behind the renewed interest in magnesium. However, there is also significant growth in applications for instruments related to communications, computers and cameras (popularly known as 3C) and handheld tools. Structural applications for magnesium include aerospace, automotive, nuclear, and sporting goods. Magnesium is also being used in biomedical applications. As magnesium is biocompatible and bio-degradable, it can be used in

repair surgery for bone and dental implants, allowing bone tissue to regenerate without the need for a second surgery to remove the repair implant [2].

Extensive research is being carried out to expand the knowledge of the interactions between forming processes, components design, and component function/properties. However, this knowledge is less comprehensive than desirable, particularly for the new alloys.

2.1.1 Competency of magnesium alloys

The potential competitors of magnesium alloys are aluminum alloys, plastics, and various composites. The raw material cost is higher for magnesium in comparison to aluminum but there are other important factors to be considered. Magnesium alloys are easily castable and able to hold tighter tolerance than aluminum. "Components can be cast at 1.0 to 1.5mm wall thickness and 1 to 2 degree draft angles, which are typically ½ that of aluminum [14]." It requires less time to die-cast magnesium in comparison to aluminum, so it would be possible to produce more parts per hour.

"Magnesium can be machined faster and has the best strength-to-density ratio of any of the commonly used structural metals. Magnesium's superior machinability allows the use of high speeds and heavy feeds, which result in fewer machines, less capital investment, less floor space, and less labor overhead requirements than aluminum. Low cutting pressures, high thermal conductivity, and rapid heat dissipation providing four to five time greater tool-life and less "downtime" than aluminum. Magnesium's lack of affinity for tool steel allows the die-cast tools to last roughly two times longer than aluminum. [15]"

Due to high fluidity of molten magnesium it is possible to cast complex and fine detailed components. The relatively low heat content results in reduced thermal distortion. This, coupled with its lower density, enables close tolerances to be held and allows designers to incorporate more features. A steel cross-car beam instrument panel has more than 35 different parts while a comparable die cast magnesium instrument panel contains only 5 parts [14].

Although polymeric materials have comparable density, magnesium has better mechanical properties, better electrical and thermal conductivity [16]. In addition, the ease of recycling, compared with polymers, makes magnesium alloys environmentally attractive [17].

2.1.2 Solidification of magnesium Alloys

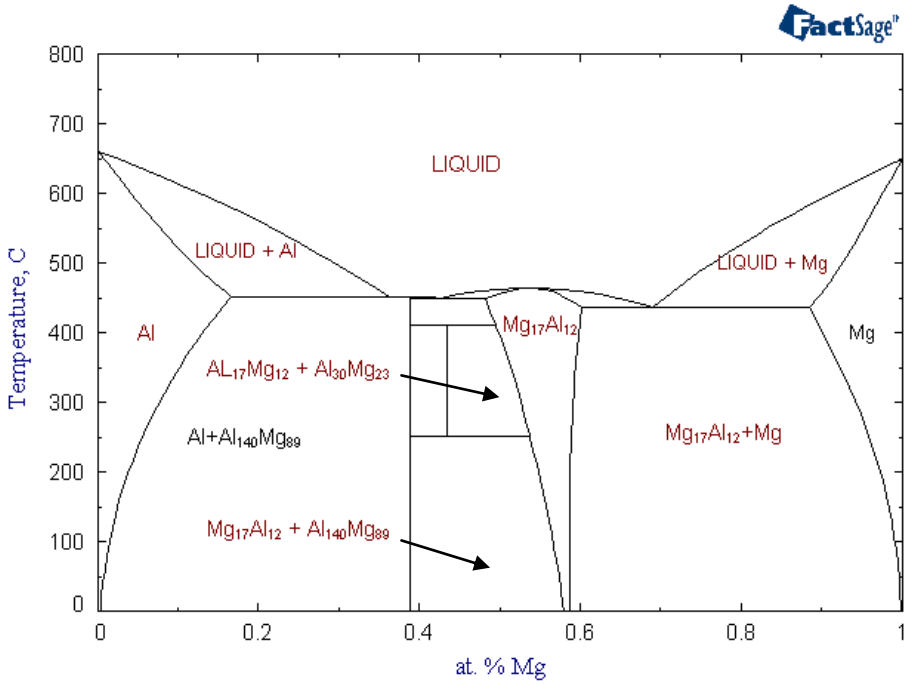

Figure 2-1: Mg-Al binary phase diagram

Most of the commercial magnesium alloys are based on magnesium-aluminum (Mg-Al) system. Hence, understanding of the Mg-Al binary phase diagram is vital for predicting equilibrium phase development of different alloys. The solubility curve of the binary Mg-Al alloys displaces slightly with addition of manganese or zinc. Commercial magnesium casting alloys contain 2–9 wt.% aluminum. The Mg-rich section of the binary phase diagram reveals a maximum solid solubility of 12.9 wt.% Al at the eutectic temperature of 437 °C and α-Mg/β-$Mg_{17}Al_{12}$ eutectic appears at about 33 wt.% Al. Most of the commercial Mg-Al alloys are hypoeutectic alloys and have aluminum content below the maximum solid solubility. Under equilibrium conditions, the Mg–Al casting alloys should solidify as single phase α-Mg solid solution. However, the presence of metastable β-$Mg_{17}Al_{12}$ in as-cast microstructure of Mg-Al alloys suggest that, equilibrium solidification almost never takes place in any of the commercial casting processes [18].

There are three types of growth morphologies that are commonly observed in the mushy zone of a solidifying alloy- planar, cellular, and dendritic. The dendritic growth pattern, which is predominant in normal casting conditions, can be divided into two types- columnar and equiaxed. Since magnesium has a hexagonal-close-packed (HCP) crystal structure, dendrite arms may branch with a six-fold symmetry [18].

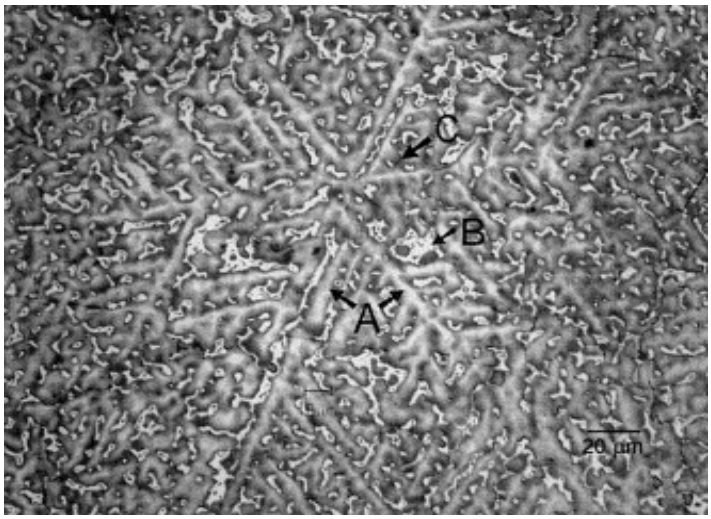

Figure 2-2: Micrograph of fully developed dendrite in magnesium alloy with six-fold symmetry (A). The white phase between the dendrites is secondary eutectic phase $Mg_{17}Al_{12}$ (B) and the dark regions between the dendrites are aluminum-rich solid solution (C) [18].

Non-equilibrium solidification begins with the nucleation of primary α-Mg phase. As solidification progresses, the liquid between dendrites gets enriched with solute due to solute rejection or segregation. Segregation takes place due to unequal solute diffusion rates in the solid and the liquid phases of the solvent material. As a result, the phases that solidify in the later stages of the solidification process, such as β-$Mg_{17}Al_{12}$, are placed between dendrite arms. Due to segregation or coring, the outer layers of α-Mg dendrites become richer in aluminum than the preceding one. The aluminum concentration gradually changes in the inter-dendritic region as some of the aluminum atoms react to form β-$Mg_{17}Al_{12}$ phase and the peak in the aluminum concentration occurs at the instant before the β-$Mg_{17}Al_{12}$ phase precipitates [18].

Depending on the alloy's composition and cooling rate, the β-$Mg_{17}Al_{12}$ phase exhibits a wide range of morphology. The morphology may be in the form of fully divorced, partially divorced, granular, fibrous, and lamellar. Nave et al. [19] reported that the cooling rate may affect the morphology of the eutectic by changing the morphology of the primary dendrites. Change of cooling rate will also influence the number of nucleation sites, solute contents in the dendrites, and the gradient of solute distribution in the liquid ahead of the growing dendrites. Hence, the size, shape and distribution of the β-$Mg_{17}Al_{12}$ phase in the solidified microstructure are strongly correlated with cooling rate.

2.1.3 Dendrite arm spacing

Dendritic structure is a common feature observed in metals and alloys. The growth pattern of dendrites varies from pure metals to alloys. During solidification, the failure of liquid-solid interface to maintain a 'plane front' results in dendrites [20]. The main reasons for this type of growth are the presence of impurities in the alloy, segregation of solute, local disturbances and variations in temperature gradient and solidification rate [21]. Dendrite arm spacing (DAS) usually refers to the spacing between the secondary arms of the dendrites. However, if tertiary arms are present at a smaller spacing, then it would refer to this. Alternatively, if no secondary arms are present, which is very rare, the spacing would be that of the primary dendrite stems [22]. The secondary dendrite arm spacing controls the size and the distribution of porosity and intermetallic particles in the casting. As DAS becomes smaller, porosity and second phase constituents are dispersed more finely and evenly. This refinement of the microstructure leads to considerable

improvement in mechanical properties. The tensile properties most affected by variations in DAS are ultimate tensile strength and percent of elongation [22].

A number of studies have pointed out the effect of microstructure, and particularly of dendrite spacing, on mechanical properties [23-26]. Dendrite fineness is regarded as most important structural length parameter for the prediction of mechanical properties in cast alloys but in the metallurgy of wrought materials, it is the grain size of the alloy that is usually the important structural feature. The improved mechanical characteristics of cast structures having smaller dendrite spacings are due largely to the shorter wavelength of the periodicity of the microsegregation.

Mechanical properties of most cast alloys are seen to be strongly dependent on secondary arm spacing. As DAS decreases, consequently ultimate strength, ductility and elongation increase. Close to the chill the strength of the alloy is high and the toughness is good. As the cooling rate is decreased (and the DAS grows), the ultimate strength falls.

Because of the strong correlation between section thickness and DAS, the effect of section size on mechanical properties is seen to be important. There had been some works to relate the section thickness of magnesium alloys to mechanical properties [27-29]. The change of thickness means the cooling condition during solidification is also different, affecting the microstructure and therefore the mechanical properties.

The improvement of strength and toughness by a reduction in DAS is quite often confused with or considered similar to the effect of grain refinement. According to Campbell [22], the effects cannot be the result of the same mechanisms. This is because there is no grain boundary between the arms of a single dendrite to stop the slide of a slip plane. A dislocation will be able to run more or less without hindrance across arm after

arm, since it will be part of the same crystal lattice. Thus in general, it seems that the Hall-Petch equation should not apply. Classical physical metallurgy has been unable to explain the effect of DAS on mechanical properties. As Campbell [22] explains that the DAS is merely the indicator of the time available for the opening of the bifilms. It is the opening of the bifilms into expansive planar cracks that is important.

It is now known that DAS is controlled by a coarsening process in which the dendrite arms first grow at very small spacing near the tip of the dendrite. As time goes on, the dendrite attempts to reduce its surface energy by reducing its surface area. Thus small arms preferentially go into solution while larger arms grow at their expense, increasing the average spacing between arms. The rate of this process appears to be limited by the rate of diffusion of the solute in the liquid as the solute transfers between dissolving and growing arms.

2.2 Segregation

The chemical heterogeneity which results due to redistribution of solutes during solidification of an alloy is known as segregation. If the segregation is in the length scale of dendrite arms or a few grains, it is called microsegregation. For macrosegregation the length scale varies from a few millimeters to a few centimeters. The mechanical property and corrosion resistance of an alloy can be significantly affected by microsegregation [30]. Hence it is very important to understand the microsegregation pattern of an alloy, so that the solidification process can be controlled accordingly to achieve optimum material properties. Numerous experimental and theoretical studies have been carried out to investigate microstructure and microsegregation in binary alloys. Though most of the

commercial alloys are multi-component, the number of research concerning them is limited. Particularly for magnesium alloys there has not been any significant research related to this topic.

When the solubility of the solute element in the solid is lower than that in the liquid, a solute-rich boundary layer builds up at the solid/liquid interface during solidification. Theoretical models of solute redistribution such as the Scheil equation have shown that in alloy systems containing a eutectic reaction, the maximum composition that can be attained by the intercellular liquid is the eutectic composition, even when the initial composition of the alloy in question is hypoeutectic [31]. To summarize, microsegregation controls the microstructure of an alloy system by influencing the following events, growth morphology, solute concentration in solid and liquid, and fraction of non-equilibrium second phases.

Ganesan et al. [32] reported some problems which are caused by the severe segregation of refractory elements during the solidification of the nickel based superalloys,

- Formation of low melting point or brittle phases
- Nonuniform distribution of strengthening precipitates,
- Interdendritic porosity
- Misoriented grains
- Freckle formation
- Solidification cracking, and
- Localized phase instability.

It is possible to address some of these problems by implying long duration stepwise homogenization heat treatments or hot-isostatic pressing but that would increase

production cost and the unresolved problems would result in increased scrap rates. Therefore, when new processes are applied or new alloy chemistries are evaluated, it is usual to characterize the extent of microsegregation. For near net shape castings and welding, where heat treatment is not applicable, it is very important to know the amount of microsegregation.

There are several experimental methods [33] for the measurement of segregation characteristics of an alloy. The most common among them are

- Planar directional solidification
- Equilibrium solidification
- Interrupt quenching
- Dendrite contour mapping
- Eutectic composition measurement
- Random mapping

In planar directional solidification, bar shaped samples are produced which have elemental segregation along the crystal growth direction. To obtain the segregation profile, chemical analysis is done on slices taken from different positions of the bar. For equilibrium solidification and interrupt quenching method, the semisolid structure which occurs at a high temperature during solidification is retained and the elemental partitioning coefficients are obtained by measuring the quenched solid and liquid composition using electron probe micro analyzer (EPMA). In recent years dendrite contour mapping has been used extensively. In this method the sample is directionally solidified, the composition on the transverse section is measured using EPMA and then

the elemental distribution map is drawn, correlating segregation pattern and fraction of solid [33].

2.2.1 Microsegregation measurement techniques and representation

Gungor [34] reported that the extent of microsegregation in an alloy could be determined experimentally by measuring one of the following:

- Amount of nonequilibrium eutectic
- Amount of nonequilibrium second phase
- Minimum solid composition
- Ratio of minimum to maximum composition of the primary phase
- Composition versus fraction solid profiles

Experimental techniques to investigate the extent of microsegregation include quantitative metallography (point count, areal, and lineal measurements), X-ray diffraction analysis [35] and electron microprobe measurements.

An estimation of the volume fraction of second phases could be obtained by metallographic and X-ray diffraction techniques but to obtain the composition minima and local solute redistribution profiles, EPMA should be done [34].

Of the techniques available, the most widely used for characterizing microsegregation is the random sampling approach developed by Flemings et al. [36], commonly known as the point matrix or area scan approach. There is no hard and fast rule about the total number of points to be taken to represent the compositional variability. Gungor [34] reported that at least 100 points are necessary to obtain reasonably accurate result. He showed that the result did not vary significantly if 300 points are taken instead of 100

points. These 100 or more point composition measurements are obtained either along several arbitrarily selected lines or on a grid encompassing several primary dendrite stems from a transverse section of the casting. These are performed by means of scanning electron microscope–energy dispersive spectroscopy (SEM–EDS) or electron microprobe analysis using wavelength dispersive spectrometry (EPMA–WDS).

In the present work SEM-EDS was used for elemental analysis. Compositional measurements were obtained for at least 150 points placed at a rectangular gird of 10×15 at each thermocouple location. This combination of SEM-EDS and 150 points area scan provided reasonably accurate result at convenient machine use.

There has been debate over the best way to gather and represent microprobe data. Line scan or area scan? Usually area scan is preferred because it avoids the subjective selection of a line that traverses regions of maximum and minimum solute concentrations and provides a continuous variation in concentration profiles instead of a few discrete points [32]. There is further practical significance in choosing area scan method for the analysis of weakly cored or homogenized systems where dendritic contrast is less apparent [32].

However area scan method has its drawbacks too. Lacaze et al. [37] and Xie et al. [38] reported that the cumulative representation of microsegregation data of multicomponent alloys can be misleading, as local compositional variations that would otherwise be clearly captured by a typical line scan or X-ray map are lost when each solute composition is individually sorted.

With line-scans, it is possible to obtain the compositional variability along a chosen line. The approach for segregation measurement of columnar and equiaxed grain should be

different. For columnar grains, one should choose to measure the dendrites which are closely aligned with the plane of sectioning and analyze the segregation along a line which crosses several secondary dendrite arms. It is difficult to choose the line direction for equiaxed dendrites, if the primary arms are not long enough. But there might be problems regarding the determination of solute distributions as these results might not represent the actual distribution profile as it is very difficult or nearly impossible to select a line passing through the center of a dendrite. According to Lacaze et al. [37] , line scan is probably the best data format for comparing with microsegregation models considering the segregation between a pair of adjacent dendrite arms.

Other two comparatively less applied methods are compositional maps and segregation ratio. With compositional maps it is possible to present the nature and variability of the dendritic structure and associated microsegregation, but it is not a suitable method for comparing different samples. Segregation ratio usually refers to maximum over minimum or maximum over bulk composition. These are the simplest parameters for comparing different samples but much information is lost. Martorano et al. [39] used a refined segregation ratio, the average deviation between the measurements and nominal composition were reported.

In case of representing the cumulative profiles, there could be errors incorporated, originating from random errors of analysis, local variability of microstructural spacing, and the presence of multiphase structures [37]. Care should be taken when dealing with multiphase systems, sampling of secondary phases can produce artificially high or low concentrations that may potentially lead to misleading results, if the subsequent data treatment is attempted without care.

Considering all these factors, area scan method was applied in the present work. As the samples were not directionally solidified hence it was difficult to identify perfect dendritic structures at all sample locations which is a prerequisite for applying line scan method.

2.2.2 Sorting methods

The data points obtained through EPMA are sorted into increasing or decreasing order depending on their segregation behavior to produce composition versus solid fraction profiles for each element. The problem with this kind of profiling is, though it gives a global view about the compositional variation but information regarding the sampling location is lost. Another problem is, it fails to maintain the association between all measurement data taken from a specific region. These curves represent microsegregation profiles from the first to last solidified regions based on the assumption that the solid concentration at the liquid/solid interface varies continuously with fraction solid and back-diffusion during solidification and interdiffusion during cooling can be ignored [37].

Other approaches, that partially overcome some of these problems, such as sorting all the measurements based on composition of a single component (single-element sorts) or sorting based on the compositional difference between two solutes (difference sorts). Yang et al. [33] reported that sorting based on primary alloying elements can produce more accurate elemental partition coefficients. However, the main weakness of both techniques lies in the appropriateness of the choice of the elements upon which to base

the sort; for a 10-component alloy, there are 90 different permutations of the difference sorts to consider [32].

Ganesan et al. [32] proposed an alloy independent sorting algorithm. They termed it weighted interval ranking sort (WIRS). In this approach, all elements present at each data point are considered along with the measurement errors accrued during data treatment. By applying this approach for segregation profiling of Ni-based alloys, they demonstrated that this sorting method treats eutectic constituents appropriately and noise in the segregation profile is also more accurately distributed.

WIRS method was applied in this work as this alloy independent sorting method could accurately treat the eutectic constituents of the three investigated multicomponent alloys.

2.2.3 Considerations for analysis and interpretation

Some issues should be carefully monitored during collection, analysis and interpretation of microsegregation data. Firstly, the pattern of data collection would be different based on the purpose of the investigation. Usually the typical features of interest are the maxima, minima and profiles of composition on the dendritic scale. Thus, data from many dendrites are obtained and averaged. In most cases, it is assumed that the sample under investigation does not present any long range variations; it is homogeneous apart from at the microscopic scale. For directionally solidified structures the plane selected for studying is either parallel or perpendicular to the growth direction, while in case of equiaxed structure any plane of section should be suitable [37].

Secondly, the laboratory experiments performed to investigate the overall solidification kinetics and the development of microstructure and associated microsegregation are

generally designed to operate under controlled thermal conditions and these conditions are totally different from industrial casting conditions. Another concern is, although the dendrites and their variable segregation are 3D phenomenon but microsegregation is commonly measured on a 2D section [37]. These issues should also be considered while interpreting microsegregation data, as they could be the reason of discrepancy between experimental results and theoretical predictions.

Thirdly, it is well established that the dendritic scale and associated microsegregation depend on the cooling conditions. But as mentioned earlier that industrial casting condition is totally different from controlled laboratory conditions. Thus sufficient precautions must be exercised in this regard when devising an experiment to imitate industrial experience. In particular, the cooling conditions are quite often normalized in terms of a cooling rate, but it should be emphasized that it should be called heat extraction rate rather than cooling rate and it is really difficult to achieve a constant cooling rate. Though particular conditions are applied to yield constant cooling rate, departures from a constant cooling rate during solidification is very likely to take place [37].

Sasikumar et al. [40] reported that the general convention of representing cooling conditions by local solidification time or average cooling rate in the solidification interval might be misleading.

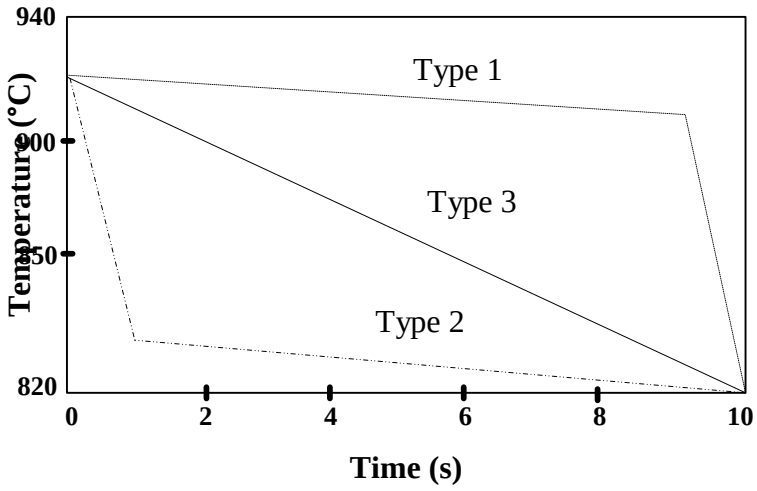

Figure 2-3: Schematic diagram showing the effect of the shape of the three types of cooling curves on microsegregation [40]

In Figure 2-3, although these three cooling curves will give the same average cooling rate but significant variation in dendrite arm spacing and volume fraction of eutectic was observed by Sasikumar et al. [40]. Despite of having similar solidification time, the curves of type 1 give rise to more coarsening and less homogenization than the curves of type 2 because it stays at higher temperature for longer time. Hence, Sasikumar et al. [40] suggested that, "If microsegregation is significantly affected by the shape of the cooling curves, any function or curve or table showing the relationship between any of the microsegregation parameters and local solidification time should be accompanied by a specification of the cooling curves for which these relationships are valid [40]".

2.2.4 Microsegregation measurement in magnesium alloys

Very few experimental works [41-44] regarding the microsegregation analysis of magnesium alloys were found in the literature. In contrary, several studies were carried

out to investigate the solidification behavior of magnesium based alloys. Although the prime focus of these studies were not on microsegregation analysis but valuable information regarding elemental composition at different cooling rates and conditions could be obtained from them. Mirković et al. [42, 43] studied the microsegregation of alloys AZ31 and AM50 alloys, applying directional solidification technique. They reported that the segregation behavior of manganese is opposite compared to both aluminum and zinc. Zhang et al. [44] studied the microsegregation in directionally solidified Mg-4Al binary alloy. They determined microsegregation in specimens directionally solidified with cooling rates ranging from 0.06 to 0.8 K/s. They reported that the concentration profile of Al at high growth rate or higher cooling rate is closer to the Scheil model. Zheng et al. [41] investigated the microsegregation pattern of Mg-4Al-4Ca alloy under different growth rates using directional solidification technique. They suggested that Scheil model can be used in microstructure simulation of this alloy as the microsegregation of the alloying elements (Al and Ca) predicted by this model agreed reasonably well with the EPMA measurements. Wei et al. [45] did the microstructural characterization of several magnesium alloys in the AM series in as cast condition. They performed quantitative analysis of the Al segregation in the die cast alloys by examining thin foil specimens in the TEM. Compositional measurements across an α-Mg grain in AM50A at interval of 180 nm were performed using X-ray energy dispersive spectrometry (EDS) in the TEM along a straight line. They found that the Al composition in the interior of Mg grain was approximately 1.5 wt.% which increased to 3.0 wt.% in the area adjacent to the grain boundaries. They repeated the same procedure for a thin foil sample of die cast AM60A at intervals of 600 nm. The Al content varied from 2 wt.% in

the grain interior to approximately 4 wt% in the Al-rich grain boundary region. The width of the high Al region was about 2–3 mm. They also reported that owing to low Al content no β-$Al_{12}Mg_{17}$ formed in AM20 but there was intergranular Al segregation. Barbagallo et al. [46] determined the variation of the alloying elements content through the grain boundaries of an HPDC AM60 alloy by means of EPMA line scanning and reported that Al concentration varied from 2.5 wt.% in the bulk α-Mg core to 10 wt.% in the boundary region. It is to be noted that for the same alloy AM60, Wei at al. [45] and Barbagallo et al. [46] reported different amount of Al content in the grain boundary region, this is due to the fact that the casting conditions of the samples were different. Han et al. [47] reported that for permanent mold casting of AZ91D alloy, in the dendritic center the aluminum concentration is 2.6 wt.% but it is 11.7 wt.% at the dendrite edge, about 4.5 times higher than that in the dendrite center. Zhang et al [48] conducted experiments to compare the amount of microsegregation in permanent mold cast and die-cast AZ91 alloys. They reported that the average concentration of Al and Zn is lower in die casting matrix than in permanent mold casting matrix. Average concentration of Al is 3.3 wt.% and for Zn it is 0.33 wt.%, in permanent mold casting and 3 wt.% Al and 0.22 wt.% Zn in die-cast matrix, which means amount of segregation was more in comparatively fast cooling. Ditze et al. [49] reported for strip casting of AZ91 alloy, the aluminum content increased from 1 wt.% at the center of the dendrite arms where solidification had started to about 2.5 wt.% between the arms where solidification had ended. Guo et al. [50] reported that in AZ80 alloy the regions close to the β -$Mg_{17}Al_{12}$ eutectic phase have higher aluminum contents, the maximum concentration in the dendritic interstice varied between 6.6 wt.% and 7.9 wt.%. They also reported that applying electromagnetic

vibration on the billet; they could increase the value of minimum Al concentration up to 3.5 wt.% from 2.5 wt.%, which is the minimum concentration of Al in the Mg matrix center in conventional die-cast billet. That means, they could reduce the amount of microsegregation by agitating the liquid.

2.2.5 Effect of segregation on mechanical properties and corrosion

Segregation is responsible for the formation and non-uniform distribution of brittle phases. For magnesium alloys, the amount, shape and distribution of the brittle intermetallic compound β-$Mg_{17}Al_{12}$ have strong influence on the mechanical properties and corrosion resistance of cast components. Kleiner et al. [51] investigated the microstructure and mechanical properties of AZ91, AZ71 and AZ80 alloys. They used AZ91 for squeeze casting, AZ91 and AZ71 for new rheocasting and extruded billets of AZ80 for thixocasting. They reported that finely dispersed and isolated β-$Mg_{17}Al_{12}$ particles in squeeze castings result in better mechanical properties, especially ductility, than the continuous network of β-$Mg_{17}Al_{12}$ usually observed in semi-solid processed parts.

Tensile fracture initiates by the cracking of the β-$Mg_{17}Al_{12}$ particles so the volume fraction and distribution of this phase determines ductility. Ductility is enhanced by a decrease in volume fraction of β-phase as well as by a finer dispersion of its particles. The dominant influence of the amount and distribution of β-$Mg_{17}Al_{12}$ on the mechanical behavior of Mg-alloys is further confirmed by fracture toughness measurements. From microscopic investigation of the crack paths, the different fracture behavior of squeeze cast, semi-solid cast and solution heat treated alloys is demonstrated. For squeeze cast

specimen, as there is no continuous network of β-phase, the crack path is quite tortuous [51].

For AZ91 alloys, it has been shown that the β-phase affects corrosion in one of two ways: it either acts as a micro-galvanic cathode, increasing the corrosion rate of the alloy, or it acts as a barrier to corrosion, reducing the corrosion rate [52]. The β-phase acts as barrier, when it is more continuous and finely divided. Corrosion is confined with the grains thus overall corrosion of the alloy is also inhibited [53, 54]. However, when the β-phase is small, occurring as intergranular precipitates, it acts as a micro-galvanic cathode. Therefore, the micro-galvanic corrosion or corrosion resistance is dependent on the anode (α)/cathode (β) area ratio [54].

2.2.6 Microsegregation severity comparison

Although elemental mapping provides valuable information regarding solute redistribution, it is difficult to quantitatively compare these results. Several quantitative indicators, such as segregation ratio, segregation index, fraction of nonequilibrium microconstituent, and segregation deviation parameter have been found in the literature [55, 56].

Segregation ratio and segregation index, these two methods rely on the minima or maxima of an alloying element at a particular location to calculate segregation severity. These calculations might be misleading sometimes as only terminal points of solute profiles are being considered instead of the entire variation.

Poirier [55] proposed segregation deviation parameter method for measuring the severity of microsegregation. This method is better in the sense that the deviation is calculated over the entire range of data.

$$\sigma_m = \frac{1}{nC_0} \sum_{i=1}^{n} |C_i - C_0| \quad (1)$$

In this method, segregation deviation parameter, σ_m is calculated using equation 1. The absolute difference between the composition at any point C_i and the bulk composition C_0 is measured and the sum is taken for all the readings. Then, this summation is divided by the total number of points analyzed and the bulk composition.

Both segregation deviation parameter and segregation index were employed in this work to compare the severity of microsegregation at different locations of the wedge cast samples.

2.3 Analytical microsegregation modeling

Solidification modeling has three major branches, macroscopic modeling, microscopic modeling, and calculation of phase diagram. Microscopic models mainly deal with the state of microstructure, (types, amount and size of microstructural constituents) and microsegregation (local distribution of alloying elements) [57].

Several analytical microsegregation models [35, 58-63] have been found in the literature to model the solute redistribution of alloying elements during dendritic solidification of alloys. In these models, analytical treatment of micorsegregation during solidification is based on the analysis of the mass balance for the solute elements. The simplest formulations are the equilibrium solidification model (lever rule) and Scheil-Gulliver

model, which describes the two extreme cases of ideal equilibrium and non equilibrium, respectively.

In most of the models, mass balance for the solute elements is considered within a simplified geometry such as a plane, cylinder or sphere to describe the growth of dendrite arms. It is obvious from theoretical and experimental evidences that the simplified geometry gives reasonably accurate results for the majority of the alloy systems and solidification processes [37, 64, 65].

With the advent of more sophisticated computing technology and improvement of material databases, the more advanced models (Kraft [64], Du [66], Boettinger [67]) incorporate more realistic variable diffusion properties across the solid-liquid interface.

2.3.1 Equilibrium solidification model

For equilibrium solidification model, as the name suggests, it assumes that state of equilibrium exists at the solid-liquid interface during growth. That means there would be negligible resistance for transportation of atoms between the solid and liquid phases [68].

From Figure 2-4, it is evident that if a single crystal of alloy composition C_0, is cooled to temperature (T^*), which is below the liquidus temperature (T_L), then according to the equilibrium solidification theory, C_L^* and C_S^* would be the respective compositions of liquid and solid at the interface. To describe solidification in these conditions, the equilibrium partition ratio may be defined as:

$$K = \frac{C_S^*}{C_L^*} \qquad 2$$

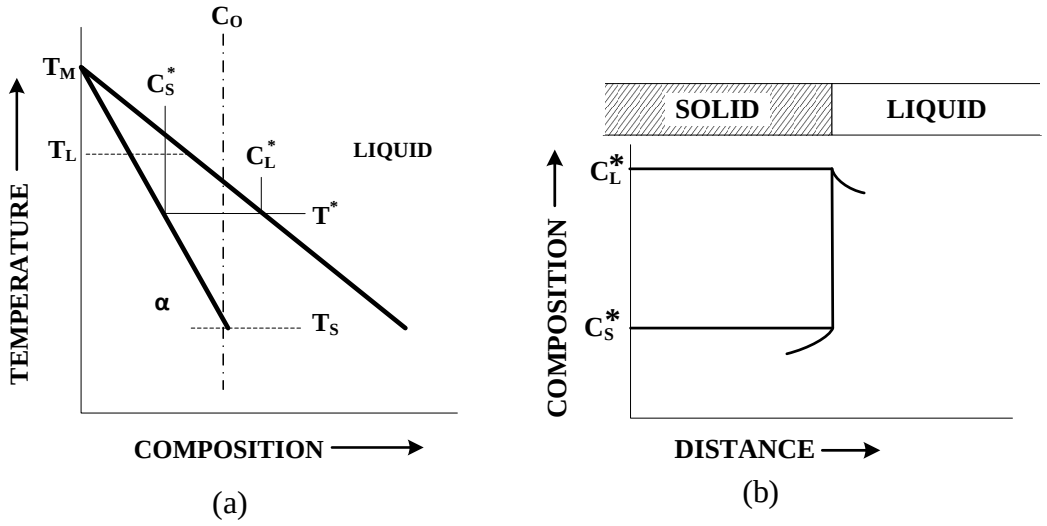

Figure 2-4: Solidification of an alloy with equilibrium at the liquid-solid interface. (a) Phase diagram; (b) composition profile across the interface [68]

The partition coefficient is the ratio of the composition of the solid to that of the liquid. It indicates the degree of segregation of solute. A value less than unity indicates that the element is partitioning preferentially to the eutectic region whereas a value greater than unity indicates that the element is partitioning to the dendrite core. The farther from unity the partition coefficient is the more strongly the element partitions to either the dendrite core or eutectic region. Physical parameters that contribute to the partitioning coefficient are differences in atomic radii (the tendency for an element to be in solution) and the chemical potential of the elements in the liquid.

From Figure 2-5, it could be interpreted that the dependency of liquidus temperature on the changing liquid composition would result in solidification of these alloys over a range of temperature. The first solid would start forming at T_L ; the composition would be KC_0, which means it would be lower in solute compared to initial liquid composition. As the

solidification progresses, the balance of the solute would be rejected enriching the liquid through diffusion. This would eventually result in lower liquidus temperature than that of the initial composition. This solute rejection process is liable for the development of segregation or coring. As a general rule, it can be stated that if the freezing range is larger for an alloy and it gets sufficient time for solute rejection, the segregation severity would be more [69].

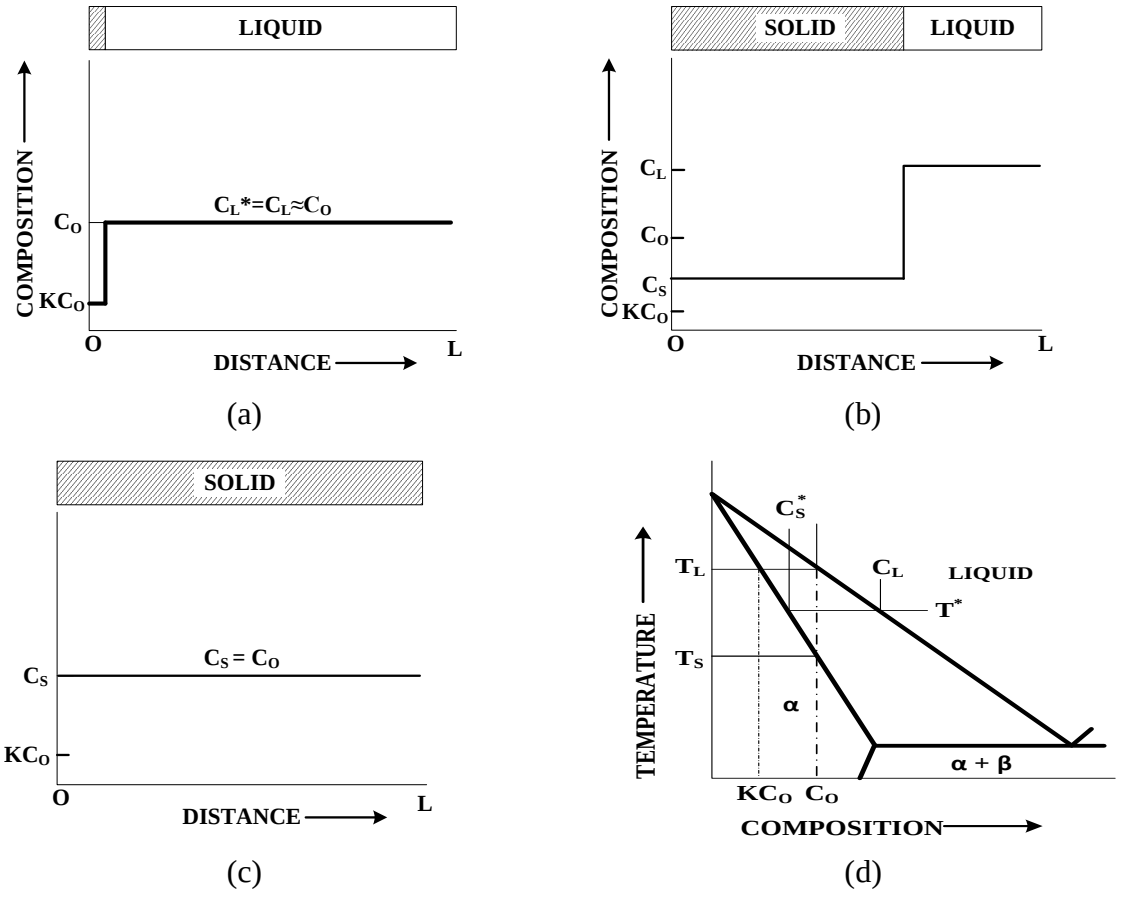

Figure 2-5: Solute distribution in equilibrium solidification of an alloy composition C_0 (a) At start of solidification; (b) at temperature T*; (c) after solidification; (d) phase diagram [68]

Applying the equilibrium lever rule the amount of solute redistribution during equilibrium solidification can be determined by,

$$C_S f_S + C_L f_L = C_0 \quad (3)$$

Here f_Sf and f_L are weight fractions of solid and liquid respectively. The above equation can be written in the following form:

$$C_S = \frac{K.C_0}{(1 - f_S) + K.f_S} \quad (4)$$

This equation describes the composition of the solid phase with respect to the fraction of solid.

Where, C_S is solute concentration in solid (wt. %), C_0 is initial solute concentration (wt. %), K is partition coefficient, and f_S is the fraction solid.

According to the assumption of the equilibrium model, there would be complete diffusion in the liquid and solid phases that means the final product would have a homogeneous composition C_SC=C_0 [68].

2.3.2 Scheil-Gulliver solidification model

Conditions assumed for equilibrium solidification are simply unachievable in real life casting conditions. Scheil-Gulliver model is much more compatible with the general casting process. The assumptions [58] of this model are,

- Negligible undercooling during solidification
- Complete solute diffusion in liquid

- No diffusion in solid
- No mass flow into or out of the volume element
- Constant physical properties
- Fixed volume elements (no dendrite arm coarsening)

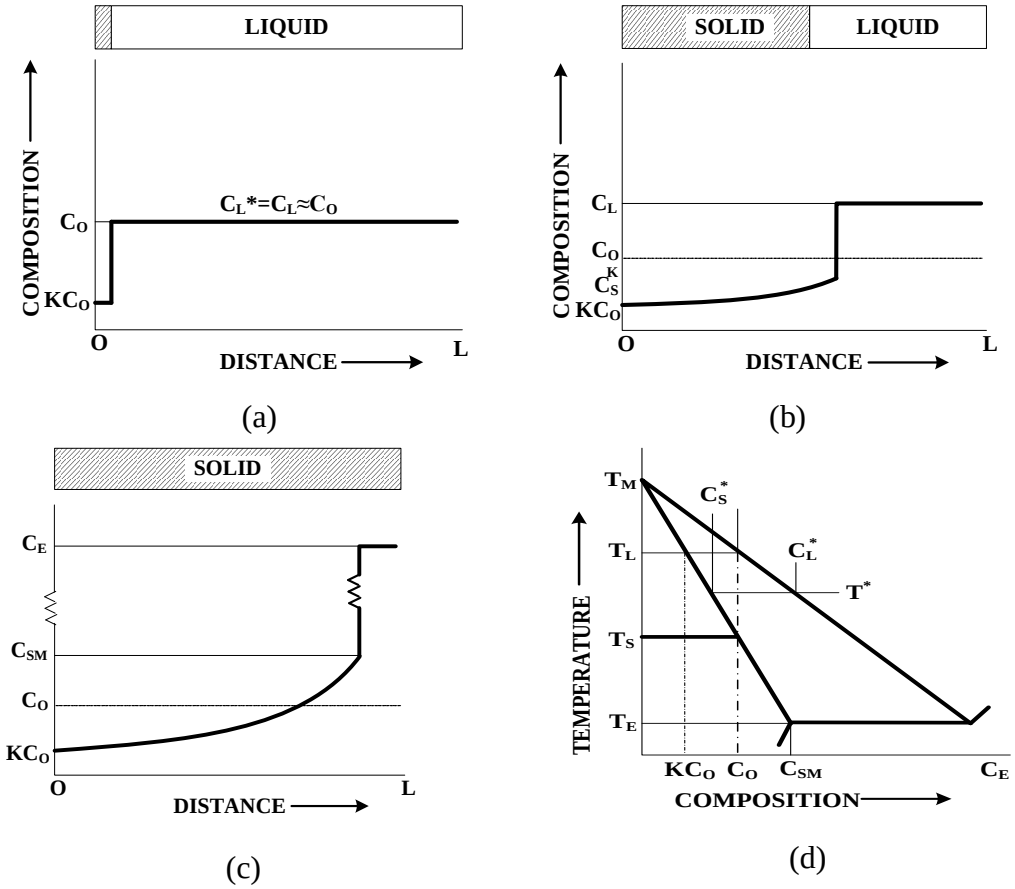

Figure 2-6: Solute redistribution in solidification with no solid diffusion and complete diffusion in the liquid(a) At start of solidification; (b) at temperature T*; (c) after solidification; (d) phase diagram [68]

This model is different from equilibrium model in the sense that it does not allow any elemental diffusion in the solid. That means, once a solid is formed nothing comes out of it or gets in. This would result in a steady rise in rejected solute level in the liquid phase

until the final liquid region has reached the eutectic composition, as shown in Figure 2-6. The famous "non-equilibrium lever rule" or more popularly known as Scheil equation, is as follows:

$$C_S = K.C_0(1 - f_S)^{K-1} \quad (5)$$

2.3.3 Brody-Flemings dendritic solidification model

The work of Brody and Flemings [60] can be considered as the biggest advancement in dendritic microsegregation modeling. They almost perfectly pinpointed the reason for discrepancy between experimental microsegregation measurements and the values predicted by Scheil model. And this mismatch is due to the presence of finite solid-state diffusion in actual castings, whereas Scheil model assumes no diffusion in solid state. Therefore the amount of back diffusion that takes place both during and after the solidification has to be taken into consideration. This back diffusion is liable for lower solute levels than the prediction of Scheil model. The extent of back diffusion is determined by the dimensionless parameter, α, as shown in the integration of the differential solute balance equation for a parabolic growth rate as follows,

$$C_S = KC_0[1 - (1 - 2\alpha K)f_S]^{(K-1)/(1-2\alpha K)} \quad (6)$$

Where,

$$\alpha = \frac{4D_S t_f}{\lambda^2}$$

Here, D_S is the diffusivity in solid (m^2s^{-1}), t_f is local solidification time(s), and λ represent secondary dendrite arm spacing (m). Equation 6, contains two limiting cases

that were described earlier for plane front solidification, when α is set to 0.5, then the equation represents the equilibrium lever rule and when D_S is set to zero (i.e. no solid state diffusion), α becomes zero, and that results in Scheil equation.

There are many other models available in the literature, and the quest for achieving a perfect model is still going on. But, most of these models are modifications of Brody-Flemings model. Kearsey [70] in his thesis came to the conclusion that it is really difficult to make accurate microsegregation prediction using these simplified models, as these models do not take into account the complexity regarding the number of diffusing solute species and their relative interactive efforts that takes place during the solidification of multicomponent alloys.

Research is going on to complete the database for magnesium alloys; diffusivity data for different ternary systems are being experimentally determined. Then it might be possible to predict the microsegregation more accurately using the models with these values incorporated. Till then, it is better to measure the microsegregation experimentally in these alloys and the models should be improved based on these results.

2.4 Microhardness measurement

Microhardness measurement is usually done to distinguish between different hardness regions in the same sample. For microhardness measurement of magnesium alloys, Vickers microhardness is usually applied. The usual applied load is 50 gf for 10-15 seconds [71, 72].

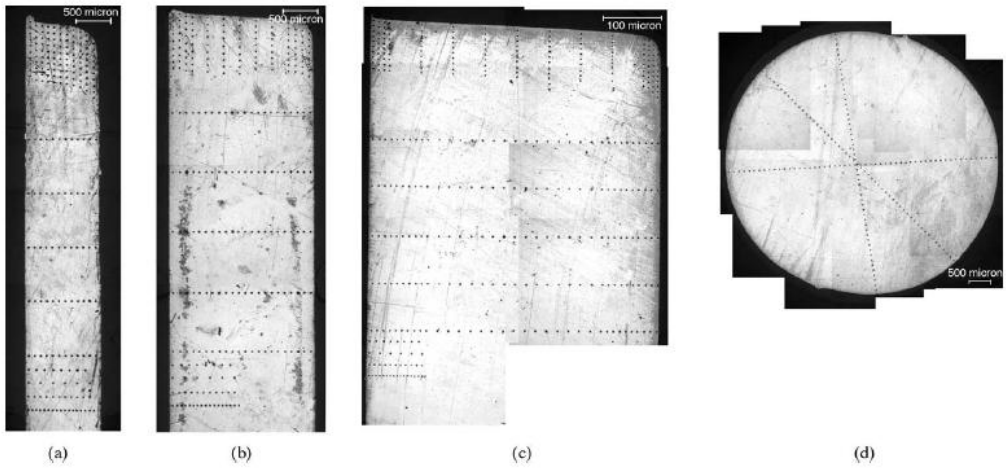

Figure 2-7: Vickers microhardness indentation patterns on the cross-sections of 1,2,5 thick rectangular (a-c) specimen, and the 6.4 mm diameter cylindrical specimen[73]

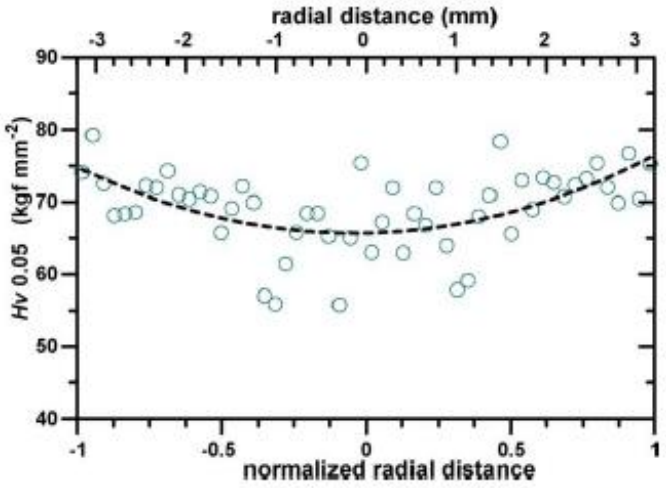

Figure 2-8: Microhardness profile for 6.4 mm cylindrical specimen. The symbols represent the diametric microhardness profile (mean values for three sets of measurements). The dashed line is a polynomial best fit [73]

Caceras et al. [27, 73] performed microhardness mapping across a sample of high pressure die cast magnesium AZ91D alloy. Figure 2-7 and Figure 2-8 show some of their results. It can be seen from Figure 2-8 that though they put a best fit curve, there is large

fluctuation of microhardness all along the sample. Weiler et al. [74] carried out microhardness mapping for high pressure die cast AM60B alloy. Through measuring microhardness across the sample, their target was to differentiate between the skin and core of HPDC sample and also to find the porous region. From their research, it became evident that the microhardness is comparatively higher near the mold wall but there is not that much fluctuation inside the sample.

In all these experiments, it is noticeable that microhardness did not vary linearly with the change of cooling rate. Though the common tradition is to somehow show that it has a trend, what should also be noticed that very high and low reading for microhardness appears almost in the same region. The possible explanation is, the microstructure can be roughly divided into matrix and secondary phase particles. These secondary phase particles are harder than the matrix. Wang et al. [75] reported that, for die cast AM50 alloy, microhardness of brittle eutectic phase β-$Mg_{17}Al_{12}$ is about 88.34Hv and the microhardness of α-Mg phase is about 66.86Hv. That means the secondary phase particles of β-$Mg_{17}Al_{12}$ are 1.3 times harder than the matrix. Any microhardness reading would be within this range and the variation would depend on the distance of indentation from the secondary phase particles. Hence, the difference in microhardness values between the skin and core is due to relatively shorter distance between secondary phases particles in the skin region. Closer to skin, the number of secondary particle is more. Thus the probability of getting a higher value is more in comparison to the core, where the particles are much more dispersed and much less in number.

Chapter 3 **Methodology**

3.1 Casting procedure

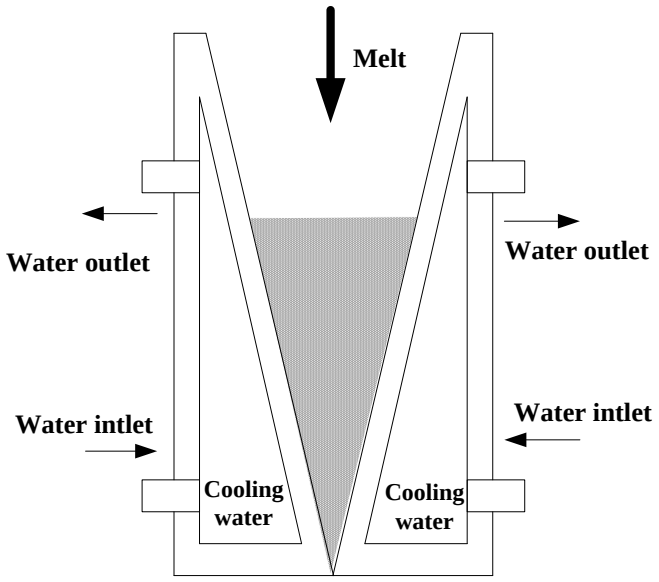

Figure 3-1: Schematic drawing of the casting method

Figure 3-1, schematically illustrates the casting procedure of wedge shaped sample in a symmetrical water cooled copper mold. Wedge casting ensures wide range of cooling rates from a single casting. As the thickness of the sample gradually changes the cooling rate also changes. The thinnest part facing the fastest cooling rate and while the thickest part faces much lower cooling rate. The microstructures at different thicknesses represent corresponding solidification conditions. The effect of cooling rate on microsegregation pattern and microstructural features of these alloys could be analyzed using this procedure. Directional solidification is the widely used technique for microsegregation

studies as growth rate and velocity could be precisely controlled. However, if industrial casting condition is taken into consideration, this setup is much closer to reality.

Bulk composition of the investigated alloys is presented in Table 3.1. In AE44 alloy, rare earth elements were added as mischmetal. Percentage of rare earth elements in mischmetal is as follows: %Ce=55.90, %La=30.50%, %Pd=6.80, %Nd=5.20, % others=1.60.

Table 3.1: Bulk composition of the investigated alloys

Alloy	%Al	%Zn	%Mn	%Si	%Cu	%Fe	%Ce (%RE*)
AE44	3.95	0.19	0.3	0.007	<0.005	<0.005	2.20 (3.94*)
AM60B	5.7	0.023	0.31	0.013	<0.005	<0.005	
AZ91D	8.8	0.75	0.34	0.015	<0.005	<0.005	

In Figure 3-2, placement of six thermocouples at different locations of the wedge is shown schematically. Time-temperature curves were obtained at those locations using the thermocouple reading. The thickness increases gradually from 6mm at location 1 to 34mm at location 6 as shown in Figure 3-2. And the distance of each location from the bottom of the wedge is also indicated. It is evident that location 1 faces the fastest cooling rate while location 6 faces the slowest cooling among the six locations.

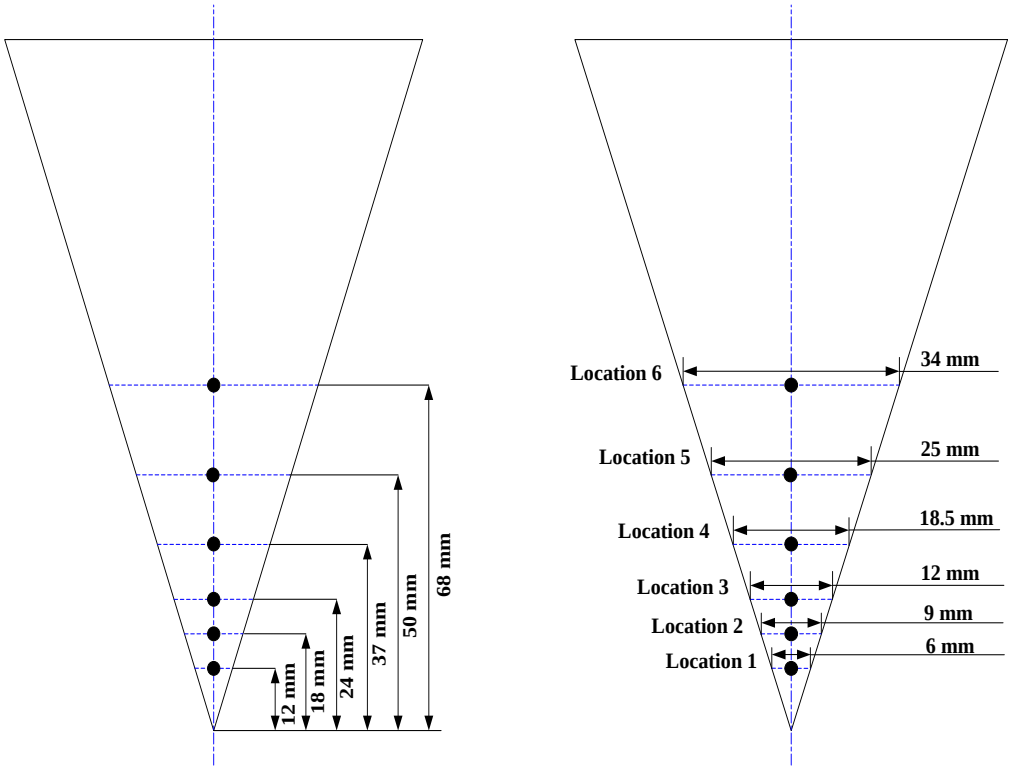

Figure 3-2: Schematic of thermocouple positions in the wedge cast sample

3.2 Sample preparation

To prepare the samples for microanalysis, solidified samples were sectioned longitudinally at the position of the thermocouple inserted and etched with nitric acid reagent (20 ml acetic acid, 1ml HNO_3 (concentrated), 60 ml ethylene glycol, 20 ml water) after being manually ground and polished. It is preferable to avoid using water from the very beginning of sample preparation for these three alloys. Grinding was done using 120, 240, 320, 400, 600, 800 and 1200 grit SiC emery paper while ethanol was used as lubricant and the samples were ultrasonically cleaned in ethanol between steps to remove any residue.

As magnesium alloys are very delicate to polish, one has to be very careful while polishing. Moments of carelessness might result in hours of re-polishing. The rotation

speed of the grinding wheel should not be too high; it should be around 100-150 rpm. For these three alloys, polishing clothes and diamond paste did not give satisfactory results. Active oxide polishing suspensions (OP-S) and polishing pads made of neoprene foam (MD/OP-Chem) from Struers were used. While doing the final polishing, the polishing pad should be cleaned every 1 minute; otherwise the brittle particles may accumulate on the polishing pad and damage the surface of the sample. The solidification microstructures were analyzed by optical microscopy (OM) and secondary electron microscopy (SEM). For the SEM use, the samples were not etched.

3.3 Microscopy and Energy Dispersive Spectrometric (EDS) Examination

The microstructure and the phase analysis of these three alloys at different locations were investigated using scanning electron microscope (SEM) (Model, Hitachi S-3400N SEM) equipped with WDS (wavelength dispersive spectrometry) and EDS (energy dispersive spectrometry) systems for elemental analysis.

The SEM was used mainly in the backscatter electron (BSE) mode at 15 keV. While using the samples for elemental analysis or microscopic examination using SEM, the samples were not etched. Except this, the grinding and polishing procedure was similar as optical microscopy. For image analysis, there should be high contrast in colors among the phases to be measured. Due to the supersaturated solution of aluminum rich α-Mg around the secondary phase particles (β-$Mg_{17}Al_{12}$ in case of AZ91D and AM60B), it is very difficult to measure the area fraction of this phase using optical micrographs. For AM60B, it is almost impossible to measure the amount of β-$Mg_{17}Al_{12}$ using optical micrograph. From optical micrograph of AM60B, it is seen that, seemingly the phases are

not at the same level from the surface. There seems to be a network like structure which is engraved upon the background and the presence of β-$Mg_{17}Al_{12}$ is difficult to detect. For AE44, optical micrographs provide enough color contrast among phases to analyze.

The composition measurements for elemental analysis were carried out using EDS. Though WDS method is more accurate than EDS for elemental analysis, it has its drawbacks also. For three magnesium alloys, cast into wedge shape, there were six sample locations for each alloy to be investigated. That means, in total 18 sample locations were investigated for the elemental analysis. At each sample location a minimum of 150 readings were taken using EDS. For EDS analysis of all these points, considering one minute per reading, plus the setup time for the machine means almost 60 hours of operational time is needed. The required time would be four times more for WDS analysis. To compare between WDS and EDS, for three sample locations of AZ91D both EDS and WDS analysis were carried out. While doing the WDS, pure Mg, Al, Mn and Zn were used as standards. In order to clarify the area scan method used in this study for EDS measurements, a schematic diagram is provided. In Figure 3-3, the dots at the intersection denote the investigated points for EDS analysis.

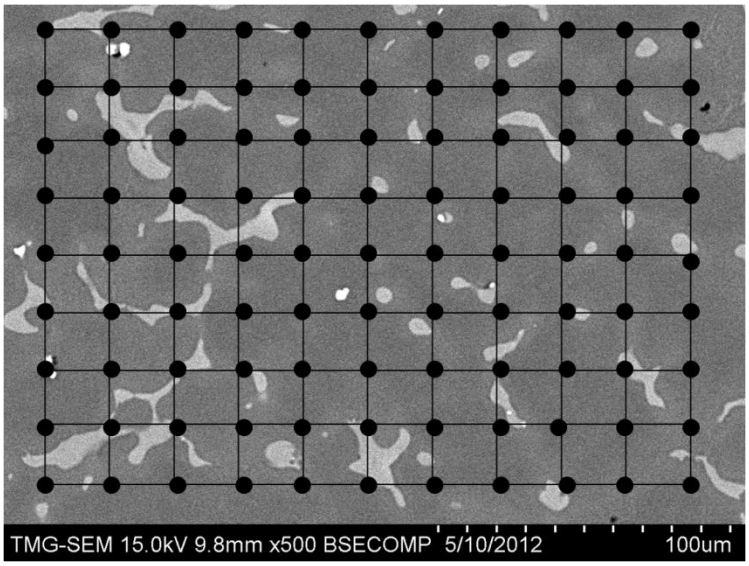

Figure 3-3: Schematic of area scan method using EDS. Each black dot corresponds to a composition measurement.

3.4 X-ray diffraction (XRD)

To detect the phases present in these alloys and to measure the volume fraction of the dominant secondary phases, X-Ray Diffraction (XRD) was performed. For AZ91D the secondary phases are β-$Mg_{17}Al_{12}$ and Al_8Mn_5. The amount of Al_8Mn_5 is so little that it is very difficult to measure the volume fraction using XRD. The volume fraction of β-$Mg_{17}Al_{12}$ was measured at different sample locations. For AM60B, the story is the same; only the volume fraction of β-$Mg_{17}Al_{12}$ was measured as the amount of Al_8Mn_5 is negligible. For AE44, volume fraction of $Al_{11}RE_3$ was measured and Al_2RE was present in trace amount.

An X-ray diffractometer, (X'Pert PRO, manufactured by PANalytical Inc.), was used to record the XRD pattern, with a Cu-Kα1 (λ=1.5418 Å) radiation produced at an applied

voltage and a beam current of 45 kV and 40 mA, respectively. The XRD spectrum was acquired from 20 to 120º 2θ at a 0.02º step size.

To prepare the samples, powders were ground in a mortar to a uniform particle size distribution and the diffraction patterns were obtained at room temperature. Silicon powder (-325 mesh) was added to all powder samples as an internal standard to correct for any systematic error. To use the peak intensities for comparison between different samples, identical sample preparation technique, amount of the sample, and data collection conditions were used. X-ray diffraction analysis of the samples was carried out using X'Pert HighScore Plus Rietveld analysis software in combination with Pearson's crystal database [76].

3.5 Dendrite arm spacing measurement

Secondary dendrite arm spacing was measured using linear intercept method. As shown in Figure 3-4, from optical micrographs, suitable locations were selected where secondary dendrite arms are clearly distinguishable.

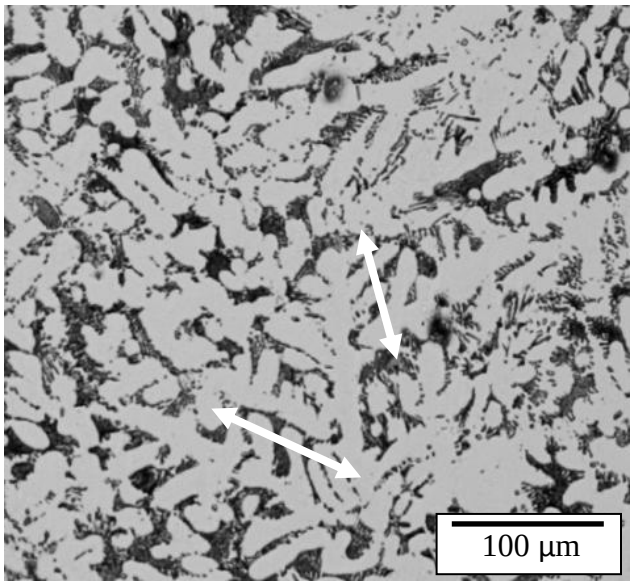

Figure 3-4: SDAS measurement technique

Then the average secondary dendrite arm spacing was measured by counting the number of arms intercepted by straight lines drawn. Readings were taken at 10 different locations close to the thermocouple position in the wedge and then averaged.

Chapter 4 **Results and discussions**

This chapter describes the solidification analysis, microstructure and morphology of the three investigated magnesium alloys (AZ91D, AM60B, and AE44). The chapter is divided into following main sections: thermal analysis, microstructural and morphological analysis, and segregation analysis.

4.1 Thermal Analysis

The cooling curves obtained at different locations of the wedge cast samples were analyzed to obtain important thermal parameters. A cooling curve contains information regarding the release of heat during solidification. This release of heat eventually changes the slope of the cooling curve which indicates the characteristics of transformation and phase reactions during solidification. However, the amount of heat evolved during some phase transformations is so small that it is difficult to detect these changes from the cooling curve alone. Hence the first and second derivative of the cooling curve was employed to determine these thermal parameters accurately. This procedure is presented in Figure 4-1for location 1 of AZ91D alloy. The block arrows denote the approximate start and end of solidification as determined from temperatures at deviations from linearity in the first and second derivative curves. The results are summarized in Table 4.1. The liquidus and solidus temperatures recorded at different wedge locations did not follow any increasing or decreasing trend with the change of cooling rate. From Table

4.1, it can be seen that the rare earth containing alloys have the smallest solidification range.

Table 4.1: Liquidus, solidus and freezing range calculation of the three alloys

Alloy	Liquidus (°C)	Solidus (°C)	Freezing range (°C)
AZ91D	600	410	190
AM60B	620	415	205
AE44	630	575	55

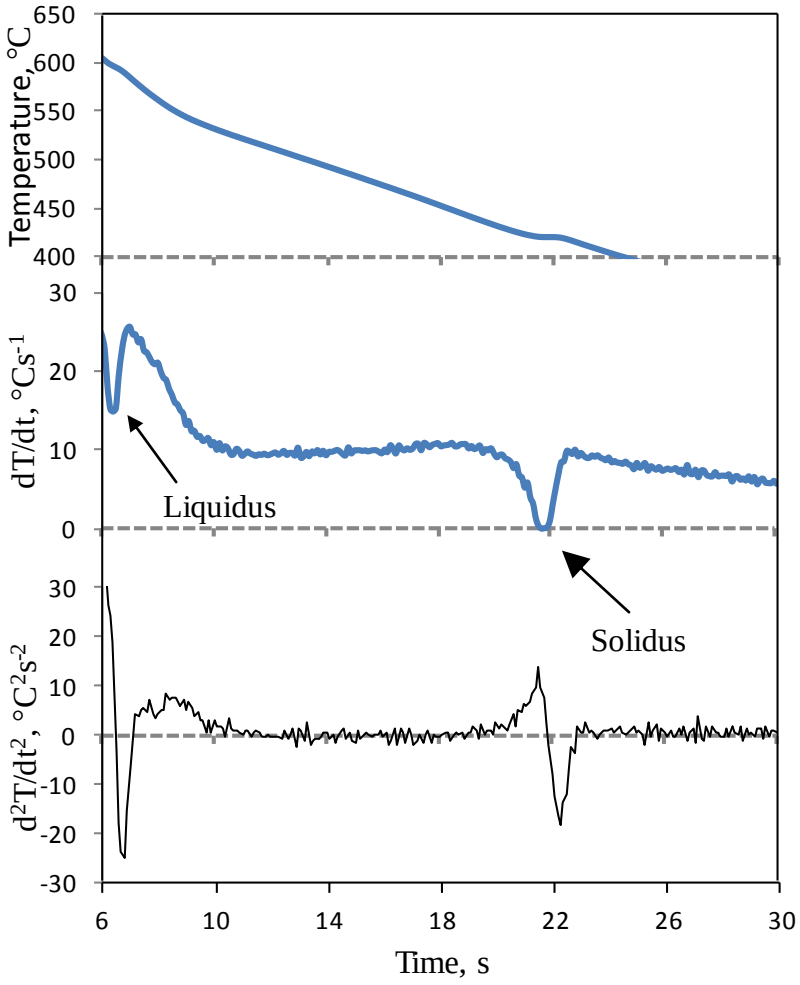

Figure 4-1: The cooling, first and second derivative curves of the AZ91D alloy showing the solidus and liquidus

Table 4.2: Cooling rate of investigated alloys within the solidification range

Cooling rate °C/s			
Location	AZ91D (600°C-410°C)	AM60B (620°C-415°C)	AE44 (630°C-575°C)
1	10.11	16.13	6.05
2	11.32	16.55	7.79
3	11.41	16	7.26
4	10.15	11.87	5.84
5	8.08	8.17	3.01
6	5.18	5.02	1.49

Cooling rates of the three investigated alloys at different thermocouple locations are presented in Table 4.2. For ease of calculation and representation, cooling rates were considered to be changing linearly within the approximate solidification range of the alloys. From the table, it can be seen that for all three alloys, within their respective solidification range, there is little difference in cooling rates among first three locations. Although it is considered that cooling rate decreases gradually from location 1 to 6, it is evident from the table that for all three alloys, cooling rate at location 2 is slightly higher than location 1. The deviation observed at these thermocouple locations can possibly be explained by some phenomenological factors. Firstly, this could be due to the delay in thermocouple response to correctly record the temperature change in rapid cooled locations. Secondly, the pattern of mold filling might also be responsible. The wedge cast sample is very narrow at the bottom hence this narrow end could solidify much earlier before rest of the locations. But the molten metal on top of this solidified location will affect its cooling rate. Thirdly, this thin end at the bottom of wedge might not be cooled properly by the circulating cooling water due to stagnation. However, samples with the same cooling rate might have different amount of microsegregation based on cooling and

solidification conditions such as thickness of sample, coarsening, and homogenization period.

4.2 Microstructural analysis

To characterize the microstructure of these three magnesium alloys, the following features of the microstructure were quantified,

- area percentage of secondary phases,
- average area of the secondary phase particles,
- maximum area of the secondary phase particles, and
- secondary dendrite arm spacing

All these microstructural features vary significantly with the change in cooling rate and subsequent microsegregation. Hence, detailed information regarding these features in respect to cooling rate would be very important for simulation and modeling of microstructure. The micrographs were taken at 500X magnification for image analysis and each micrograph covers an area of 227μm×200 μm. Measurement of average and maximum area of secondary phase particles at specific locations provides information regarding overall particle size distribution.

Microstructural mapping was done from the edge to edge for the first four thermocouple positions. For locations 5 and 6, as they are much wider, pictures were taken from the center to the edge of the wedge instead of the regular patterned edge to edge. Dimension of the wedge cast sample is provided in detail in Figure 3-2. Each picture covered a distance of 200 μm. Therefore, for location 1, there are approximately 30 pictures, for location 2, 45 pictures, for location 3, 60 pictures, for location 4, 90 pictures, for location

5, 60 pictures and for location 6, 85 pictures. These pictures were merged to produce microstructural maps and important segments are provided in the appendix (A.1-A.3) for clarity. For each location of the wedge, these merged micrographic maps are divided into three sections, edge, transition from columnar to equiaxed, and mid position of the wedge.

To measure the change in area percentage of secondary phase in each location from edge to the center of the wedge, average of five micrographs were taken. That means each bar presented in Figure 4-7, Figure 4-14, and Figure 4-21 represents approximately 1000 μm×200 μm area.

4.2.1 AZ91D microstructure

The general microstructure of the as-cast AZ91D alloy is characterized by a solid solution of aluminum in magnesium, which is known as α-Mg (hexagonal close packed structure) and eutectic β-$Mg_{17}Al_{12}$ phase. Dendrite arms of α-Mg are surrounded by a eutectic mixture of α and β-$Mg_{17}Al_{12}$. In addition to this, little amount of Al_8Mn_5 is also noticed. These phases are shown in Figure 4-2. The β-$Mg_{17}Al_{12}$ phase may be fully or partially divorced depending on the solidification rate.

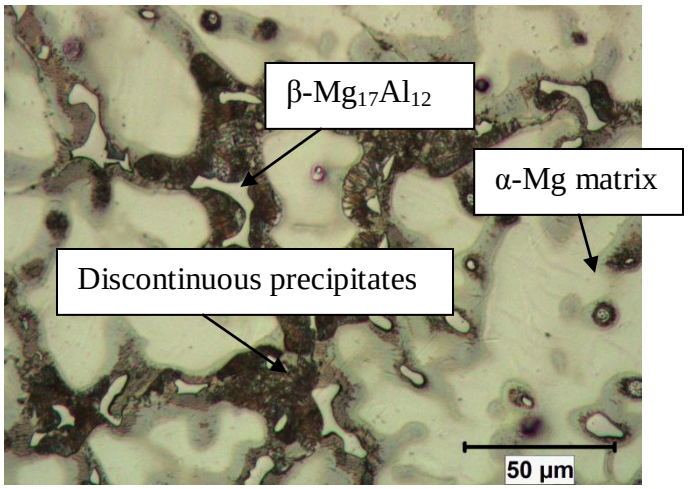

Figure 4-2: Microstructure of AZ91D alloy

In Figure 4-4, microstructures obtained from middle of wedge (close to thermocouples) at different locations of AZ91D alloy are shown. Up to location 4, morphology of β-$Mg_{17}Al_{12}$ phase was partially divorced, at location 6, fully divorced morphology was observed. Magnified pictures of these two different morphologies are provided in Figure 4-3.

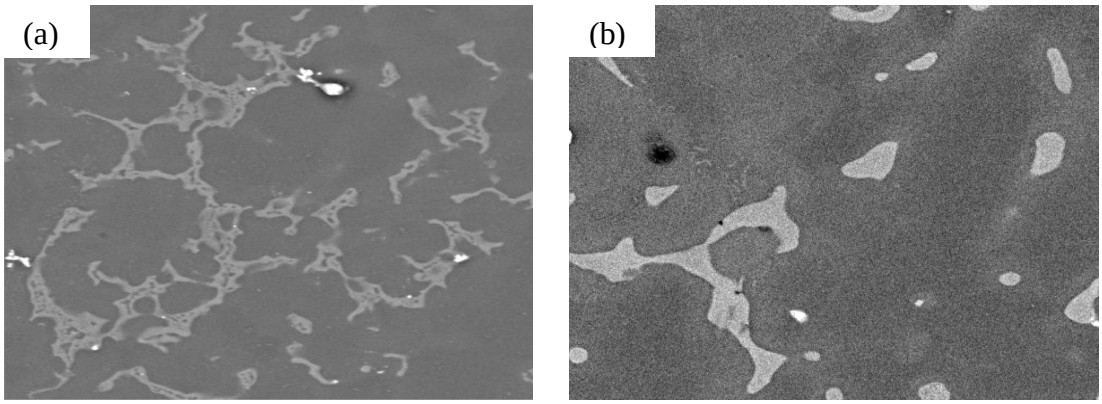

Figure 4-3 : Different morphologies observed in AZ91D alloy (a) partially divorced (b) fully divorced

As can be seen from the micrographs in Figure 4-4, secondary phase particle area increases significantly from location 1 to location 6. Though the areas of the particles are much smaller in location 1, the numbers of nucleating sites are much greater in number in comparison to location 6.

As can be seen from Figure 4-4, distance between eutectic β-$Mg_{17}Al_{12}$ phase particles also increases with the decrease of cooling rate, which indicates that secondary dendrite arm spacing is varying with cooling rate. This variation in secondary dendrite arm spacing (SDAS) was measured close to six thermocouple locations.

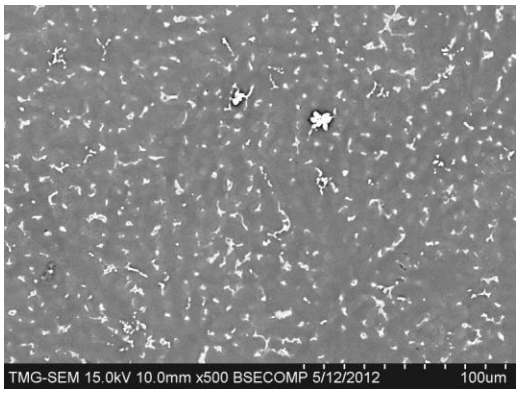

Location 1

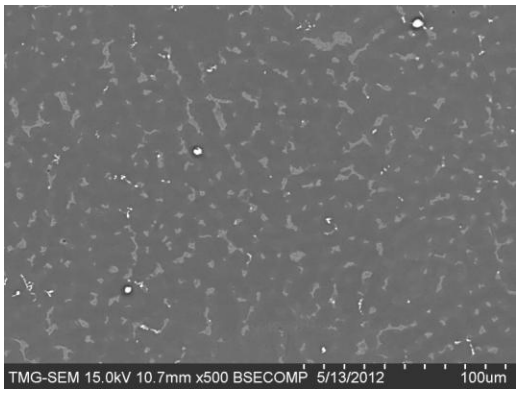

Location 2

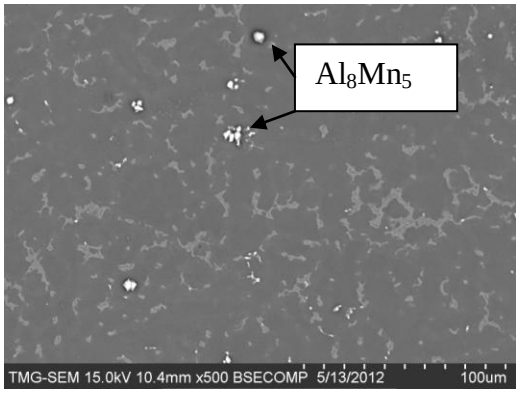

Location 3

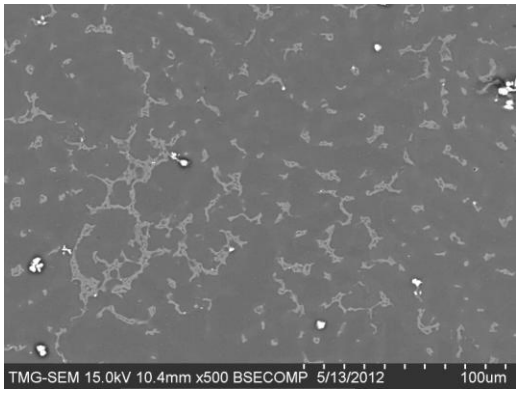

Location 4

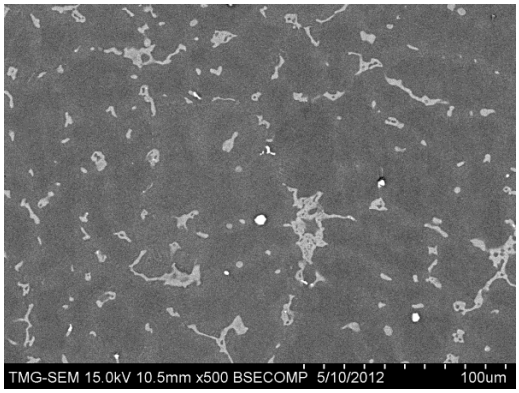

Location 5

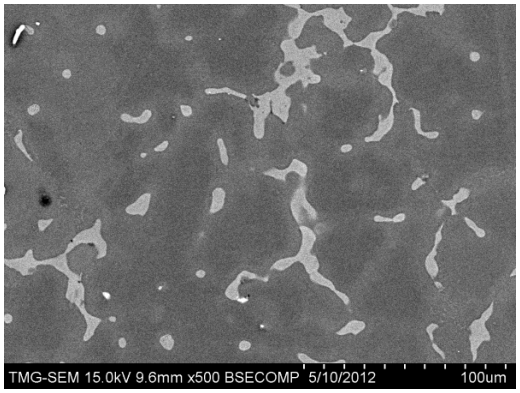

Location 6

Figure 4-4 : Microstructures at mid position of wedge at different locations for AZ91D alloy

As can be seen from Figure 4-5, secondary dendrite arm spacing increases as the cooling rate decreases. In locations 1, 2, and 3, SDAS was in the range of 9-10µm. This might be due to the fact, that cooling rates at these three locations are very close (10-11.5°C/s) as mentioned earlier in Table 4.2. Moreover, the thicknesses of these samples are also very close, that is why there is no significant change in secondary dendrite arm spacing among them. After that, in locations 4, 5, and 6 dendrite arm spacing increases gradually. SDAS is around 9µm at the bottom of the wedge and it increases up to about 26µm in location 6.

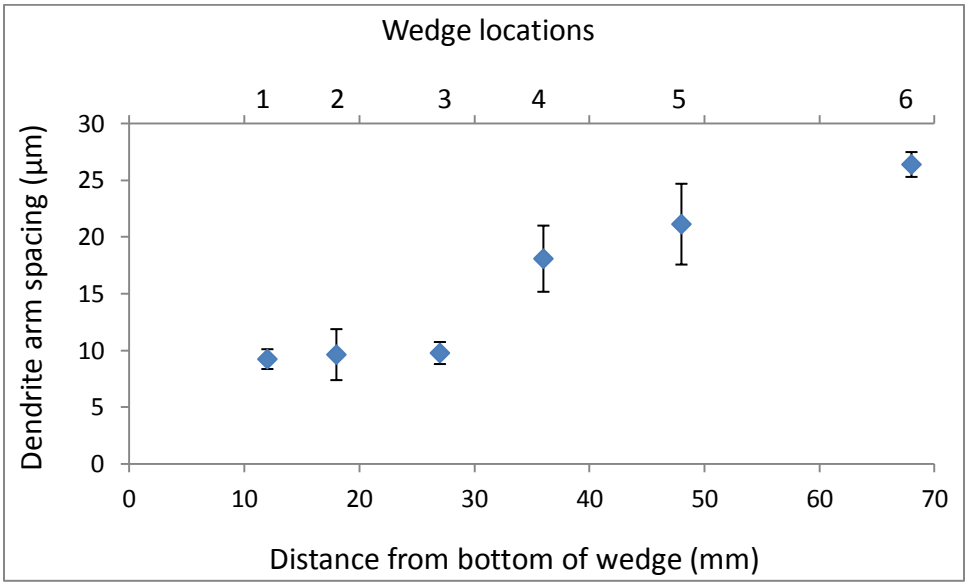

Figure 4-5: Secondary dendrite arm spacing measurement for AZ91D alloy

Area percentage measurement of β-$Mg_{17}Al_{12}$ phase is presented in Figure 4-6 and Figure 4-7. Figure 4-6 shows area percentage measurement of β-$Mg_{17}Al_{12}$ phase in the middle of the wedge close to thermocouple locations, whereas Figure 4-7 depicts the distribution of area percentage of β-$Mg_{17}Al_{12}$ phase from edge to center of wedge at different locations. As can be seen from Figure 4-6, area percentage of β-$Mg_{17}Al_{12}$ phase increases with the

decrease in cooling rate up to location 4. At location 1, the area percentage is 5.5%, whereas in location 4 it is 7.0%. Substantial reduction in area percentage was observed in locations 5 and 6.

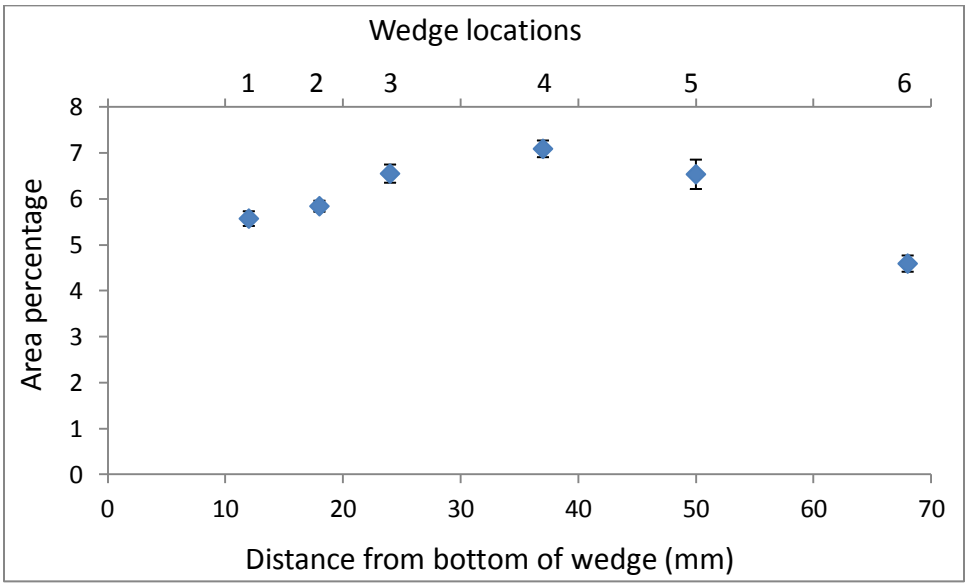

Figure 4-6: Area percentage of eutectic β-$Mg_{17}Al_{12}$ at the center of the wedge at different locations for AZ91D alloy

This reduction could be due to discontinuous precipitation which takes place at slow cooling rates. If the cooling rate is slow, continuous β-$Mg_{17}Al_{12}$ phase decomposes to fine discontinuous precipitates. These precipitates could not be measured using scanning electron microscopy as they do not have distinguishable color difference from the α-Mg matrix.

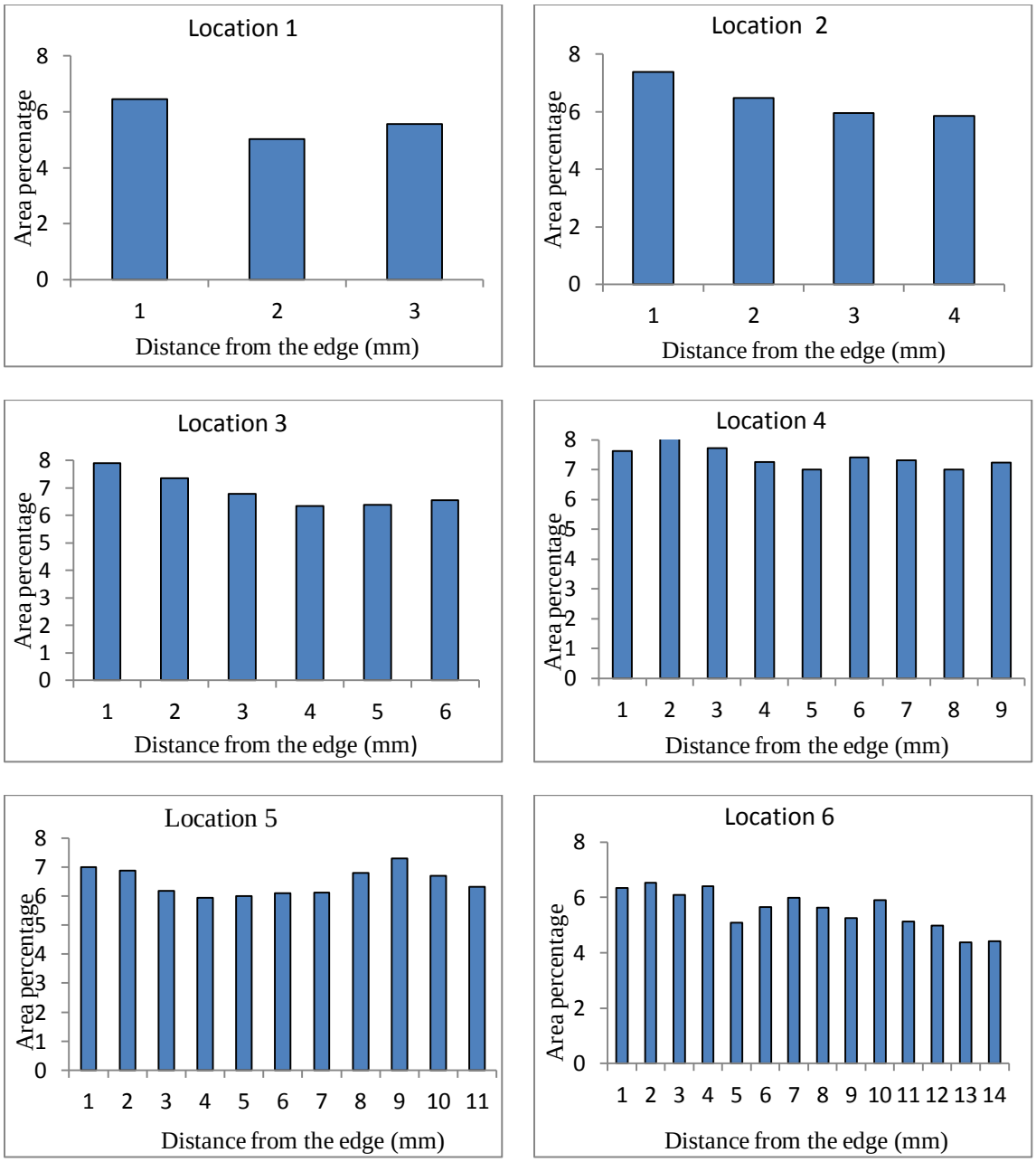

Figure 4-7 : Area percentage of β-$Mg_{17}Al_{12}$ phase at different sample locations from the edge to center

Figure 4-7 demonstrates the area percentage distribution of β-$Mg_{17}Al_{12}$ phase in different locations of wedge from edge to center. As can be seen from this figure, in all locations,

closer to the mold wall amount of β-$Mg_{17}Al_{12}$ phase were higher in comparison to center of the wedge. For example, in location 2, close to edge, area percentage of β-$Mg_{17}Al_{12}$ phase is 7.3, whereas at the middle of this location it is 5.8%. Significant drop in area percentage of β-$Mg_{17}Al_{12}$ phase was observed throughout the entire location 6 in comparison to locations 3 and 4. Highest area percentage measured in location 6 was 6.5%, which is much lower than around 8% observed in locations 3 and 4.

Variation of average area of β-$Mg_{17}Al_{12}$ phase particles at different wedge locations is presented in Figure 4-8. As can be seen from Figure 4-8, average particle area changes gradually with cooling rate. At locations 1, 2, and 3 the average particle area is approximately 1μm^2, whereas at location 6, the area increases up to 5 μm^2.

Furthermore, in each location the maximum area occupied by individual particles were also measured and presented in Figure 4-9. Similar to average area of particles, area occupied by large particles also increases with the decrease of cooling rate. In location 1, large particles were occupying approximately 10 μm^2, whereas in location 6 large particles were in the range of 50-60 μm^2. Detail distribution of average particle area and maximum particle area is provided in appendix A.4-A.6.

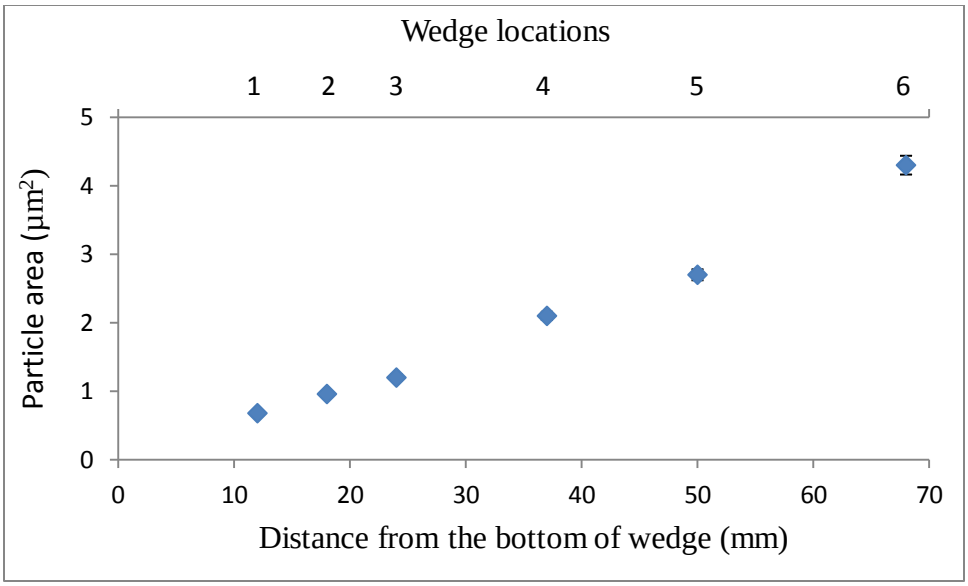

Figure 4-8: Variation of average particle area of β-$Mg_{17}Al_{12}$ at the six thermocouple locations of AZ91D alloy

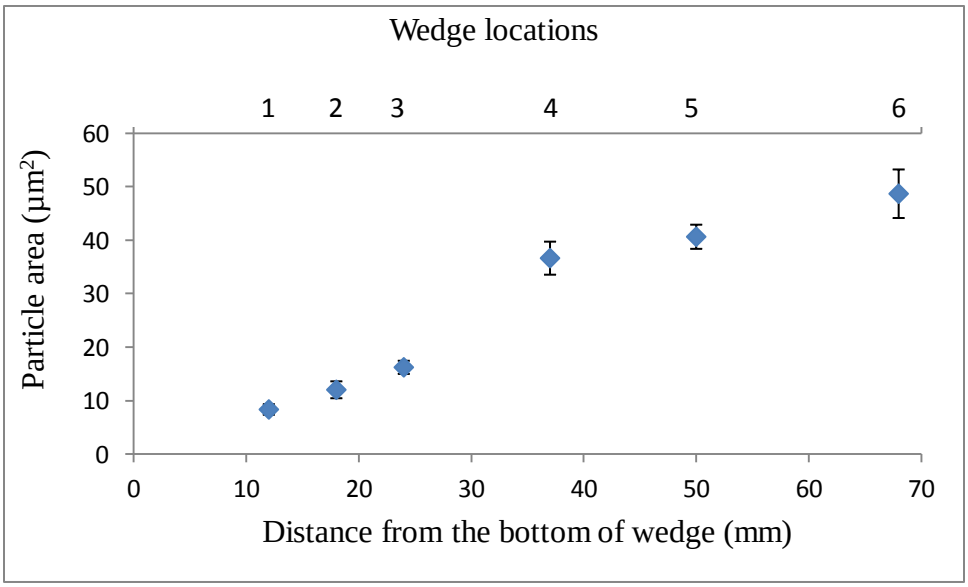

Figure 4-9: Variation of large particle area of β-$Mg_{17}Al_{12}$ at the six thermocouple locations of AZ91D alloy

4.2.2 AM60B microstructure

The typical microstructure of AM60B alloy consisting of α-Mg dendrite cells and a divorced-eutectic (α-Mg + β-$Mg_{17}Al_{12}$) is presented in Figure 4-10. A few spherical Mn-rich intermetallic particles are also generally observed in the microstructure. The primary α-Mg dendrites form the largest portion of the microstructure and are surrounded by the divorced eutectic.

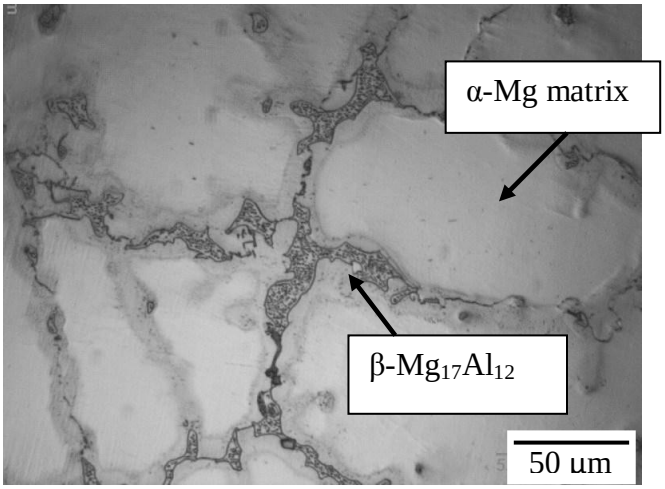

Figure 4-10: Microstructure of AM60B alloy

Microstructures obtained from the middle of the AM60B wedge casting at the six locations (close to thermocouples) are shown in Figure 4-11. Fully divorced morphology was observed for β-$Mg_{17}Al_{12}$ phase in all locations. Presence of coring was more obvious in locations 5 and 6. Secondary phase particle area increased significantly from location 1 to location 6, subsequently number of nucleating sites decreased.

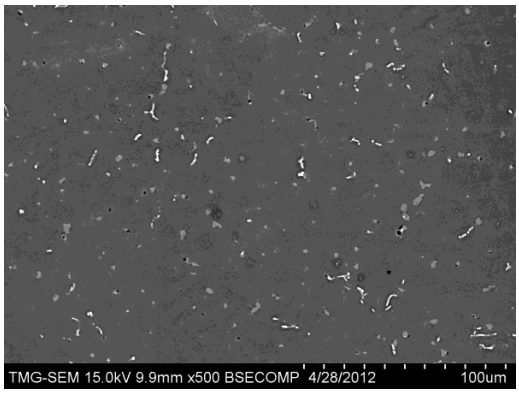

Location 1

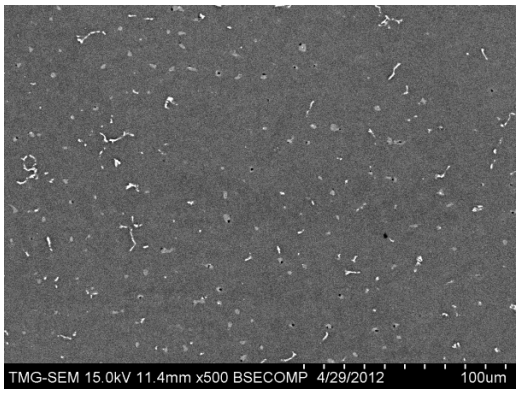

Location 2

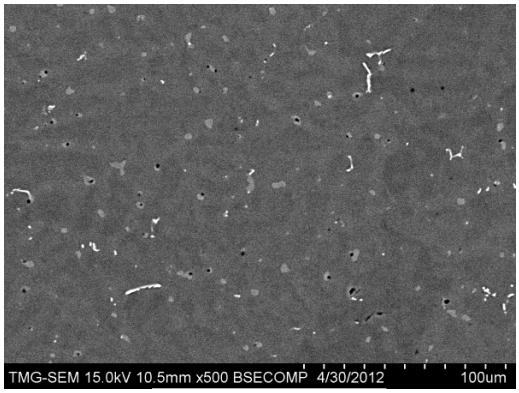

Location 3

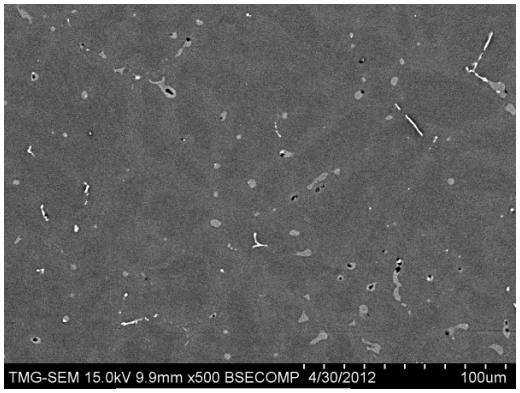

Location 4

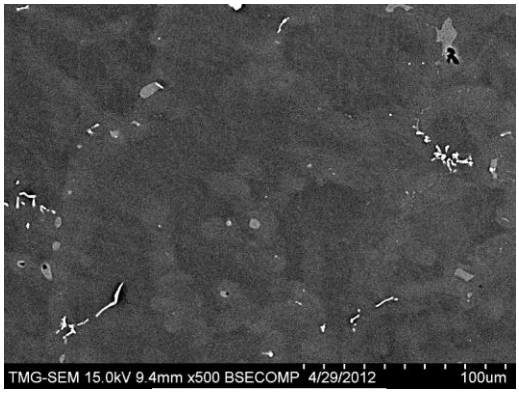

Location 5

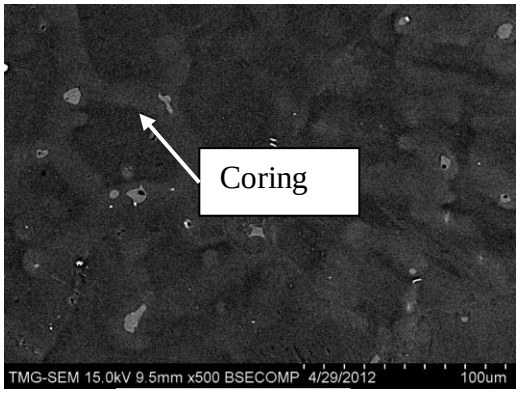

Location 6

Figure 4-11: Microstructures at mid position of the wedge casting at different locations for AM60B alloy

Secondary dendrite arm spacing (SDAS) was measured at the center of the wedge at different locations. Figure 4-12 shows the variation of SDAS with the change of cooling rate. SDAS increased gradually with the decrease of cooling rate. At location 1 the SDAS is approximately 15 μm and it gradually increases up to 30 μm at location 6.

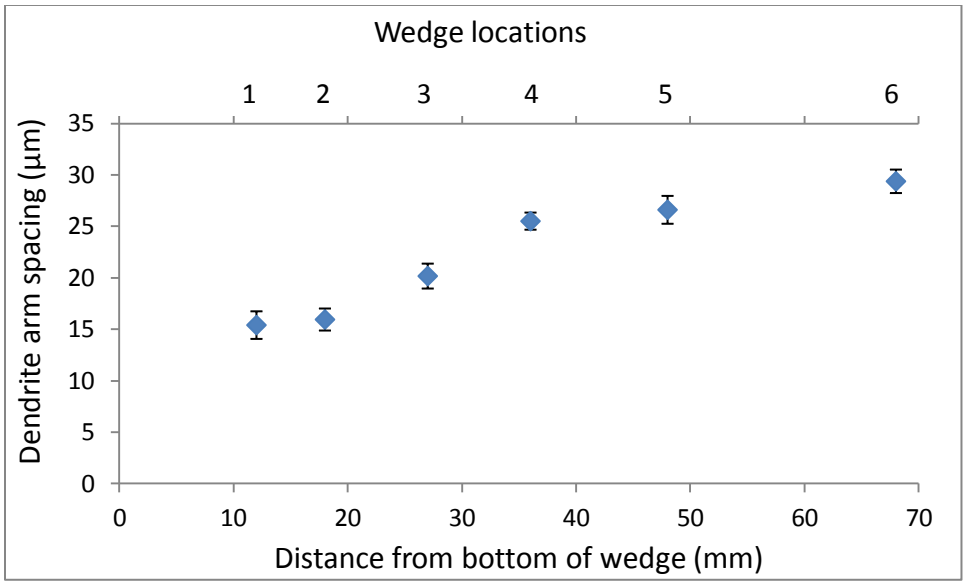

Figure 4-12: Secondary dendrite arm spacing at center of wedge at different locations for AM60B alloy

Area percentage of β-$Mg_{17}Al_{12}$ was measured at the center of the wedge for different locations and also from the edge to the center. Figure 4-13 shows the change in area percentage in the center of the wedge at different locations. The area percentage of β-$Mg_{17}Al_{12}$ was much lower in all positions in comparison to AZ91D alloy. In AZ91D, the lowest area percentage observed was approximately 4.5%, whereas the highest area percentage observed in AM60B alloy is 2.1%. There was not much change in area percentage up to location 4. In the first four locations, area percentage of β-$Mg_{17}Al_{12}$ was

~2%. Noteworthy reduction in area percentage was observed in locations 5 and 6. In these two locations, area percentage was almost half in comparison to first four locations. This decrease might be due to discontinuous precipitation which occurs due to slow cooling.

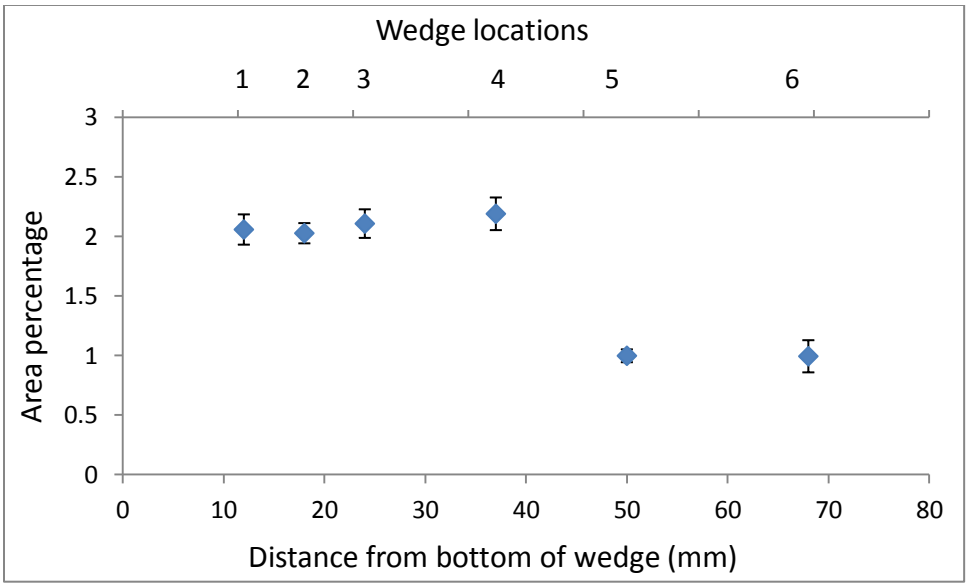

Figure 4-13: Area percentage of β-$Mg_{17}Al_{12}$ at the center of the wedge at different locations

Figure 4-14 shows the change of area percentage from edge to the center of the wedge in different locations. Generally, close to mold wall higher value of eutectic percentage is expected. However, up to location 4, eutectic percentage did not vary much between the edge and center of the wedge. This expected change in area percentage in between the center and the edge was more prominent in locations 5 and 6. These locations face comparatively lower cooling rate and they are much wider than the first three locations.

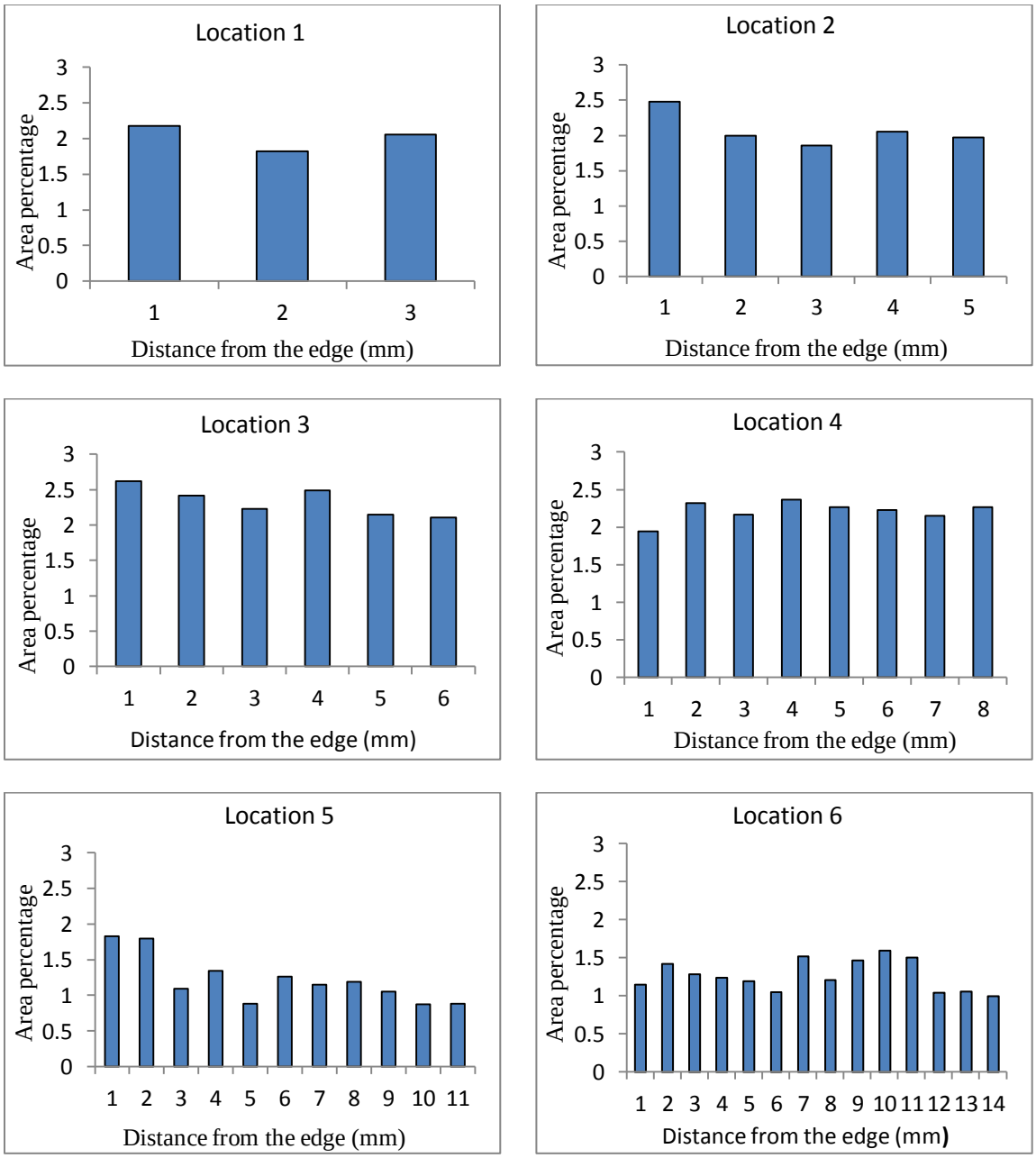

Figure 4-14: Area percentage of β-$Mg_{17}Al_{12}$ phase at different wedge locations of AM60B alloy

As can be seen from Figure 4-14, area percentage of eutectic is not the same in all locations even at the same distance from the edge of the wedge. At locations 2, 3, and 4, close to the edge, area percentage of eutectic is ~2.5%, whereas in location 6, at the same distance from the edge the area percentage is ~1.5%. Another point to be observed is that at first four locations, whatever be the distance from the edge, area percentage is always higher than 2%. But in locations 5 and 6, especially in location 6, the area percentage of eutectic is less than 1.5% at any distance from the edge.

Change of average particle area at different locations is presented in Figure 4-15. Average particle size increases gradually from location 1 to 6 with the decrease in cooling rate. As can be seen from the figure, at location 1, the average particle area is in the range of 0.4 μm^2 and the average particle area increases up to 0.8 μm^2 at location 6.

Change of particles occupying large area is shown in Figure 4-16. It also follows the general trend of increasing gradually with lowering of cooling rate. As can be seen from the figure, although average particle area at all locations is in the range of 0.1-1.8 μm^2, large particles covering more than 12 μm^2 area is also present. At locations 1 and 2, large particles are in the range of 2-4 μm^2, whereas at locations 5 and 6 it is 10-12 μm^2.

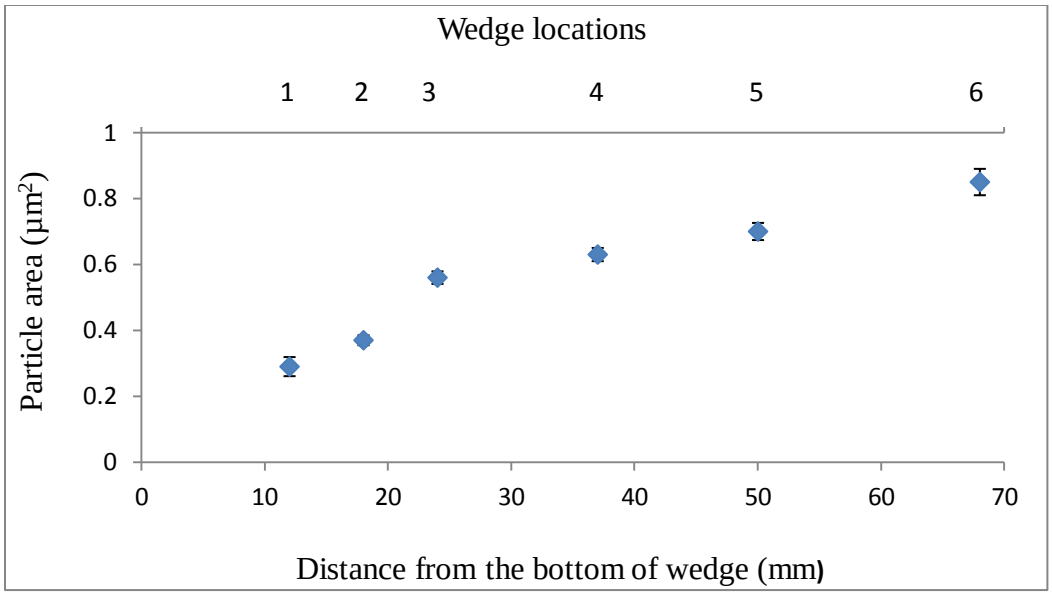

Figure 4-15: Variation of average particle area at the six thermocouple locations

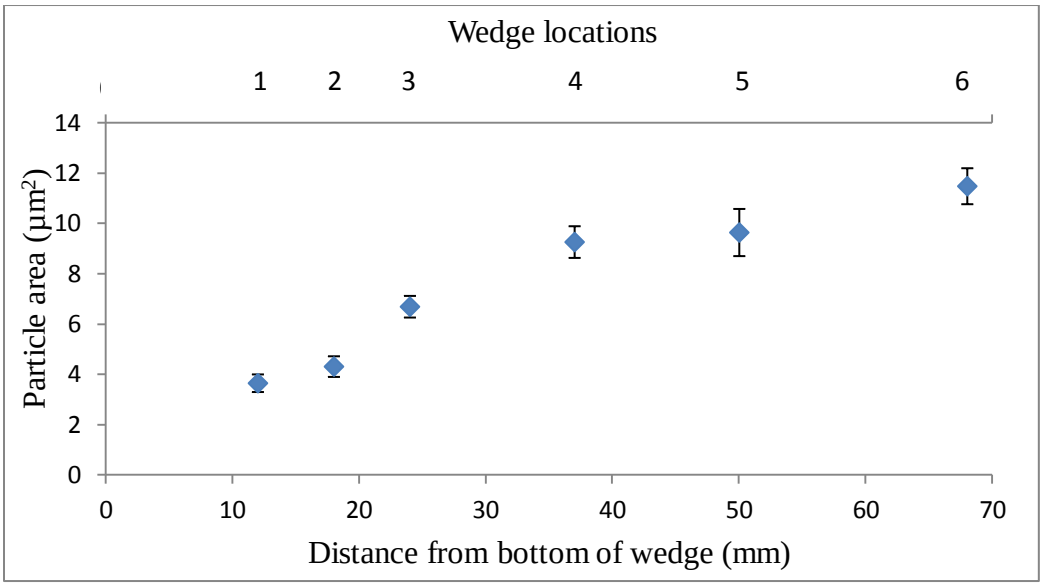

Figure 4-16: Variation of large particle area at the six thermocouple locations

4.2.3 AE44 microstructure

Many researchers [77-86] have worked with AE44 but there is significant difference in the nominal alloy composition, as rare earth addition, some have used mischmetal, some pure lanthanum or cerium. Different combination of mischmetal results in different microstructures. A typical microstructure of AE44 alloy consisting of primary α-Mg dendrites and intermetallic phases in the interdendritic regions or at grain boundaries is presented in Figure 4-17. The intermetallic phases have two distinctive morphologies; one is a lamellar or needle like acicular morphology and the other with a particulate or globular shape. The lamellar phase is identified as $Al_{11}RE_3$ and the particulate shaped is Al_3RE. $Al_{11}RE_3$ is the dominant phase in all wedge locations, the presence of Al_3RE is in very little amount.

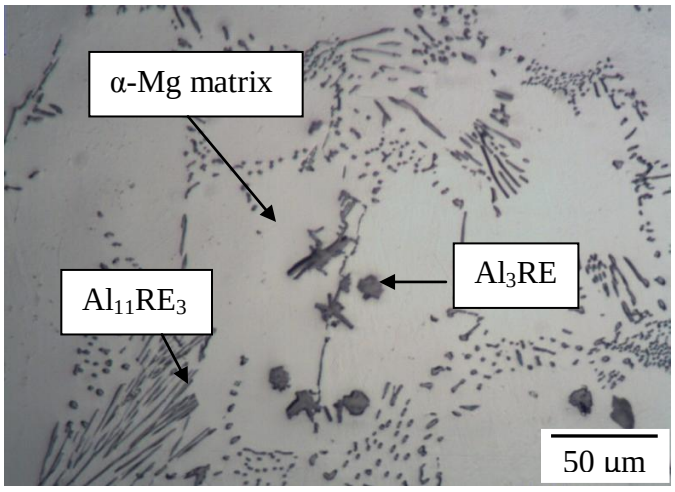

Figure 4-17: Microstructure of AE44 alloy

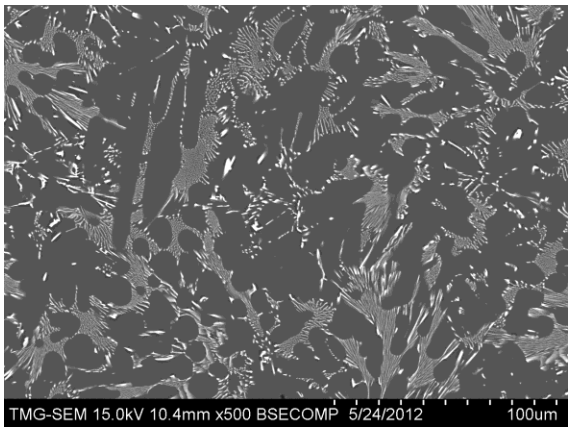

Location 1

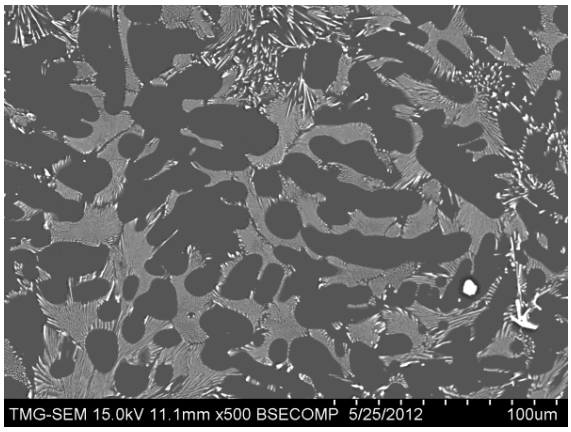

Location 2

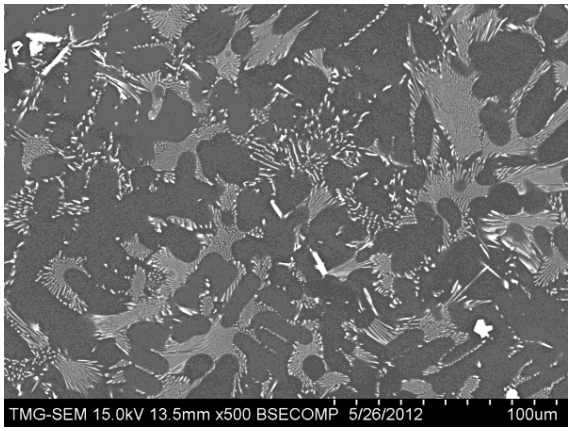

Location 3

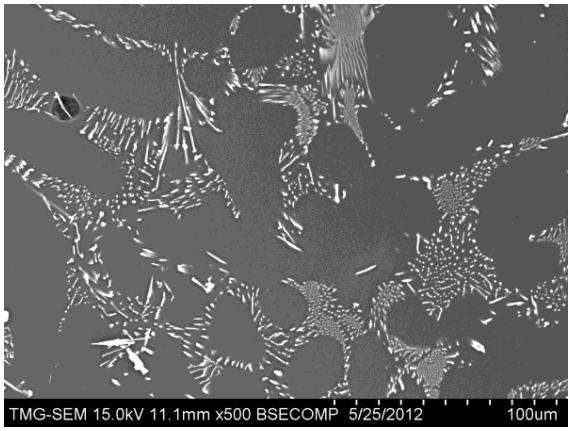

Location 4

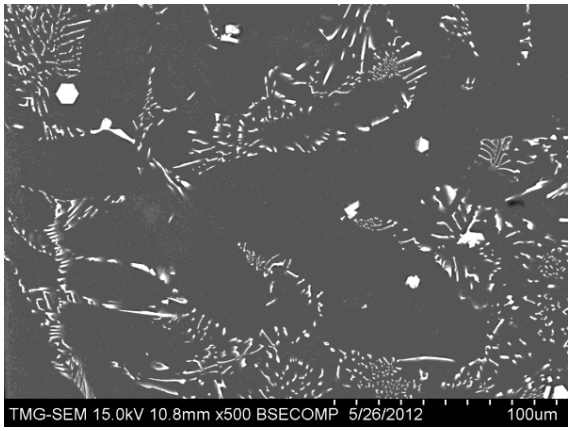

Location 5

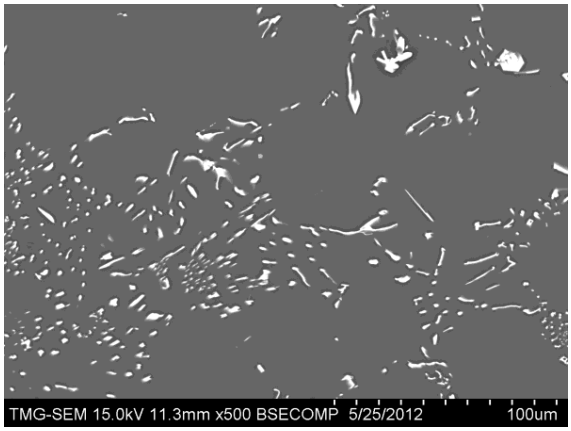

Location 6

Figure 4-18: Microstructures at the center of the wedge of AE44 alloy at the six locations

Figure 4-18, shows the variation of microstructure with cooling rate at the center of the wedge at different locations. As can be seen from the Figure 4-18, locations 1, 2 and 3 have similar cluster like morphology of $Al_{11}RE_3$. Then from location 4, the clusters start to disperse. This transition continues in location 5 and 6, where the morphology is fully dispersed.

Figure 4-19 shows the variation of secondary dendrite arm spacing (SDAS) with decreasing the cooling rate. At first three locations, the SDAS varies in the range of 10-15 μm. This could be due to the fact that these locations had almost similar cooling conditions due to proximity to the bottom of the wedge. After that, dendrite arm spacing increases up to 45 μm due to significant reduction in cooling rate at location 6.

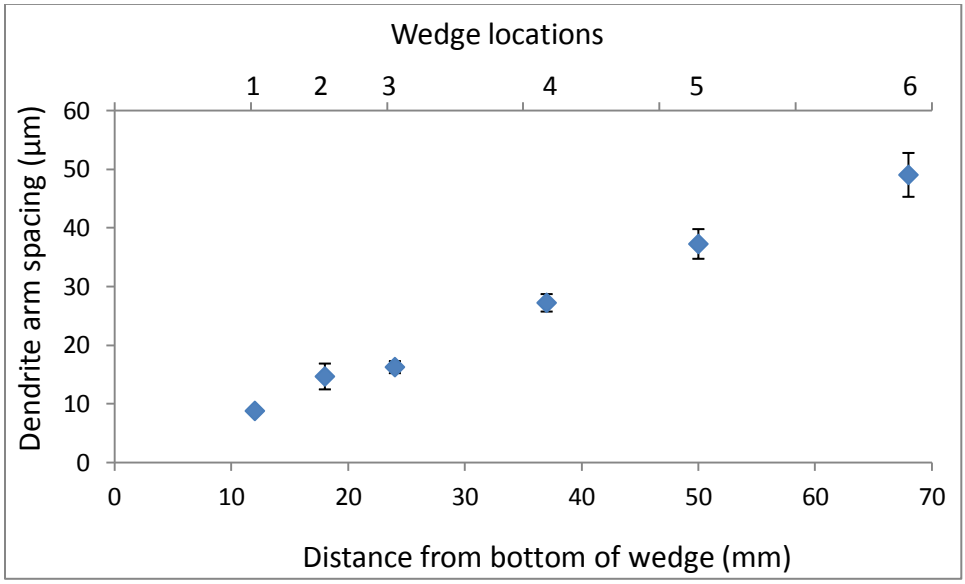

Figure 4-19: SDAS measurement at center of the wedge of AE44 at different locations

In Figure 4-20, change of area fraction of secondary phase precipitates with cooling rate is shown. From the figure it is evident that with the decrease of cooling rate, area percentage of secondary phase precipitates decreases. At location 1, the area percentage

is 20% of the total area, it gradually diminishes and at location 6, it is less than 10% of the total area.

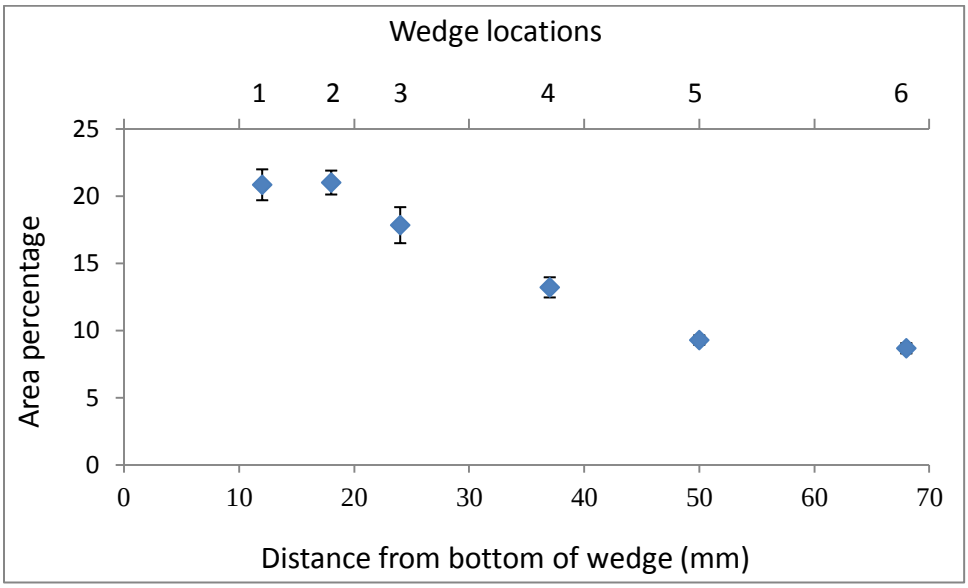

Figure 4-20: Area percentage of secondary phase precipitates in the center of the wedge at different locations

Figure 4-21, shows the variation of area percentage of secondary phase precipitates at different locations in the wedge from edge to center. Except location 1, the area percentage was higher closer to mold wall and then decreased gradually towards the center. At locations 2, 3, and 4, adjacent to mold wall area percentage of secondary phase precipitates were ~20%, whereas in location 6 area percentages of these precipitates were less than 15% in the edge of the wedge. In fast cooled locations, such as location 2, there was not much difference in area percentage between edge and center. But, as the cooling rate decreases, in locations 4, 5, and 6, 40-50% reduction in area percentage was observed between edge and center.

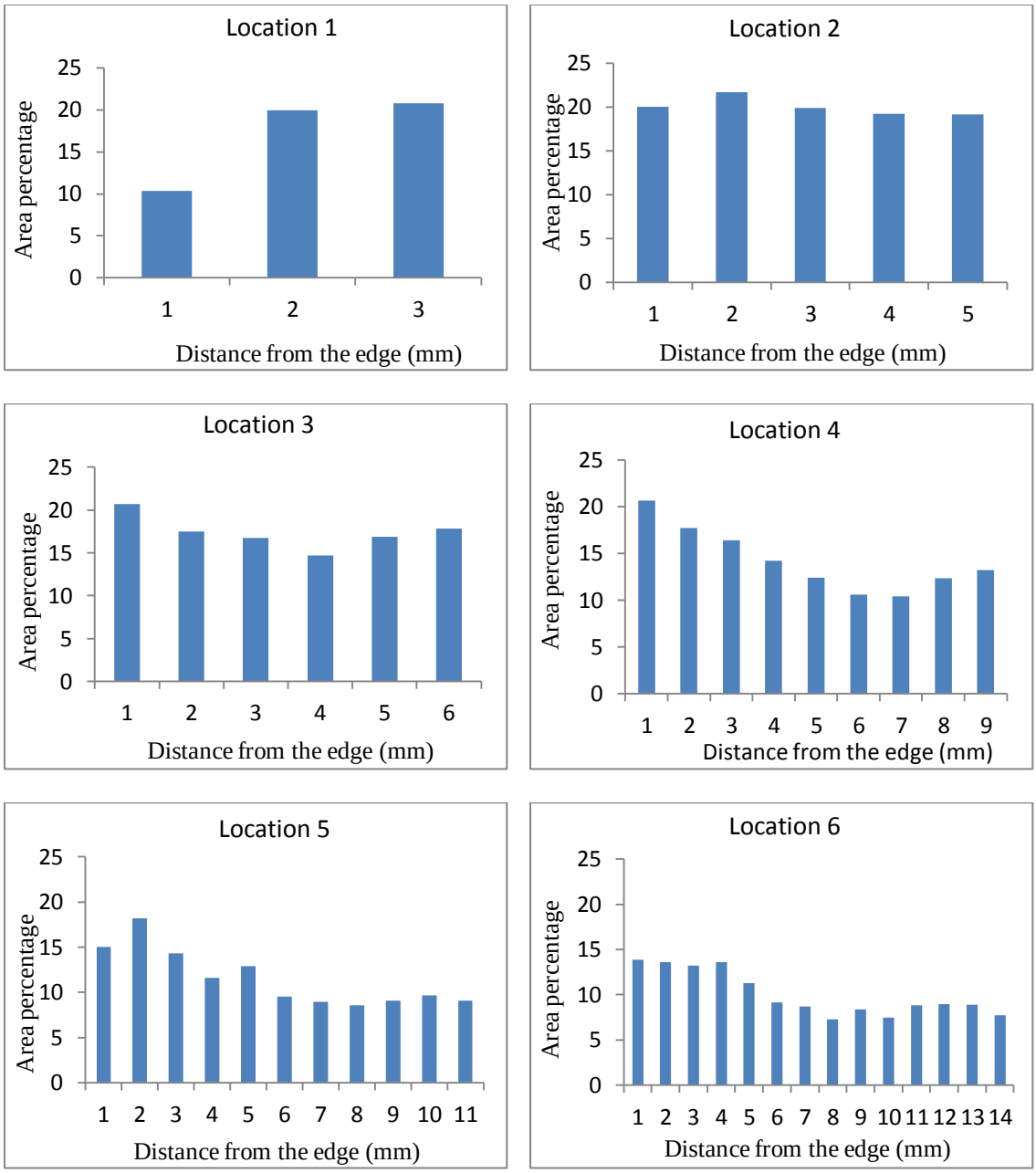

Figure 4-21: Area percentage of secondary precipitates at different locations of wedge cast sample of AE44 alloy

Change of average particle area at different thermocouple locations is shown in Figure 4-22. Due to the presence of large number of small sized lamellar particles, there is no

significant variation in the average particle area in all locations. In all locations the average particle area was in the range of 0.4-0.9 μm^2.

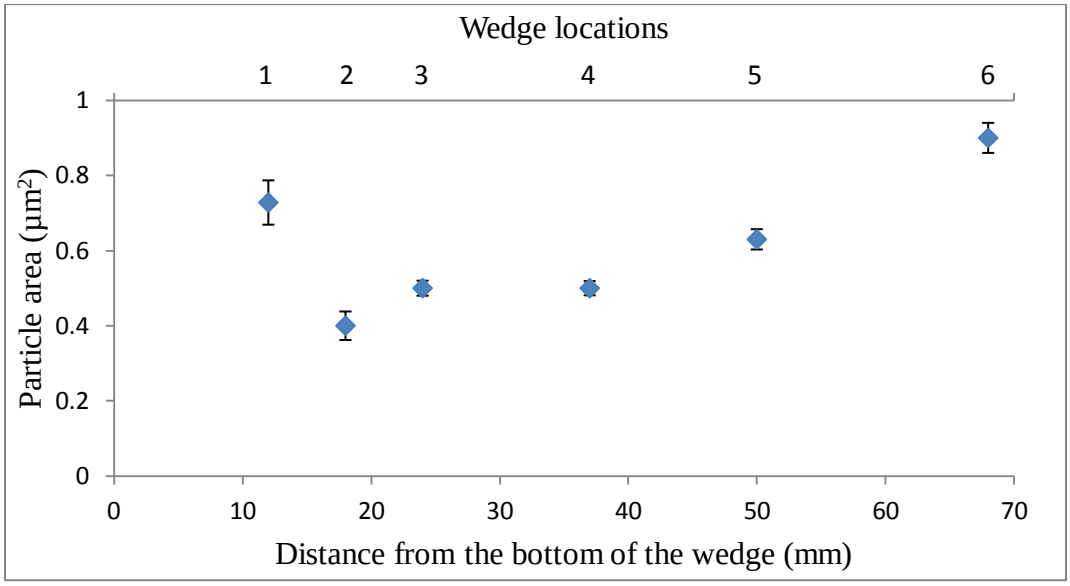

Figure 4-22: Variation of average particle area at the six thermocouple locations

Change of large particle area is shown in Figure 4-23. As can be seen from the figure, in all locations, especially in the first four locations, some large particles were observed occupying ~70-90 μm^2. Explanation regarding this issue is provided later. Apart from that, larger particles were mostly observed in slow cooled locations. Majority of the large particles in locations 5 and 6 were in the range of 30-50 μm^2.

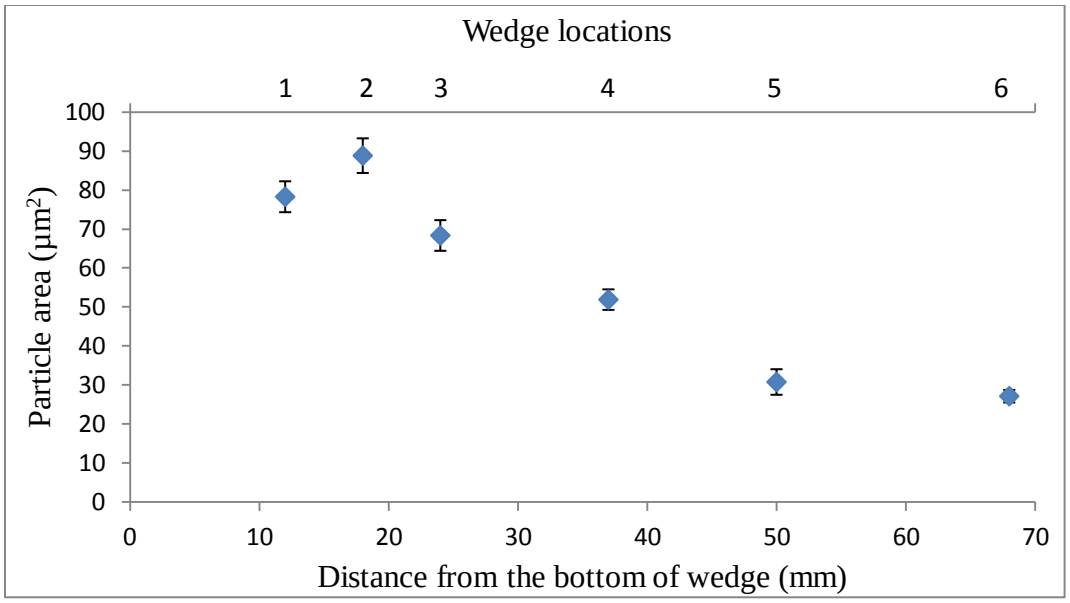

Figure 4-23: Variation of large particle area at the six thermocouple locations

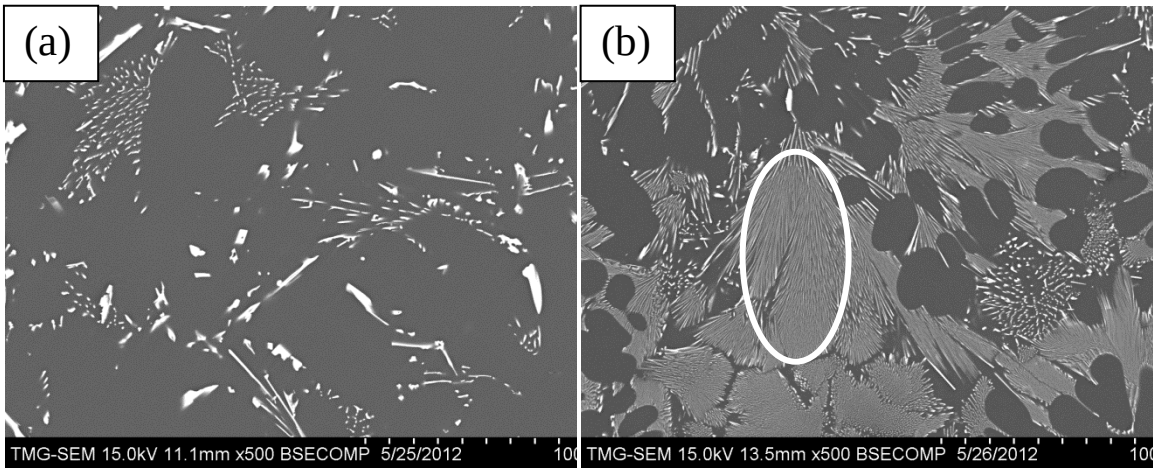

Figure 4-24: Different morphologies in AE44 alloy (a) dispersed (b) clustered

As can be seen from Figure 4-24, two distinctive morphologies could be found in AE44 alloy. The clustered morphology shown in Figure 4-24(b) was present in locations 1 to 4. As mentioned earlier, in locations 1 to 4, the morphology is cluster like and these clusters are actually dense accumulation of lamellar shaped particles. They are so densely packed

that even at 1000X magnification using scanning electron microscopy, it was not possible to measure their area as individual entity. While using the image analysis software to detect the area of the large particles, sometimes the entire cluster (indicated portion in Figure 4-24(b)) was calculated as a single particle. Hence, at locations 5 and 6, where the particles are dispersed, the maximum area of the particles represents the area occupied by a single precipitate, whereas particles occupying more than 100 μm^2 area observed in locations 1 to 4 might be representative of those clusters.

4.3 Microsegregation measurements

Quantitative microsegregation analysis was carried out close to the six thermocouple locations for the three investigated magnesium alloys. The following results were obtained from the acquired data at different locations of the wedge,

- solute redistribution profile for alloying elements (experimental & modeling)
- partition coefficient
- segregation index (ratio between minima and bulk composition) and segregation deviation
- area percentage of eutectic from the distribution profiles

Inhomogeneous distribution of solute elements during dendritic solidification of an alloy takes place due to coring. Coring or layered structure solidification is the key concept for understanding microsegregation. As can be seen from the schematic diagram of dendrite arm in Figure 4-25(a), the chemical composition at point 'C' is different from the chemical composition of point 'E'. It is assumed that, solidification starts at point 'C' and finishes at point 'E' and the change in chemical composition is gradual. In Figure 4-25

(b), optical micrograph of AZ91D alloy is presented to compare with the schematic diagram.

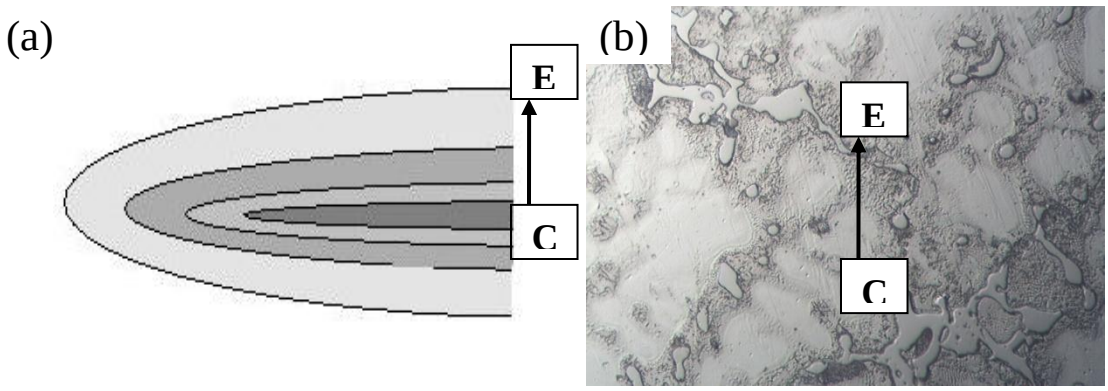

Figure 4-25: Coring in dendritic solidification; (a) schematic of dendrite arm (b) dendritic microstructure in optical micrograph of AZ91D alloy.

As mentioned in Table 3.1, bulk chemical composition of investigated AZ91D alloy is 8.8 wt.% Al, 0.75 wt.% Zn, 0.34 wt.% Mn and the rest is magnesium. When the molten alloy starts to solidify, at point 'C' the wt% of aluminum can be as low as 2 or 3wt%, depending on the cooling rate. And it gradually increases to the last point to be solidified, namely point 'E'. Some alloying elements have the tendency to accumulate in higher concentration in the edge of dendritic arm. These elements have low concentration at the center of the arm. Some alloying elements behave in opposite way; they have higher concentration at the middle of dendrite arm and then gradually decrease towards the edge. For example, Mirković et al. [42] reported for AZ31 alloy, aluminum and zinc were low in concentration in the dendrite core and they gradually increased towards the dendrite periphery, whereas manganese showed opposite trend with high concentration in the dendrite core.

4.3.1 Solute redistribution profile

Microsegregation measurements were done using SEM-EDS. At each thermocouple location more than 150 readings were taken in a 10×15 rectangular grid, with a spacing of 10μm between each point. All the data points were sorted based on the weighted interval ranking sort (WIRS) method. Details about this method could be found in Ganesan et al. [32]. This method comprises of three basic steps,

- determining the segregation trend,
- providing ranking to the data based on the segregation trend, and
- assigning fraction solid.

Determining the direction of segregation of the major alloying elements is the first step of WIRS method. The alloying elements which were present in more than 0.5wt% in the bulk composition of the alloy were considered as major alloying elements. This assumption was made because if any element has less than 0.5wt% in the bulk composition, it is difficult to detect its presence by EDS analysis and error involved in detection is much higher. In this regard, microsegregation analysis was carried out for aluminum and zinc in AZ91D, aluminum and manganese in AM60B, and aluminum, cerium, and lanthanum in AE44. The bulk composition of the investigated alloys is given in Table 3.1. Although, weight percentage of manganese is 0.31% in AM60B alloy, still an attempt was made to investigate its distribution profile.

Magnesium is the element present in highest concentration in all three alloys. Hence, segregation trends of other elements were determined based on decreasing trend of magnesium. Segregation trend of these alloys are presented in Figure 4-26.

According to the binary Mg-Al phase diagram, the first region to solidify would have the highest Mg concentration and the last region to solidify would have the lowest. Based on this assumption, the raw data generated by the SEM-EDS analysis was sorted in decreasing order of Mg concentration. Hence, the alloying elements which have increasing concentration with the decrease in Mg concentration will have low concentration at dendrite core and high concentration at dendrite periphery.

For AZ91D and AM60B, with the increase of magnesium concentration, concentration of Al and Zn decreases while Mn shows the opposite trend. That means, Al and Zn would be low in the dendrite core and gradually increase towards the dendrite periphery. For AE44 alloy, with the increase of Mg concentration, all other elements Al, La, Ce, and Nd decrease in concentration. Thus, the concentration of these elements will be low in the dendrite core.

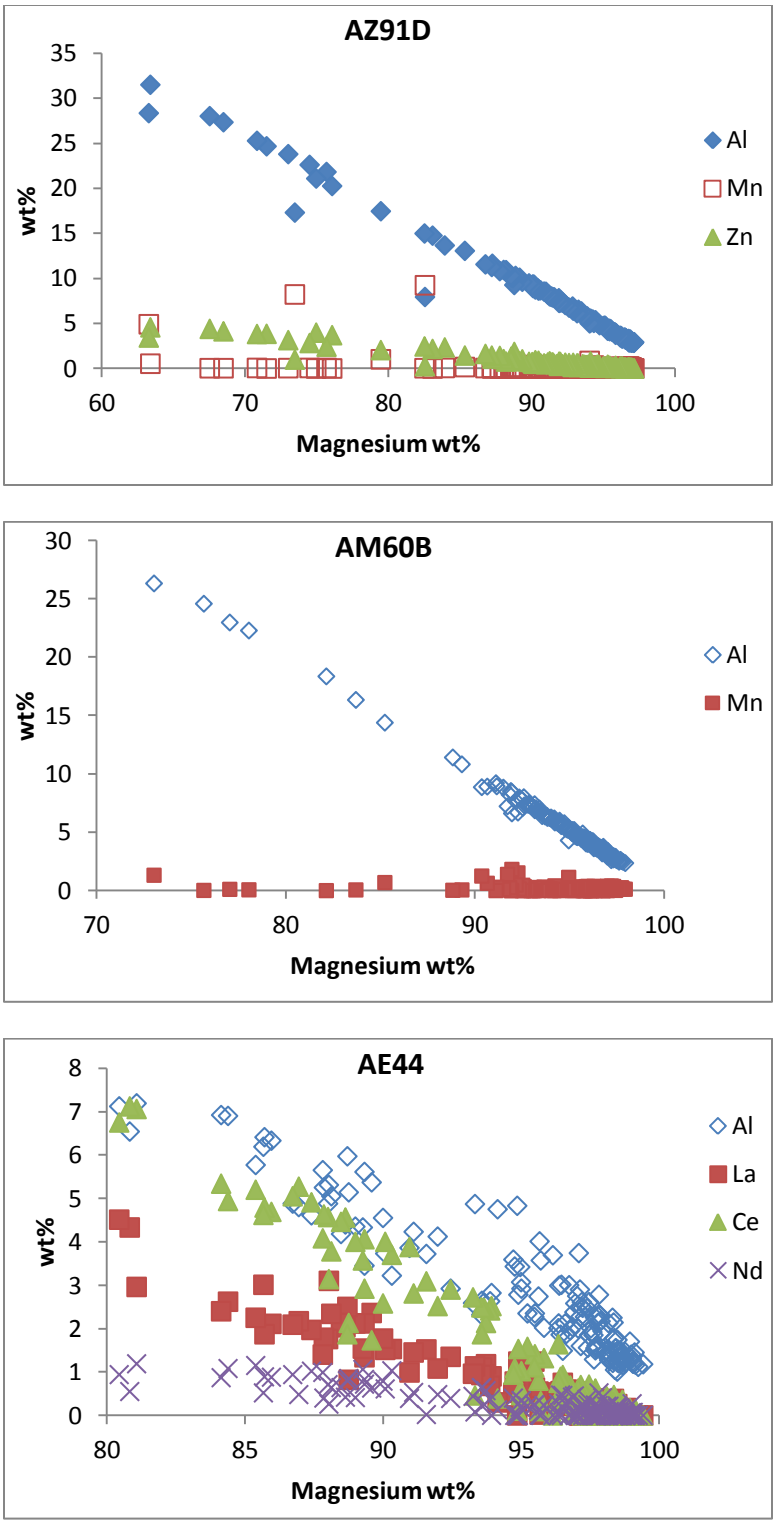

Figure 4-26: Segregation trend in investigated alloys

Location 1 Location 6

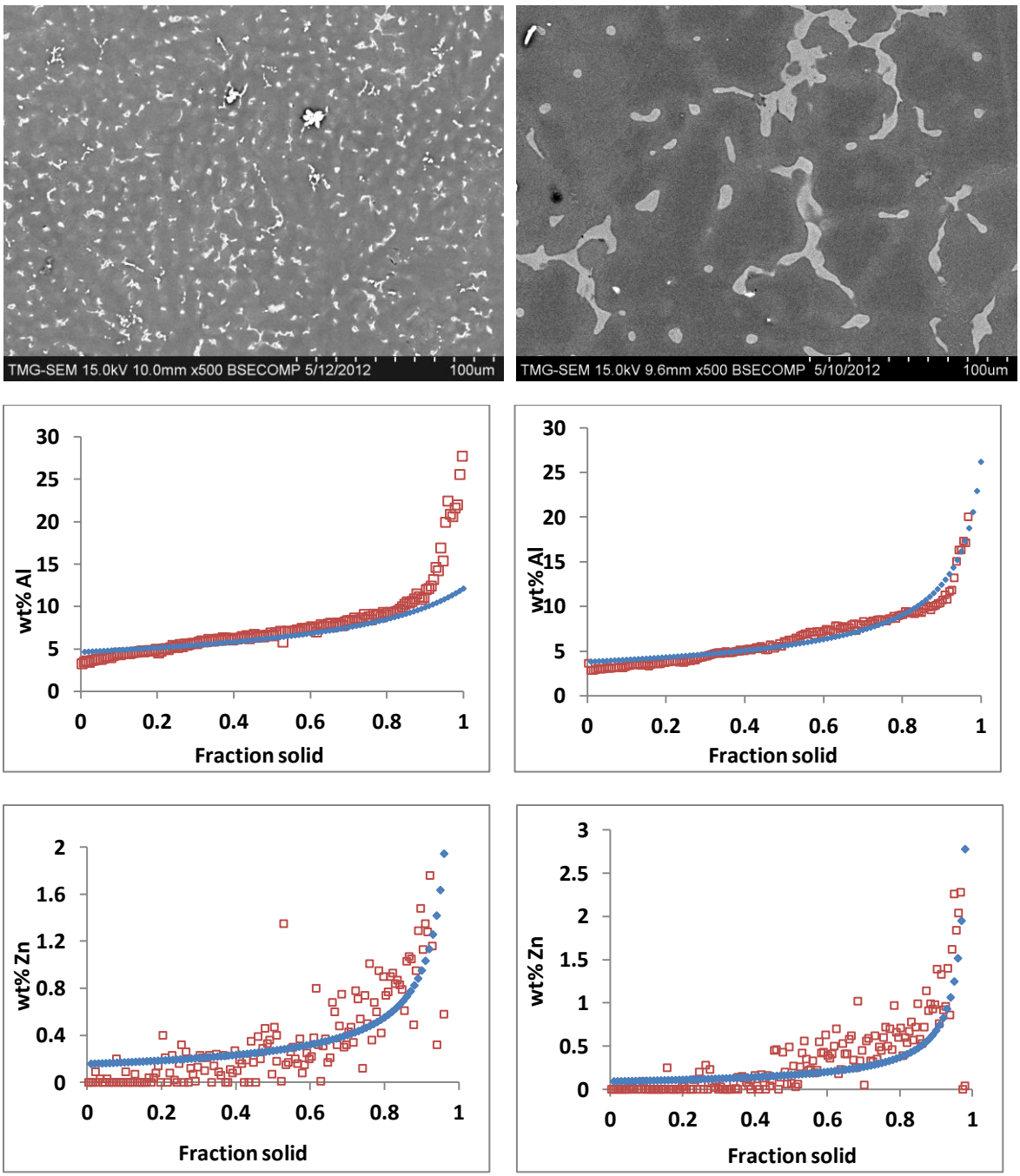

Figure 4-27: Solute redistribution in locations 1 and 6 of AZ91D alloy

Location 1 Location 6

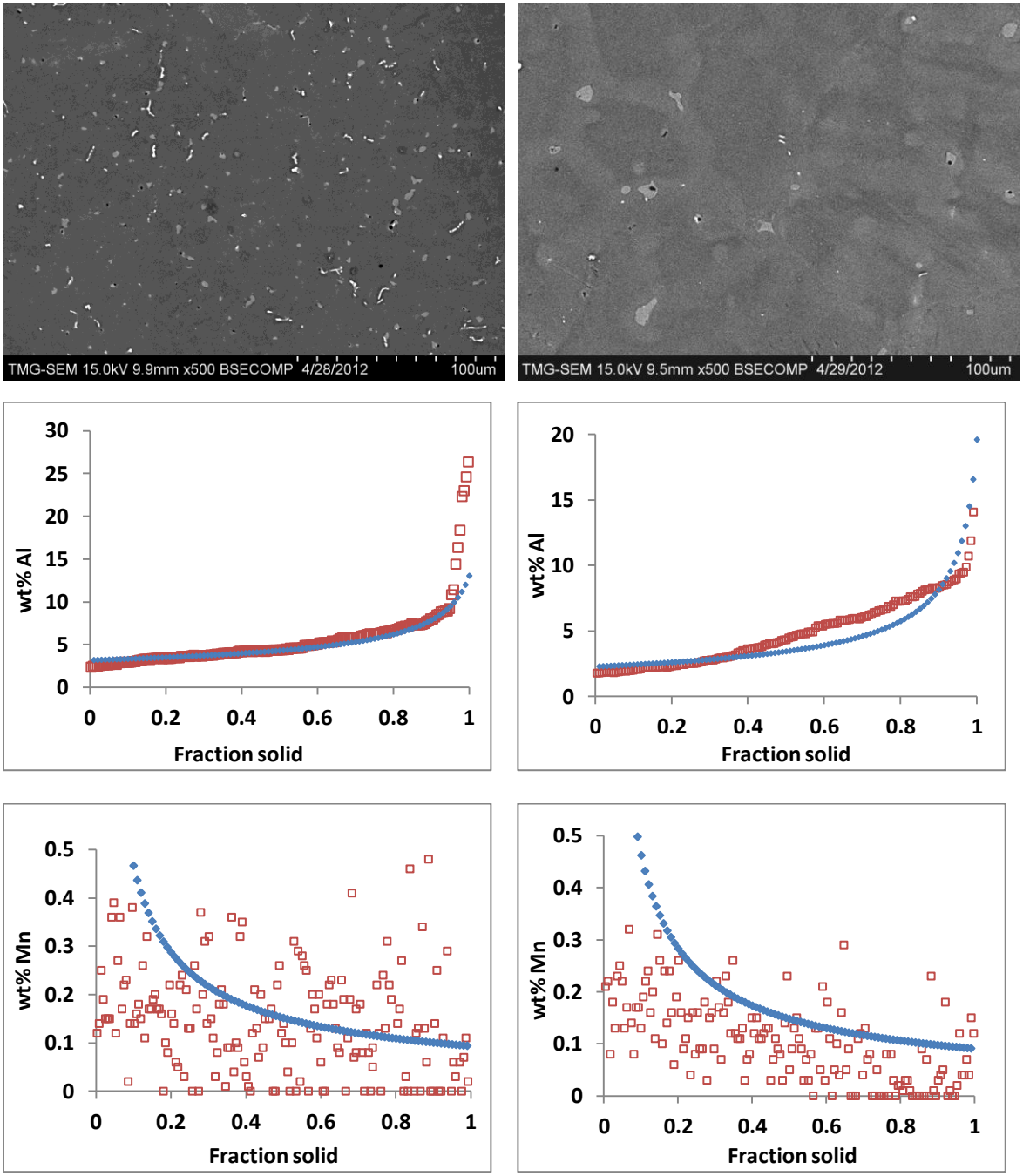

Figure 4-28: Solute redistribution in locations 1 and 6 of AM60B alloy

Location 1 Location 6

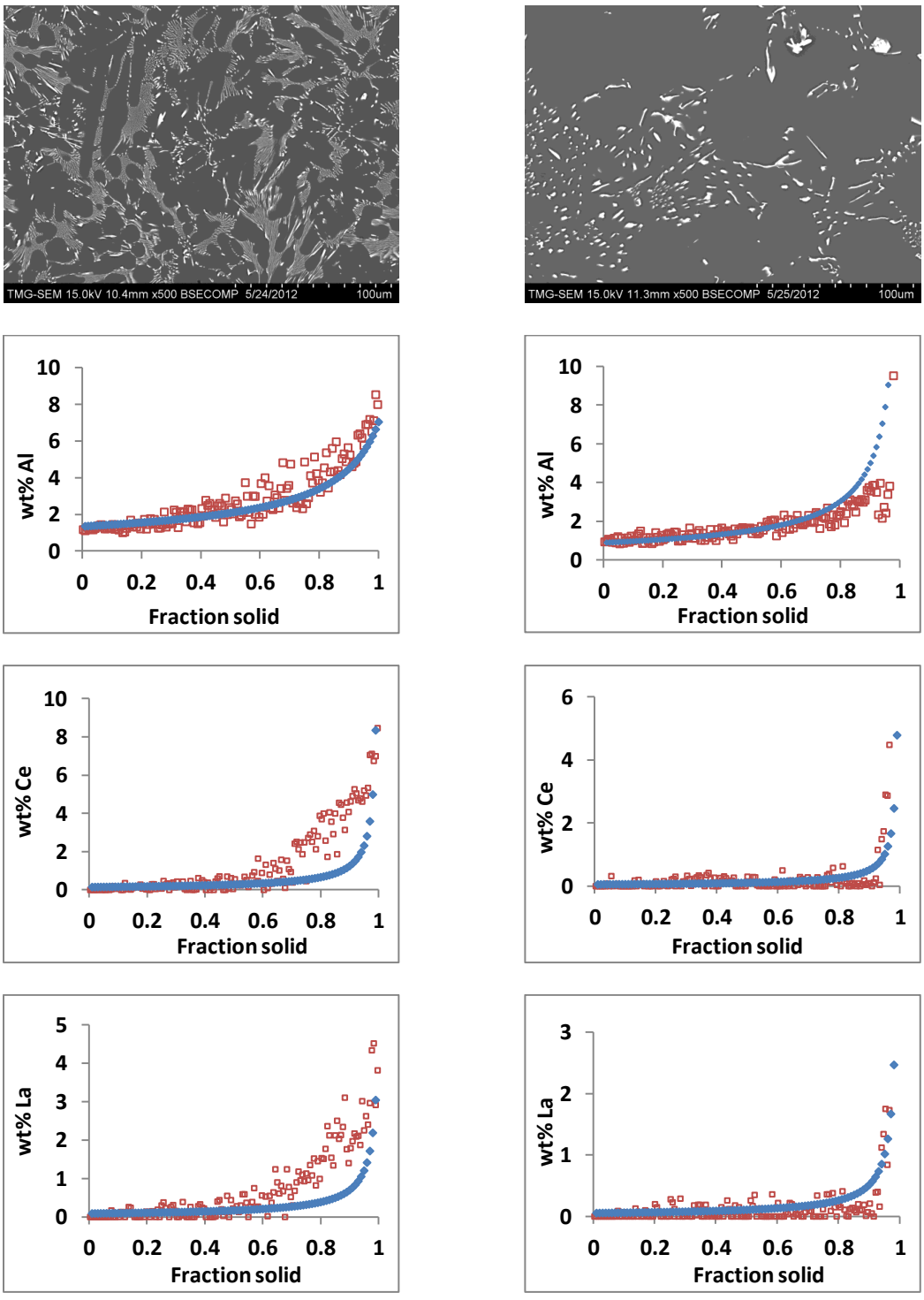

Figure 4-29 : Solute redistribution in locations 1 and 6 of AE44 alloy

In Figure 4-27 to Figure 4-29, the solute redistribution profiles at locations 1 and 6, for major alloying elements of AZ91D, AM60, and AE44 alloys are presented. Solute redistribution profiles at rest of the locations are provided in the appendix (A.7-A.9). In these solute redistribution profiles, open symbols represent the solute profile obtained from the experimental data sorted and treated through WIRS method and the closed symbols represent the curves calculated using Brody-Fleming model. The Brody-Fleming equation for modeling solute redistribution is given below,

$$C_S = KC_0[1 - (1 - 2\alpha K)f_S\,]^{(K-1)/(1-2\alpha K)} \qquad 7$$

The parameters needed to calculate the solute profiles, (composition at any specific point solidified C_S) using this model are dimensionless parameter α, solid fraction f_S, partition coefficient K, and bulk composition C_0 . Detail explanation regarding the calculation of α is provided in section 2.3.3. Secondary dendrite arm spacing and solidification time at each location was used from the experimental data to calculate α.

From the experimentally measured data sorted in WIRS method, values of C_S and f_S can be obtained. Putting these values in the Scheil equation provided below, values of partition coefficient K was calculated.

$$C_S = K.C_0(1 - f_S\,)^{K-1} \qquad 8$$

The average value of K was then used in the Brody-Fleming model for drawing solute redistribution profile. These experimentally obtained values of K for all major alloying

elements are listed in Table 4.3. From the table, it is clear that, the average value of partition coefficient decreases with the decrease of cooling rate.

The average partition coefficient was calculated by curve fitting the equation through the compositional range of 0 to 100% fraction solid. For compositional ranges greater than 80%, there was poor agreement with the Scheil and Brody-Fleming equation. The poor fitting is apparently due to a varying partition coefficient at later stages of solidification.

For AZ91D, average value of K_{Al} at location 1 is 0.53 and at location 6 is 0.43. Shang et al. [87] reported K_{Al}=0.35 and K_{Zn}=0.09 for AZ61 for Scheil and equilibrium cooling. They also reported that for Scheil cooling conditions, the partition coefficient remains constant up to 0.85 fractions solid.

For AM60B, average value of K_{Al} at location 1 is 0.56 and at location 6 is 0.41. Although, in many solute redistribution models the partition coefficient value is considered to be same for Scheil cooling and equilibrium cooling conditions, the results obtained from this experiments clearly indicate that partition coefficient value changes significantly with cooling rate.

For AE44, the average value of K_{Al} at location 1 is 0.34 and at location 6 it decreases to 0.23. For, cerium and lanthanum, their partition coefficient is too small, which confirms their low solubility in magnesium. For cerium, at location 1 the average K is 0.068 and 0.0257 at location 6. For lanthanum, at location 1 the average is 0.075 and at location 6 the average is 0.0283.

Terbush et al. [88], reported that for AX44 alloy, partition coefficient obtained for Al was 0.32. Although, they used Ca instead of rare earth elements, the value of K_{Al} is close to what has been observed at location 1 in the present work. That also makes sense as their

samples were high pressure die cast which experiences very high cooling rate similar to location 1 in this experiment.

Table 4.3: Effective partition coefficient for major alloying elements in the investigated alloys

Location		AZ91D		AM60B		AE44		
		K_{Al}	K_{Zn}	K_{Al}	K_{Mn}	K_{Al}	K_{Ce}	K_{La}
1	Lowest	0.42	0.04	0.48	0.03	0.29	0.02	0.02
	Highest	0.58	0.50	0.68	0.73	0.42	0.14	0.15
	Average	**0.53**	**0.21**	**0.56**	**0.30**	**0.34**	**0.07**	**0.08**
2	Lowest	0.42	0.03	0.39	0.01	0.17	0.02	0.00
	Highest	0.63	0.40	0.49	0.57	0.40	0.18	0.22
	Average	**0.51**	**0.15**	**0.46**	**0.33**	**0.30**	**0.06**	**0.05**
3	Lowest	0.44	0.08	0.36	0.03	0.31	0.02	0.02
	Highest	0.70	0.40	0.60	0.52	0.54	0.10	0.10
	Average	**0.57**	**0.19**	**0.45**	**0.29**	**0.40**	**0.05**	**0.05**
4	Lowest	0.32	0.06	0.30	0.01	0.21	0.01	0.01
	Highest	0.56	0.36	0.47	0.23	0.33	0.13	0.07
	Average	**0.41**	**0.18**	**0.36**	**0.11**	**0.27**	**0.03**	**0.04**
5	Lowest	0.29	0.01	0.35	0.02	0.29	0.01	0.01
	Highest	0.44	0.25	0.51	0.54	0.36	0.07	0.08
	Average	**0.39**	**0.10**	**0.40**	**0.28**	**0.33**	**0.03**	**0.03**
6	Lowest	0.33	0.03	0.31	0.01	0.19	0.01	0.02
	Highest	0.56	0.29	0.55	0.62	0.25	0.05	0.05
	Average	**0.43**	**0.12**	**0.41**	**0.29**	**0.23**	**0.03**	**0.03**

Chia et al. [13] reported the partition coefficient for La and Ce. They calculated these coefficients using the binary phase diagrams of Mg-Ce an Mg-La. According to their calculation, for lanthanum it is 0.0193 and 0.036 for cerium. It is to be noted that as their calculations are based on equilibrium phase diagram, their partition coefficient values are closer to what has been obtained in slower cooling locations in this work. For both cerium and lanthanum, at location 6 the partition coefficient is 0.03.

4.3.2 Area percentage calculation of secondary phases

From the Mg-Al binary phase diagram it can be seen that maximum solubility of Al in Mg is around 12.9 wt.%. On the basis of this assumption, area fraction of β-$Mg_{17}Al_{12}$ phase was measured using the solute redistribution curve of aluminum at different wedge locations for AZ91D and AM60B alloys. The procedure applied for these calculations is presented in Figure 4-30.

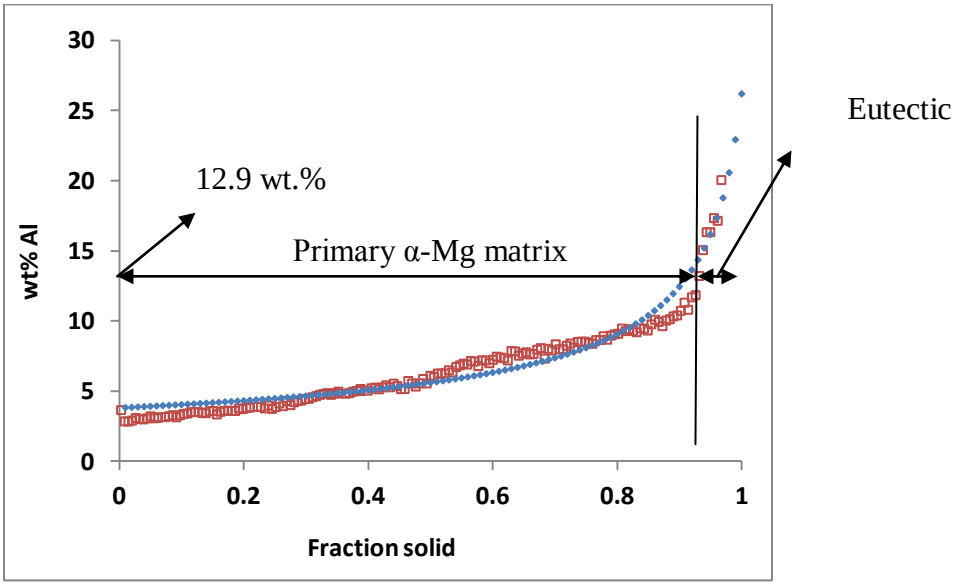

Figure 4-30: Procedure of eutectic fraction calculation using solute redistribution curve

Although, this method offers important information regarding eutectic area percentage, it is less accurate than the results obtained from image analysis. The eutectic area percentage obtained through this method depends on the area and location of points chosen for area scan method. There is high probability that the small area chosen for area scan might not fully represent the microstructural trend. At the same time, it is not possible to area scan larger area of samples due to resource constraint.

From Table 4.4, it can be seen that for AZ91D alloy eutectic area percentage increases with cooling rate up to location 4, then decreases at locations 5 and 6. This trend is similar to the observation of image analysis.

For AM60B, at sample locations 1, 2 and 3, the area fraction was in the range of 3.5-5%. Afterward a reduction was observed at location 5 and 6. At location 6 it was only 2%.

In AE44, the solubility of Al is very low in α-Mg matrix, as most of the aluminum reacts with the rare earth to form precipitates. Solubility of La, Ce and Nd is also very low in the matrix. Hence, maximum solid solubility of La in Mg, 0.8 wt.% was assumed as the beginning of precipitate formation. For AE44 alloy, area percentage of secondary precipitates decreases gradually with cooling rate from 30% at location 1 to 8% at location 6.

Table 4.4: Area percentage of secondary phases measured from solute redistribution curve and image analysis for the investigated alloys

Location	AZ91D		AM60B		AE44	
	Solute curve	Image analysis	Solute curve	Image analysis	Solute curve	Image analysis
1	7.5	5.5	3.4	1.6	30	20.8
2	7.6	5.8	4.0	1.6	24	21.0
3	8	6.5	5.0	2.1	22	17.8
4	10	7.1	4.0	2.1	12	13.2
5	7	6.5	2.7	1.9	12	9.2
6	6.6	4.5	2.0	1.7	8	8.6

Although, area percentage results obtained from solute redistribution curve and image analysis follow similar trend, solute redistribution curve method provides comparatively higher value for all three alloys and at all locations. It might be due to the fact that, in image analysis only the area covered by secondary phase particles are calculated,

whereas in solute redistribution curve method some area of the α-Mg matrix which has high aluminum concentration is also considered.

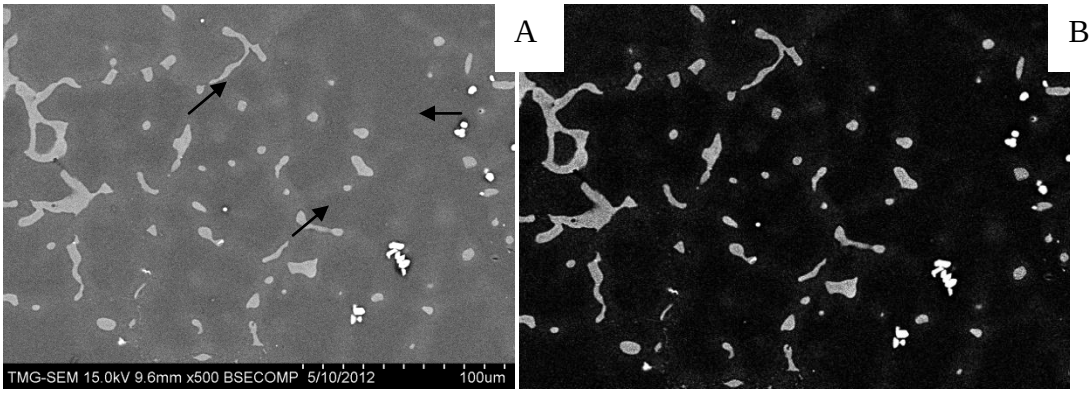

Figure 4-31: (A) BSE image obtained by SEM (B) edited image for eutectic area percentage measurement

The image in Figure 4-31(B) was used for area percentage calculation of secondary phases using image analysis method. As can be seen, the higher Al concentration regions indicated by arrows in Figure 4-31(A) was not included in the image analysis but since high Al concentration was detected, these regions are counted as eutectic phases by the solute redistribution method.

Hehmann et al. [89] reported that solid solubility of Al, La, and Ce in Mg could be increased by rapid solidification method. Hence, increased solid solubility in α-Mg matrix will result in lower area percentage of eutectic phases. In the present experiment, very high cooling rate was observed at locations close to bottom of wedge, therefore it could affect the maximum solid solubility of other alloying elements in magnesium. That means, if accurate values of solid solubility are used to calculate the area percentage, difference between image analysis and solute distribution curve method may become less.

The maximum solid solubility was assumed based on binary phase diagrams. The solubility would be different if diffusion interaction between all the alloying elements of these multicomponent alloys were taken into consideration, which could also affect the area percentage calculation.

4.3.3 Segregation index and minimum composition:

Minimum concentration of aluminum and segregation index at different wedge locations for the three alloys is presented in Table 4.5 . Segregation index is the ratio between minimum composition and bulk composition of an alloying element. To determine the minimum at a specific location, average of the ten lowest compositions were taken. From the table it can be seen that as the cooling rate decreases, the minimum composition decreases, hence the severity of segregation increases.

For AZ91D, as can be seen the minimum concentration of aluminum decreases with the decrease of cooling rate. At location 1, the composition is 2.5 wt.% and in location 6, it drops to 1.8 wt.%.

For AM60B, at location 1, minimum concentration of aluminum is 2.5 wt.% and at location 6 it reduces to 1.8 wt.%. For AE44, at location 1, the minimum concentration of aluminum is 1.1 wt.% and at locations 6 the concentration is 0.9 wt.%.

Segregation index calculated for these three alloys, increases with the decrease of cooling rate from location 1 to 6. Hence, it indicates that microsegregation is more severe at lower cooling rates.

Table 4.5: Minimum concentration of aluminum and segregation index for the investigated alloys at different locations.

	AZ91D		AM60B		AE44	
Location	Minimum of Al	Segregation index	Minimum of Al	Segregation index	Minimum of Al	Segregation index
1	3.63	2.42	2.56	2.23	1.15	3.44
2	3.57	2.47	2.25	2.54	1.21	3.27
3	3.54	2.49	2.19	2.61	1.30	3.04
4	2.90	3.03	1.89	3.01	1.06	3.73
5	3.12	2.82	2.05	2.78	1.07	3.69
6	3.01	2.93	1.84	3.10	0.90	4.39

4.3.4 Segregation deviation:

Segregation deviation was also calculated for all locations of the wedge. The overall deviation from the bulk composition for aluminum is presented in Figure 4-32.

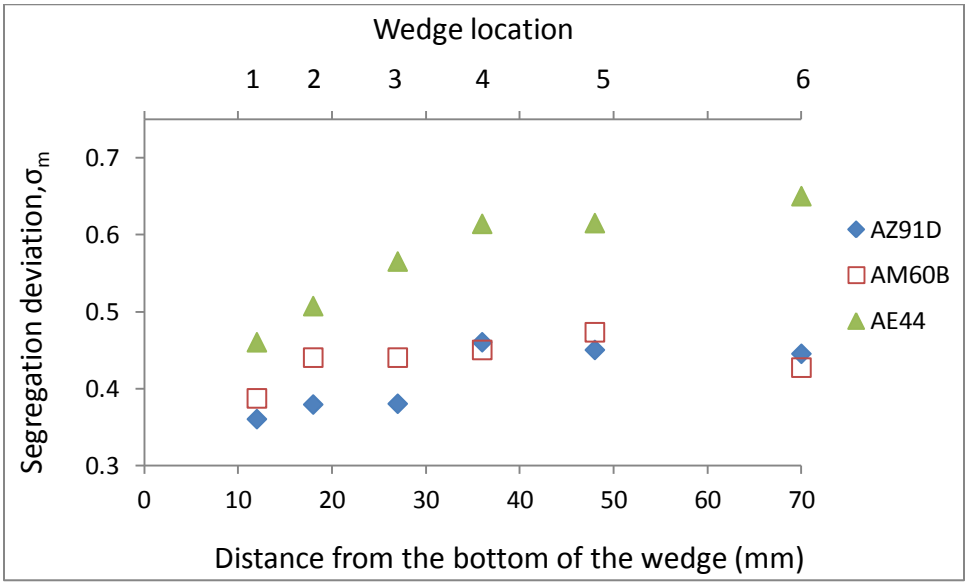

Figure 4-32: Segregation deviation for three investigated alloys

As can be seen from the figure, for AZ91D, from location 1 to 3, the deviation is similar. At locations 4, 5 and 6 segregation deviation is almost identical but higher than what was observed at locations 1, 2, and 3.

For AM60B alloy, from location 1 to location 5, the segregation deviation increases then it slightly decreases in location 6. Thus, that contradicts with the segregation index. The segregation index is high at location 6 but when the deviation is calculated on a broader range the segregation deviation is comparatively lower than other locations.

For AE44 alloy, from the figure it is evident that the segregation deviation increases with decreasing cooling rate. Except a small drop in location 5, location 1 to location 6 follows the trend.

Martorano et al. [39] reported that microsegregation severity is lower for columnar dendrites than for equiaxed ones. It has also been reported that the increase in segregation deviation parameter σ_m, for a change in structure from columnar to equiaxed seems to be constant, approximately 0.11. Consequently, the type of dendritic growth seems to be an important variable to define microsegregation. The greater microsegregation severity observed in an equiaxed dendrite zone compared with that in columnar dendrites might be the result of more homogenization in the latter structure. In the present work, location 1 could be considered as columnar dendrite and location 6 as equiaxed dendrite. The difference in deviation from location 1 to location 6, for AZ91D is 0.08, for AM60B is 0.06, and for AE44 it is 0.19 which is comparable to results observed by Martorano et al. [39].

4.4 Discrepancy between theoretical model and experimental results

There could be several reasons for discrepancy between experimental and theoretical solute redistribution curves.

Compositional analysis was carried out on a small area of the microstructure which was considered to be representative of the entire location of interest. But in wedge casting, the microstructure is not that much consistent as it is in case of directional solidification. Though the inspection area was chosen with utmost awareness, still it could produce some unexpected results, such as sudden drop or increase in the concentration of alloying elements, which defies the trend. Lacaze et al. [37] described this phenomena as "spot" segregation.

In Brody-Fleming model, it was assumed that the dendrites have plate like morphology and the volume element considered for modeling was a perfect parabola. In reality, dendrite arms were parabolic in shape but did not have symmetry with the axis as per the assumption of the model.

Accuracy of the solute redistribution profile depends on the number of data points taken for elemental analysis and the representativeness of the area examined. A large number of data points encompassing a large section of sample, increases the probability of statistically better results. Number of data points to be analyzed and spacing between each point for best results, is a contentious issue. Lacaze et al. [90], in their study used a step size of 10μm along 6 parallel lines, distance between each line was 500μm. In the present study, a total of 150 array points was chosen covering an area of 150 μm x 100 μm with a step size of 10μm. Although, more than 100 points were analyzed as per the suggestion of Gungor [34], but smaller step size was chosen to obtain compositional

variation more accurately within the studied area. Hence, there could be some discrepancy due to covering smaller microstructural area.

It can be seen from solute redistribution profiles of Al, in Figure 4-27 toFigure 4-29, that the theoretical and experimental curves have inconsistency between them generally at the beginning and end of solidification. At the beginning, the inconsistency is due to the negative curvature at low solid fraction as shown in Figure 4-33.

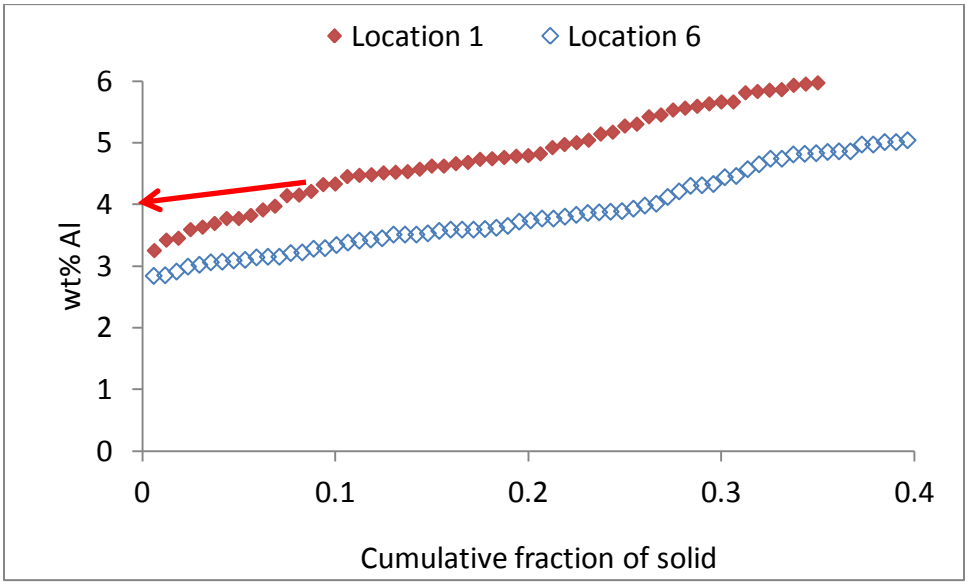

Figure 4-33: Solute redistribution profile of aluminum for AZ91D alloy showing negative curvature

This negative curvature was also reported by Gungor [34], Lacaze et al. [90], and Xie [57]. According to Lacaze et al. [90], limited solute diffusion in the liquid and physical noise of the X-ray emission are the probable causes of this negative curvature in the solute distribution curves. Xie [57] proposed another probable reason regarding the formation of negative curvature. According to his assessment, primary dendrite stems are

liable for this curvature as the minimum solute content of the primary stems are lower than that of the secondary arms. The solute distribution curves are modeled considering the dimension of secondary dendritic arms as they are the dominant ones. Finally, Xie [57] suggested that as numbers of primary dendrite arms are very few in comparison to secondary dendrite arms, therefore this negative curvature could be neglected. Extension of the solute distribution curves neglecting the negative curvature would be more appropriate representation of the minimum solute concentration present in the dominant secondary dendrite arms.

As can be seen from the Figure 4-33, this negative curvature is more prominent in location 1 in comparison to location 6. This is probably due to the fact that at slower cooling rates; there is sufficient time for coalescence and back diffusion which results in convergence of primary stems to secondary stems.

At higher solid fraction, approximately at 0.85-0.9f_S, discrepancy was observed between the experimental results and the model. For slower cooling conditions, back diffusion takes place at the end of solidification which affects the partition coefficient. One possible solution could be using different partition coefficient at 0.85-0.9f_S instead of considering a constant partition coefficient all through the solidification.

Although for most of the alloying elements experimental solute redistribution curves matched to the model with reasonable agreement, manganese redistribution curves for AM60B alloy was exception. The mismatch between modeling and experimental results for manganese might be due to its very low concentration at α-Mg matrix. The bulk concentration was ~0.3wt%, which became less than that in the matrix due to microsegregation. This low concentration could not be detected perfectly by EDS.

Although the theoretical detection limit of EDS is approximately 0.1 wt.% [91] but experimental experience proves that the error margin could be in the range of 1 to 5 wt% depending on the alloy composition.

The uncertainty in partition coefficients and phase diagram data possibly causes the small deviations of the model-calculated concentrations in the center part of a dendrite arm from the experimental data.

4.5 Thermodynamic calculations

Thermodynamic calculations were performed using FactSage to obtain preliminary idea about formation and distribution of phases, weight percentage of alloying elements in the liquid during solidification, and variation of alloying elements in the α-Mg dendrite. These calculations were performed using FSlite database for equilibrium and Scheil cooling conditions. For equilibrium cooling, it is assumed as the slowest possible cooling, allowing back diffusion to the fullest. And for Scheil cooling, though it is not considered as the fastest, it considers no back diffusion; hence it closely resembles fast cooling where rate of back diffusion is very low.

4.5.1 Phase distribution of the alloys

Phase distribution of AZ91D, AM60B, and AE44 alloys for equilibrium and Scheil cooling conditions are presented in Figure 4-34 to Figure 4-36.

Figure 4-34 illustrates the equilibrium and Scheil cooling phase distributions of AZ91D alloy. Solidification starts approximately at 600°C for both the models. But the starting temperature for formation of β-$Mg_{17}Al_{12}$ is different, in equilibrium cooling this phase

starts to form around 400°C and for Scheil cooling it starts much earlier at around 460°C. The relative amount of β-$Mg_{17}Al_{12}$ is lower in Scheil cooling (10 wt.%) in comparison to equilibrium cooling (12 wt.%).

According to thermal analysis of cooling curves at different thermocouple locations of the wedge, solidification starts approximately at 596°C and the solidus is around 420°C. Hence the thermodynamic calculation could predict the beginning of solidification almost perfectly.

Figure 4-35 demonstrates the equilibrium and Scheil cooling phase distributions for AM60B alloy. The first phase that starts to form is Al_8Mn_5, but with very little relative amount in the solidified structure. In both models, the liquid fraction drops significantly at 620°C with the start of solidification. For Scheil cooling condition, β-$Mg_{17}Al_{12}$ phase starts to form at 460°C and for equilibrium cooling it is much later, at 275°C. And the amount of β-$Mg_{17}Al_{12}$ phase is comparatively lower for Scheil cooling, approximately 5 wt.% in contrast to 8 wt.% for the equilibrium cooling condition. The liquidus temperature obtained experimentally (~623°C) match well with the thermodynamic calculations. The solidus temperature obtained through cooling curve analysis (~410°C) is close to the β phase formation temperature (460°C) according to the Scheil model.

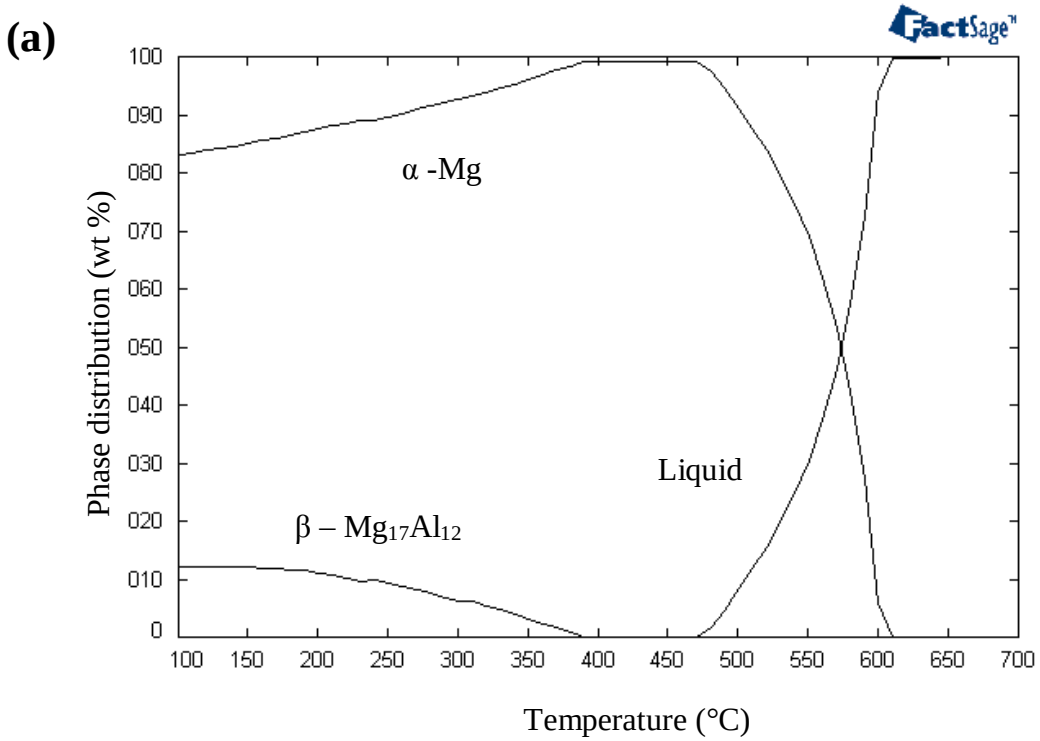

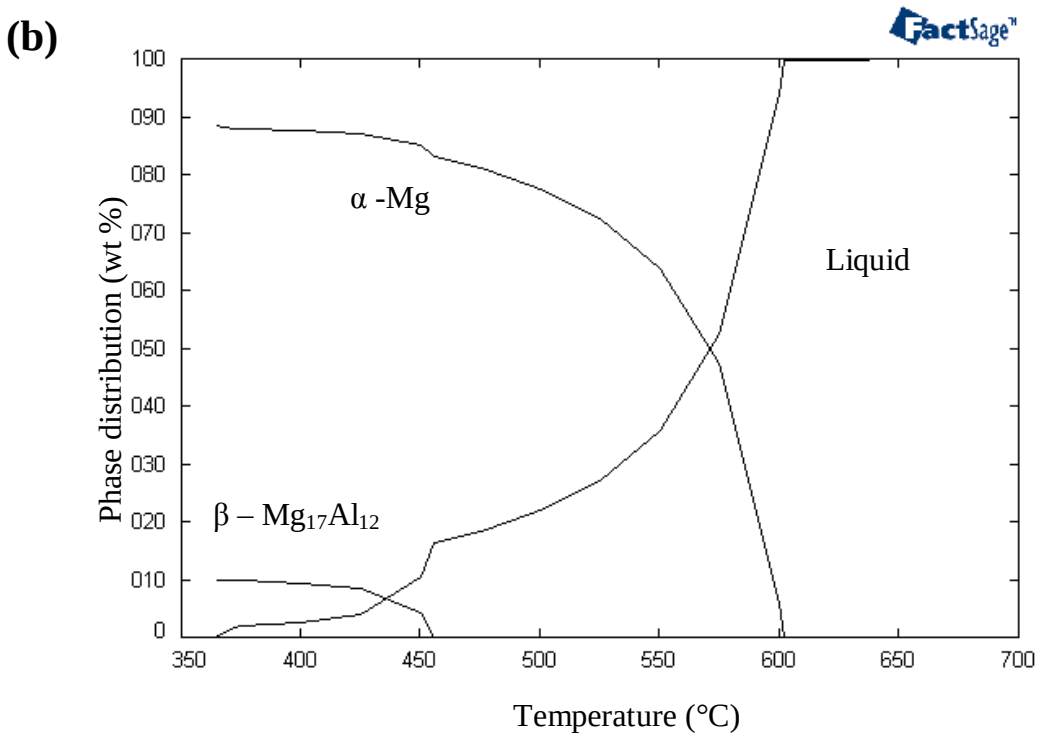

Figure 4-34: Phase distribution of AZ91D alloy (a) equilibrium cooling (b) Scheil cooling

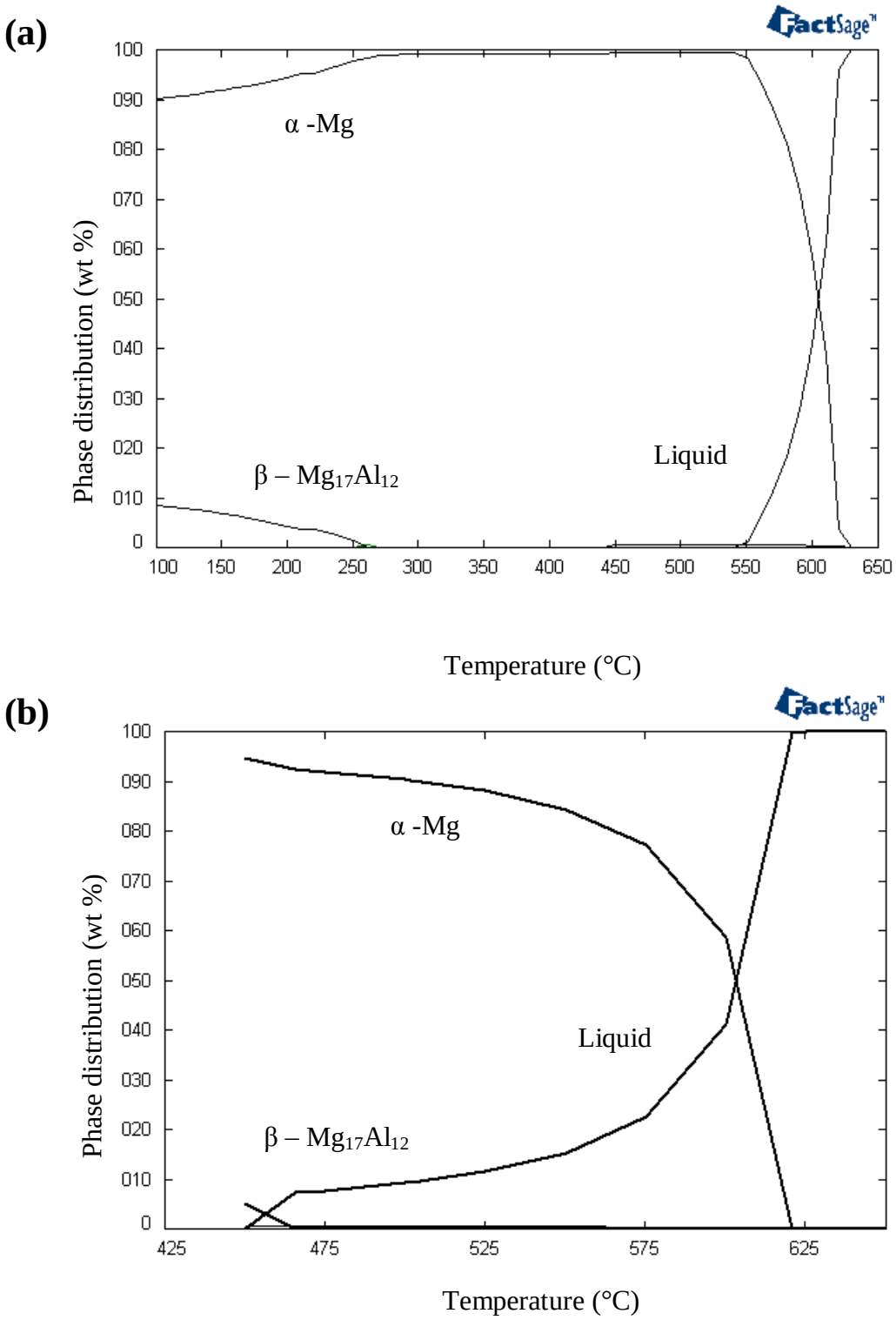

Figure 4-35: Phase distribution of AM60B alloy (a) equilibrium cooling (b) Scheil cooling

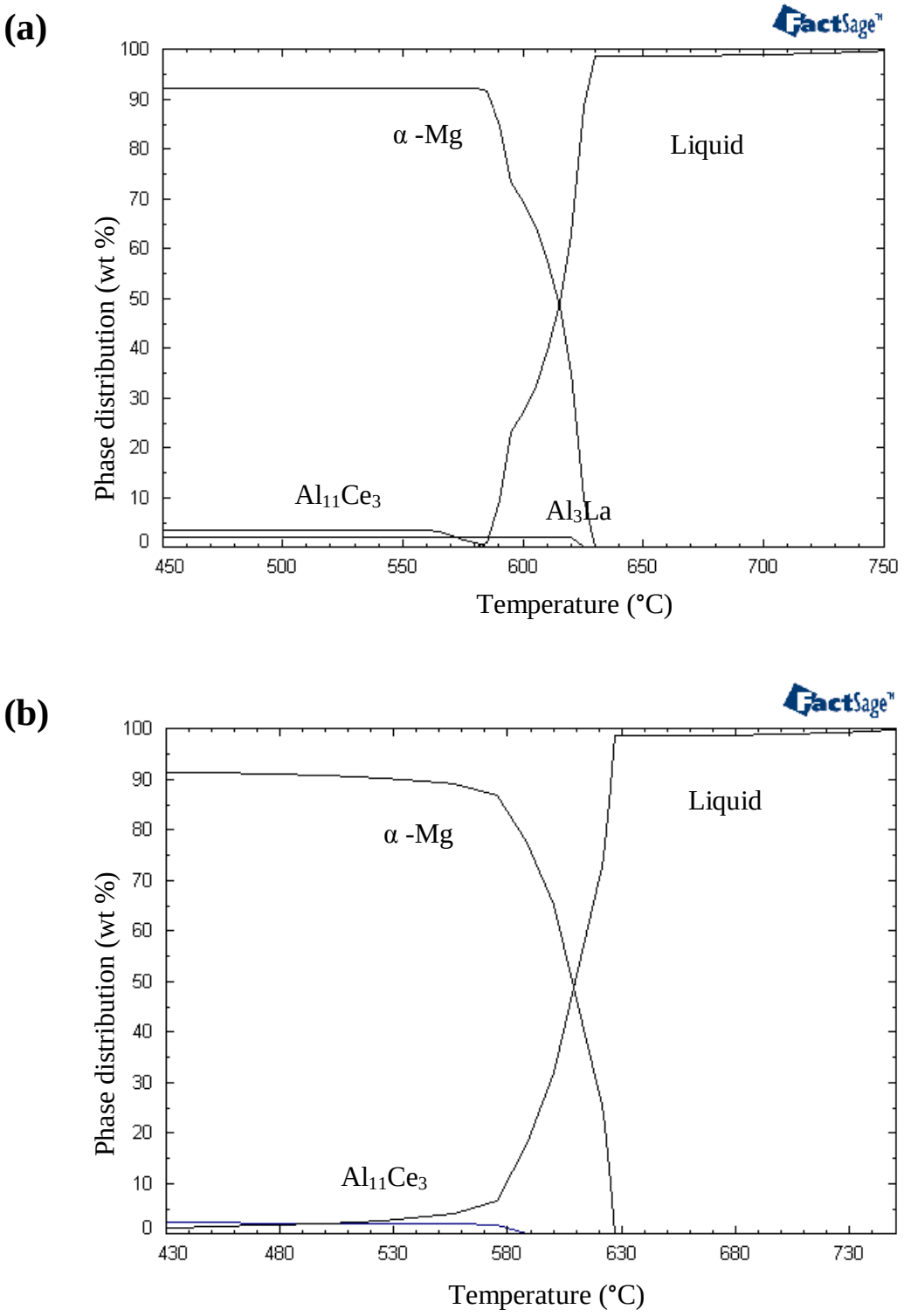

Figure 4-36: Phase distribution of AE44 alloy (a) equilibrium cooling (b) Scheil cooling

The equilibrium and Scheil cooling phase distribution simulation of AE44 alloy is presented in

Figure 4-36. For both models, major change in liquid phase fraction takes place close to 630°C. Phases that are present in the solidified structure are α-Mg, $Al_{11}Ce_3$ and Al_3La. For equilibrium cooling conditions, Al_3La starts to form at around 625°C and formation of $Al_{11}Ce_3$ starts approximately at 580°C.

According to equilibrium cooling model, solidification stops abruptly at approximately 600°C. But for Scheil model, it stops close to 450°C. This difference is due to the extremely small presence of residual liquids at the later stage of solidification. Zhao et al. [92] proposed a cut-off limit of the residual liquid to confront this problem. The cut-off limit has to be chosen sensibly, as a large value of the residual liquid amount may end the simulation early resulting in the complete solidification of the liquid phase even before the simulation reaches the eutectic, whereas a small cut-off limit will produce the eutectic phases. After applying the residual cut-off limit for AE44 alloy the Scheil solidus temperature increased to 530°C from 450°C, which is much closer to the experimental solidus temperature (~570°C).

4.5.2 Distribution of alloying elements in the liquid

Simulations of solute distribution in liquid for the investigated alloys are presented in Figure 4-37 to Figure 4-39. For AZ91D alloy, with the beginning of solidification at around 610°C, the wt% of magnesium drops in the liquid and the concentration of aluminum and zinc increase. This trend continues until it reaches a plateau at around

460°C. At 460° C, the composition of the liquid is 68 wt.% Mg, 27 wt.% Al and 8 wt.% Zn. From the literature and experimental measurements using EDS, it has been confirmed that this indicates the formation of β-$Mg_{17}Al_{12}$ phase. The formation of β-$Mg_{17}Al_{12}$ at 460°C perfectly matches with formation temperature observed in phase distribution of AZ91D alloy during Scheil cooling in Figure 4-34(b).

Figure 4-38 depicts the progression of alloying elements in the AM60B liquid during solidification. For AM60B, solidification begins approximately at 620°C. Similar to AZ91D, wt% of magnesium drops in the liquid and wt% of aluminum increases. But compared to AZ91D, there was very low presence of Zn in the solidifying liquid. Formation of β-$Mg_{17}Al_{12}$ phase takes place around 450°C which was also confirmed by Scheil cooling phase distribution in Figure 4-35(b). At this temperature, magnesium composition is close to 75-76wt% and aluminum composition is around 26wt%. Although for both AZ91D and AM60B, the leading eutectic is β-$Mg_{17}Al_{12}$, there is a significant difference in its composition. In AZ91D, β-$Mg_{17}Al_{12}$ contains 6-8 wt.% Zn, whereas in AM60B presence of Zn in this phase is very little.

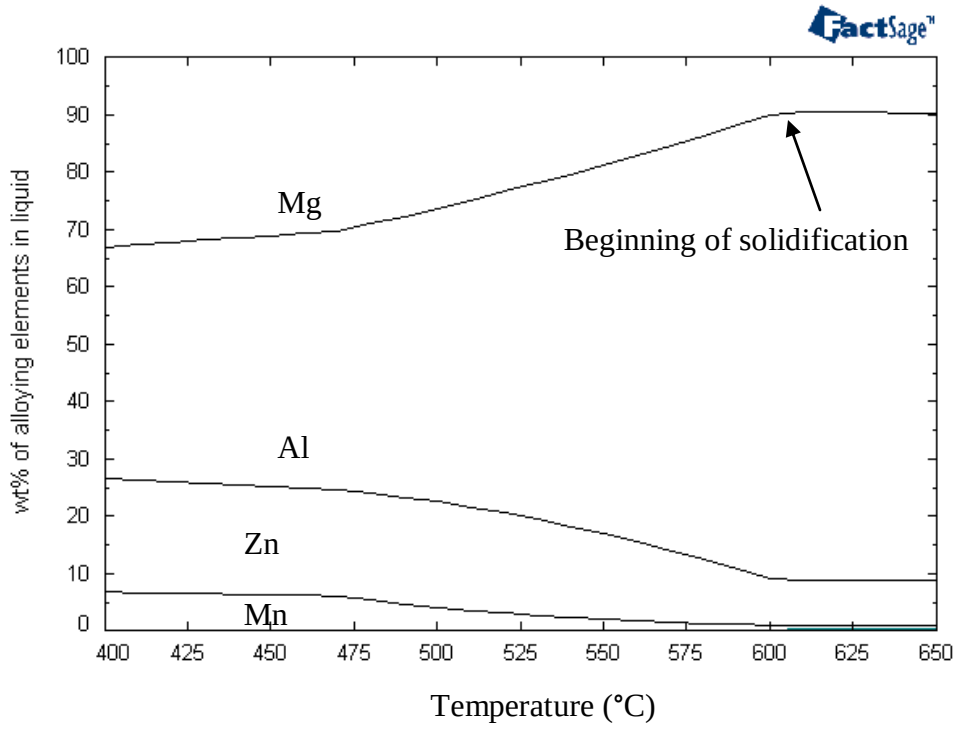

Figure 4-37: Solute distribution in AZ91D liquid

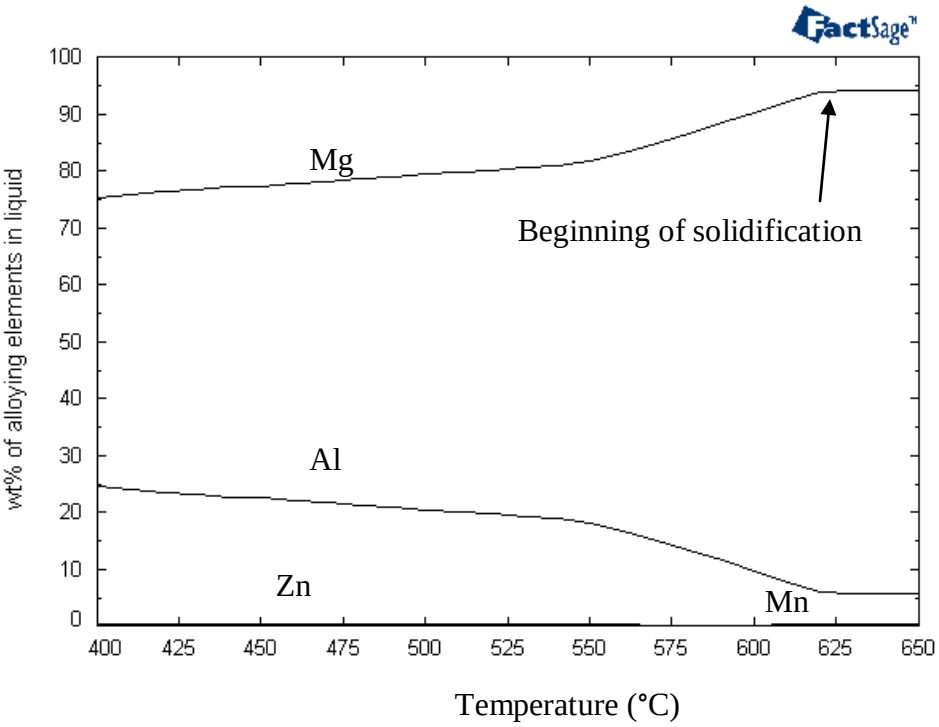

Figure 4-38: Solute distribution in AM60B liquid

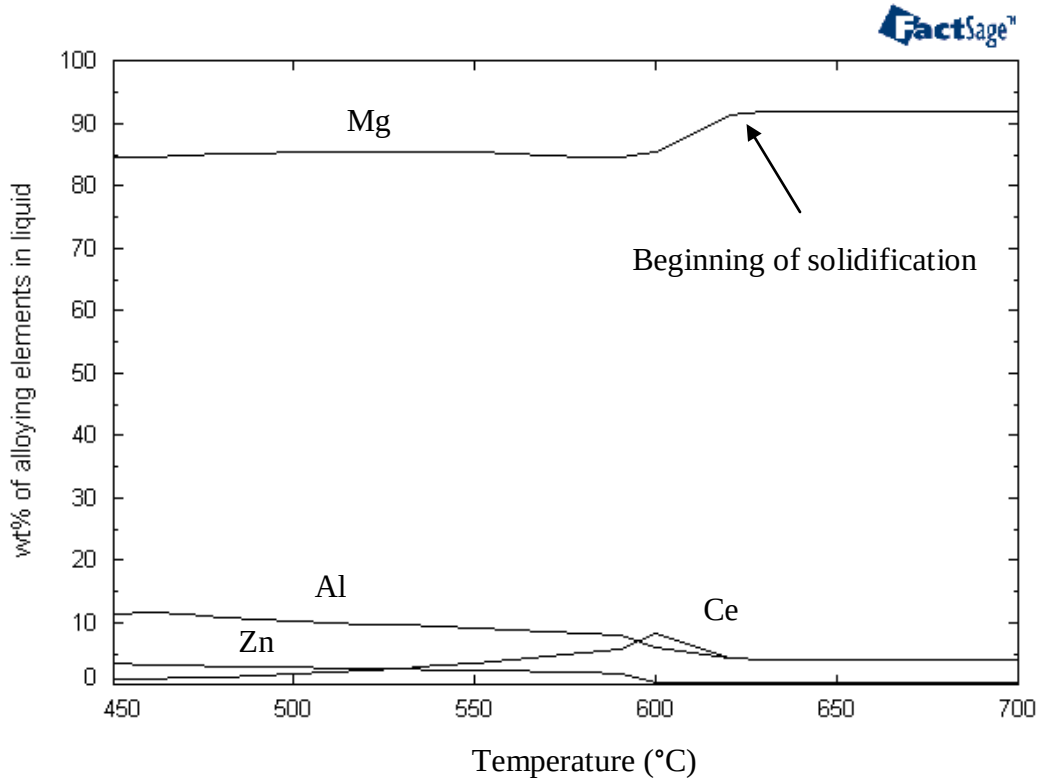

Figure 4-39: Solute distribution in AE44 liquid

Figure 4-39 shows the change of overall liquid composition for the AE44 alloy as the solidification progresses. Solidification starts approximately at 630°C and a compositional plateau is reached at close to 600°C. Shortly before the temperature reaches 600°C, the composition of cerium takes an upward turn, afterwards the concentration of Ce diminishes in the liquid. It is confirmed from Scheil cooling phase distribution presented in Figure 4-36 that at ~600°C $Al_{11}Ce_3$ starts to form. Another point to be noted is, around 450°C, the composition of the liquid is 80 wt.% Mg, 12 wt.% Al, and 4 wt.% Zn. As rare earth elements reacts early with aluminum to form secondary precipitates like $Al_{11}RE_3$ and Al_3RE, aluminum content in the liquid becomes low which suppresses the formation of β-$Mg_{17}Al_{12}$.

4.5.3 Weight percentage of alloying elements in α-Mg dendrite

Weight percentages of alloying elements in α-Mg dendrite were calculated for Scheil and equilibrium cooling to predict the upper and lower limit of the alloying elements in primary magnesium matrix or α-Mg dendrite. Moreover, these calculations also provide indication regarding segregation direction of alloying elements. As discussed in section 4.3, during dendritic solidification due to coring some alloying elements have lower concentration at the center of the dendritic arm and afterward their concentration gradually increase towards the edge of the dendrite. Scheil cooling compositions for different alloying elements are represented by dotted lines while the equilibrium cooling compositions are represented by solid lines.

Figure 4-40, depicts the solute redistribution of alloying elements in α-Mg dendrite of the AZ91D alloy. As mentioned in Table 3.1, there was 8.34 wt.% Al in the bulk composition for the investigated AZ91D alloy. However, according to this calculation, in dendrite periphery or the last region to solidify, would have Al concentration of 8.34 wt.% according to equilibrium cooling model and 5.5 wt.% according to Scheil cooling model. It is to be noted, that equilibrium model considers the bulk composition as the upper limit for dendritic segregation. The model also correctly predicts the opposite segregation trend of manganese. That means the dendrite core would be richer in manganese compared to the dendritic periphery.

Solute redistribution in α-Mg dendrite for AM60B alloy is demonstrated in Figure 4-41. For this alloy the bulk Al composition is 5.70 wt.% but for Scheil cooling at the dendritic periphery it was calculated as 3.8 wt.%. Similar to AZ91D alloy, the upper limit of Al

concentration for equilibrium cooling is same as the bulk composition. Al and Zn concentration is less at the dendrite core then it gradually increases towards the dendrite edge. Manganese follows opposite segregation trend. For manganese the highest composition is 0.2 wt.% for equilibrium cooling and 0.07 wt.% for Scheil cooling. The theoretical detection limit of EDS measurement is ~0.1 wt.% but in reality it is difficult to detect any alloying element which has less than 1wt% concentration in the bulk alloy. Hence experimentally such low values could not be measured, and the error margin in detection was high.

Figure 4-42 demonstrates the solute redistribution profiles of alloying elements of AE44. The bulk chemical composition of the alloy is 3.95 wt.% Al, 0.19 wt.% Zn, 0.30 wt.%Mn, 3.94 wt.% rare earth and the rest is magnesium. Although RE elements are 3.94 wt.% in the initial composition and cerium is present in 2.20 wt.% and lanthanum almost 1.70 wt.%, they are rarely present in the magnesium matrix for both Scheil and equilibrium cooling. Rzychoñ et al. [93] measured the chemical composition of precipitates in HPDC AE44 alloy and they reported that for the magnesium matrix the chemical composition was 97.7 wt% Mg and 2.3 wt% Al. Another important point is unlike AZ91D and AM60B alloys, the composition of aluminum in α-Mg matrix of AE44 at the end of solidification is the same for Scheil and equilibrium cooling. This is probably due to the fact that for AE44 alloy, the solubility of Al in α-Mg matrix is very low compared to AM60B and AZ91D. Hence, the Al concentration remains almost the same for both the cooling conditions.

The segregation trend is also shown in these curves. For Al and Zn, they have lower concentration at the core and then gradually increase towards the dendrite edge and the

trend is opposite for manganese. Mirković et al. [42] carried out microsegregation analysis for AZ31 and AM50, their results support this opposing segregation trend for manganese.

It was observed that for the three alloys (Figure 4-40 to Figure 4-42), the Scheil equation greatly underestimate the concentration at high fraction solid. Elemental analysis conducted at different wedge locations for the three alloys confers that the concentration of Al at high fraction solid is ~26 wt.% for AZ91D and AM60B alloy, and ~8 wt.% for AE44 alloy. But, according to the thermodynamic calculation using FactSage the concentration of Al at the end of solidification is 5 wt.% for AZ91D, 4 wt.% for AM60B, and 2.5 wt.% for AE44 alloy. This underestimation of concentration at high fraction solid possibly takes place because the Scheil equation does not consider the back diffusion phenomenon.

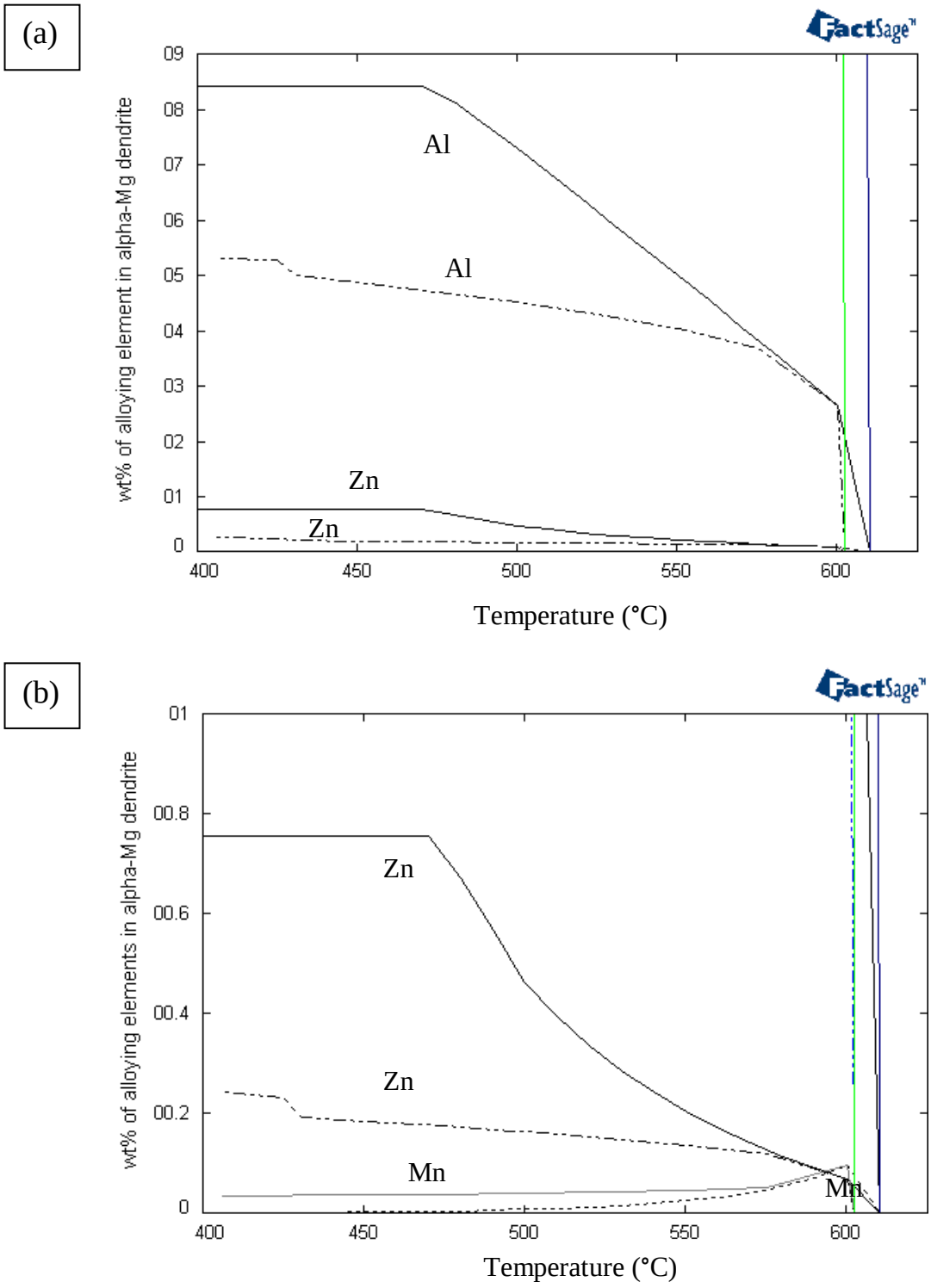

Figure 4-40: (a) Weight percentage of alloying elements in α-Mg dendrite for AZ91D alloy (b) magnified portion of the low concentration of part (a)

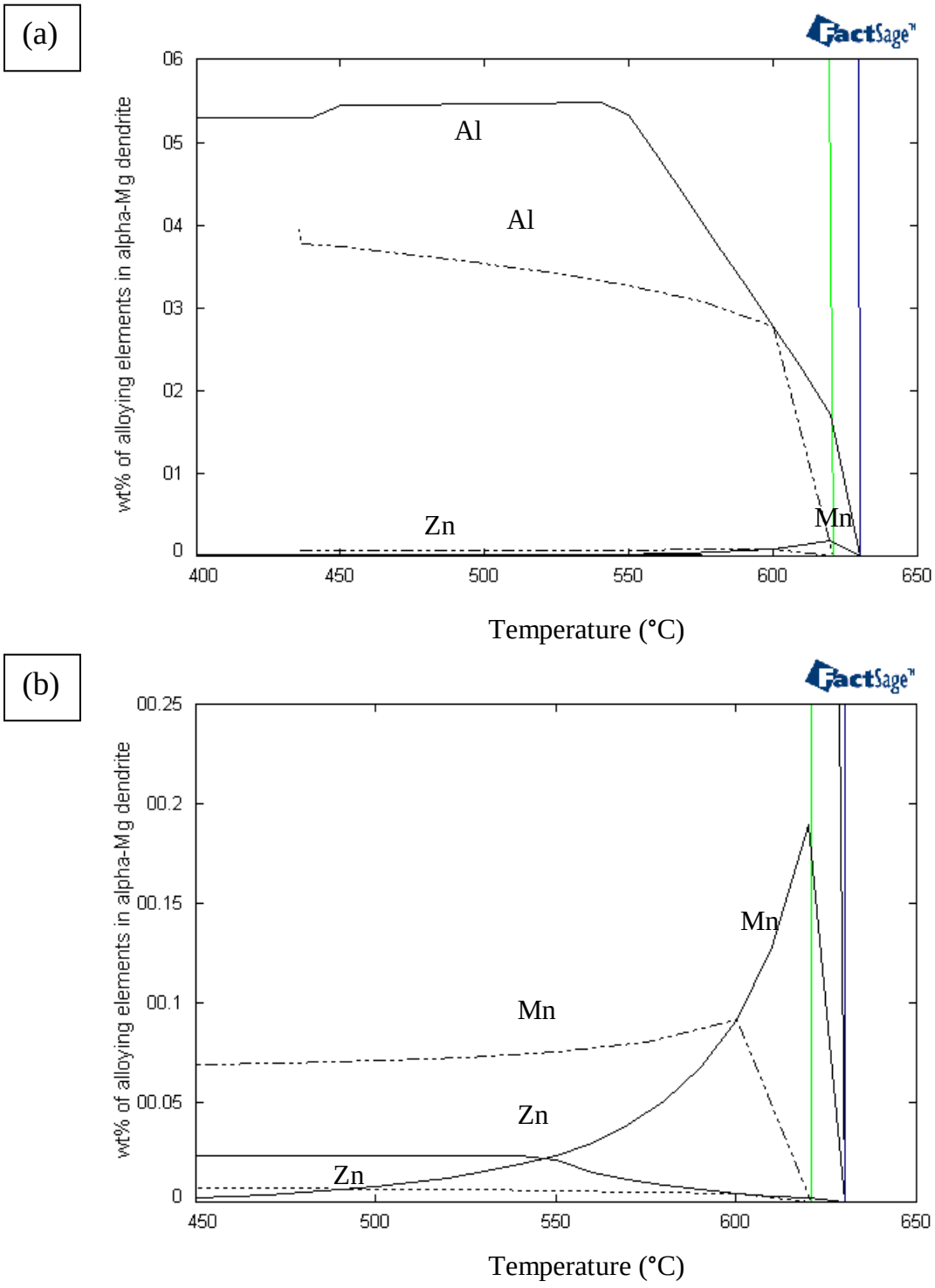

Figure 4-41: (a) Weight percentage of alloying elements in α-Mg dendrite for AM60B alloy(b) magnified portion of the low concentration of part (a)

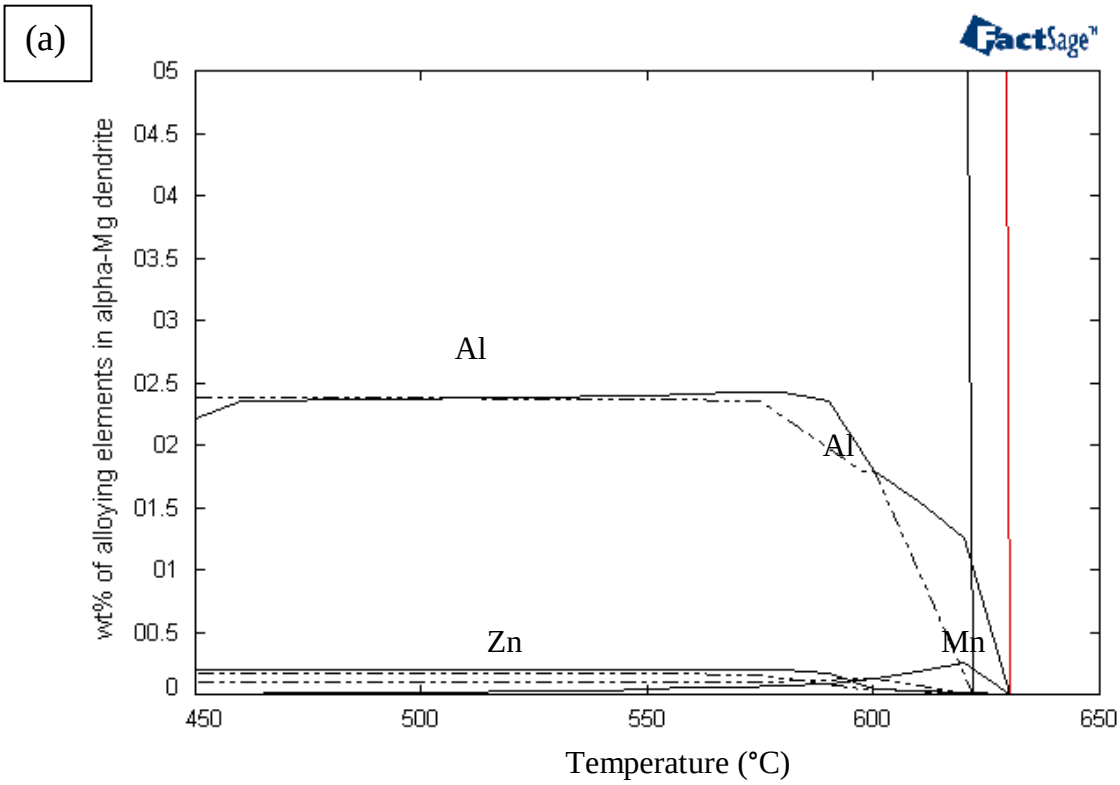

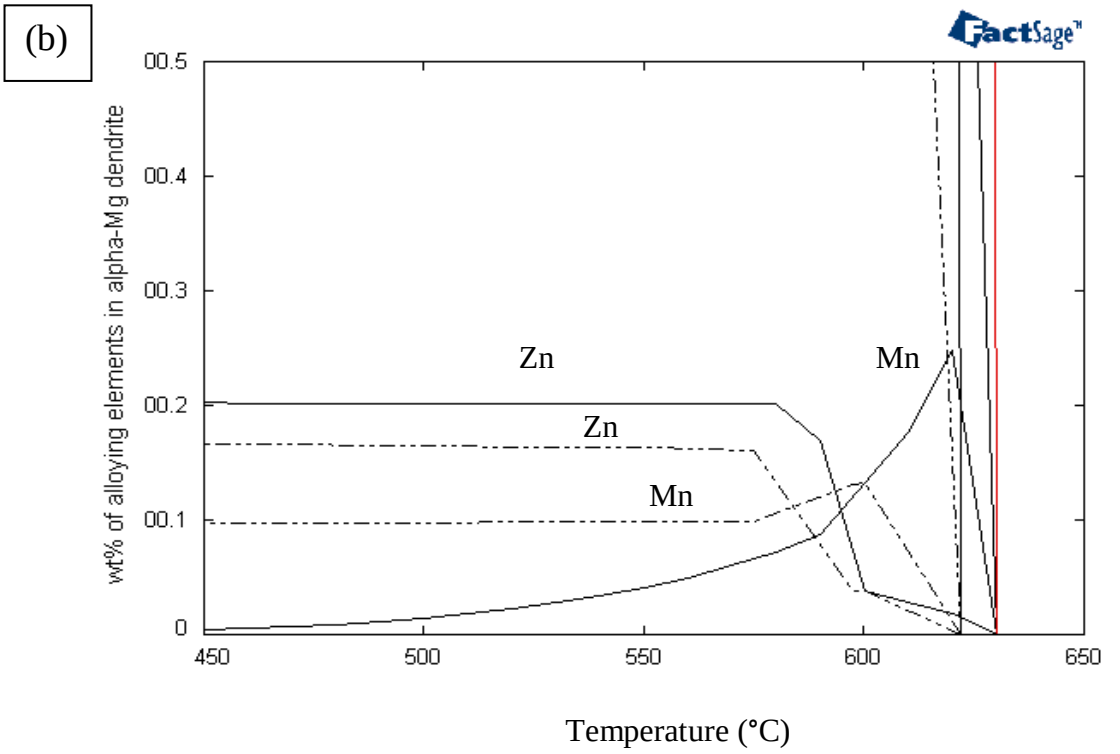

Figure 4-42: (a) Weight percentage of alloying elements in α-Mg dendrite for AE44 alloy(b) magnified portion of the low concentration of part (a)

4.6 Microhardness measurement

Microhardness measurements were carried out in two different patterns to investigate the effect of cooling rate and subsequent microsegregation on microhardness. As can be seen from Figure 4-43 (a), microhardness readings were taken close to the thermocouple positions at all locations of the wedge cast sample. Average of twenty readings was taken at each location. These results are presented in Figure 4-44.

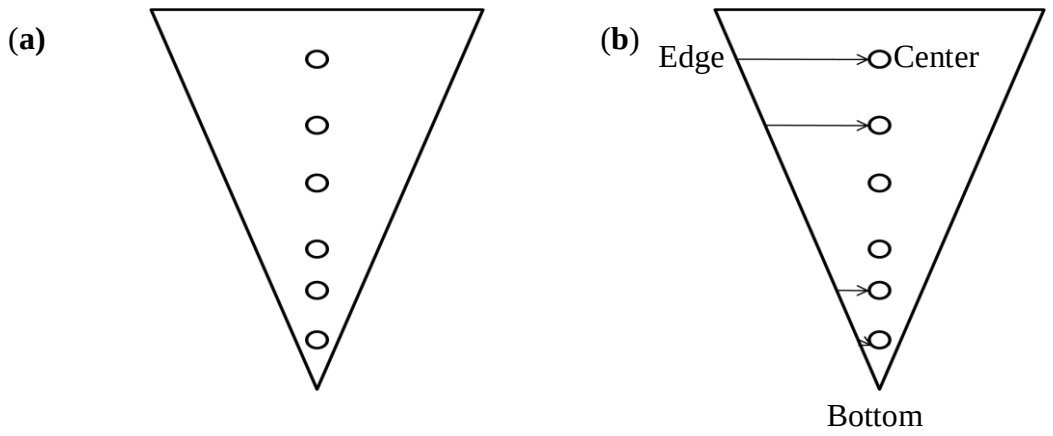

Figure 4-43: Schematic representation of microhardness measurement patterns.

In pattern (b), readings were taken across the sample location (from edge to the center of the wedge). Three sets of measurements were taken at each location. While taking reading across the sample, for locations 1 and 2, distance between each reading was 0.5mm and for locations 5 and 6, there was 1mm distance between consecutive measurements. The aim was to observe the fluctuation of hardness due to the spacing variation of secondary phases which is the result of different cooling conditions in the

various portions of the wedge. In Figure 4-45, microhardness values obtained in pattern (b) is presented for the three investigated alloys. For ease of comparison, results of locations 2 and 6 are presented here. Hardness values of the rest of the locations are provided in appendix (A.10-A.12).

Pattern A: Microhardness measurements have strong correlation with the variation of microstructure. In Figure 4-4, Figure 4-11, and Figure 4-18, micrographs of these three alloys close to thermocouple positions at different wedge locations are presented. As can be seen from these micrographs, at locations 1 and 2, more secondary phase particles are present in comparison to locations 5 and 6. As locations 1 and 2 have lower secondary dendrite arm spacing, distance between these particles are shorter compared to location 6. The secondary phases are harder than the Mg matrix. From Figure 4-44, it can be seen that for the three alloys, at locations close to bottom of the wedge, hardness values are higher. This is because at locations 1 and 2, secondary phase particles are closely positioned. Whereas at location 6, with increased secondary dendrite arm spacing, when the indenter falls in the matrix only it gives much lower hardness, which eventually reduces the average hardness value.

As can be seen from Figure 4-44, microhardness values for AZ91D are in the range of 60-70Hv, for AM60B in the range of 55-60Hv and for AE44 the range is 54-60Hv. For AM60B, comparatively higher values are observed in locations 1 and 2, after that hardness values are almost same for rest of the locations. Similarly, for AE44 alloy, hardness values were very close for all the locations, except for location 1.

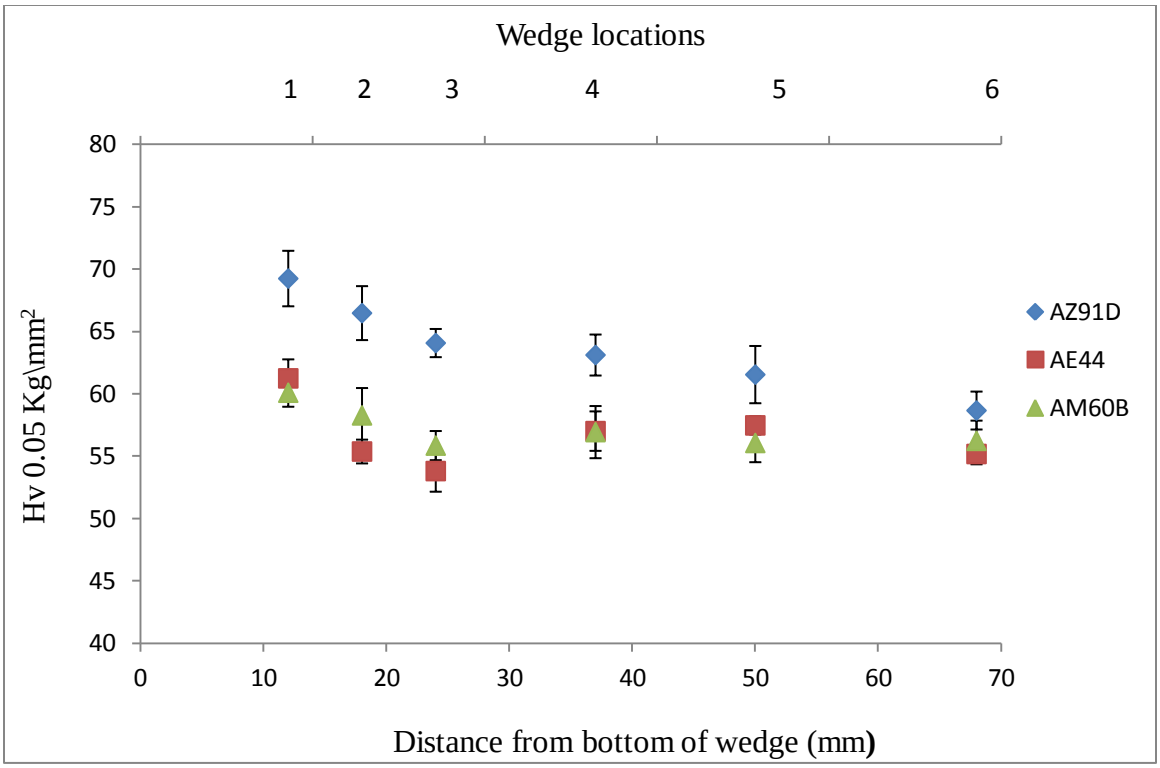

Figure 4-44: Microhardness measurements at the middle of the wedge at the thermocouple locations for the three investigated alloys (pattern A)

Pattern B: Microhardness measurements were obtained from the edge to the center of the wedge. These measurements can also be related to microstructural variation. Specific portions of the microstructural maps are presented in appendix (A.1-A.3) for the investigated alloys. At each location, three micrographs are demonstrated to point out the microstructural differences among edge of the wedge, transition from columnar to equiaxed region, and the center of the wedge. From these micrographs, it is obvious that for all three alloys, closer to the mold wall secondary phase particles are densely distributed. As a consequence, in Figure 4-45, it can be observed that for all three alloys closer to the wedge edge microhardness value is comparatively higher. It should also be noted that comparatively less variation is observed in hardness values across the sample

for location 2. This trend can be explained with the help of micrographs presented in Figure 5-4 toFigure 5-6 (location 2-AZ91D alloy), Figure 5-22 toFigure 5-24 (location 2-AM60B alloy), and Figure 5-40 to Figure 5-42 (location 2-AE44 alloy). It is obvious from these micrographs that no significant change in spacing among secondary phase particles takes place from the edge to the center of the wedge.

At location 6, close to the mold wall (Figure 5-16,Figure 5-34, andFigure 5-52) the morphology was columnar for the three alloys. In the middle of the wedge (Figure 5-18,Figure 5-36, andFigure 5-54) at this location the morphology was equiaxed and the secondary particles more dispersed. The effect of this kind of morphology is clearly reflected on the hardness profile measured across the sample at this location. That is why, so much fluctuation in hardness is observed close to the center of the wedge. No definite skin or core was observed as in high pressure die cast alloys. Hardness value was slightly higher close to mold wall, but skin area was not clearly defined.

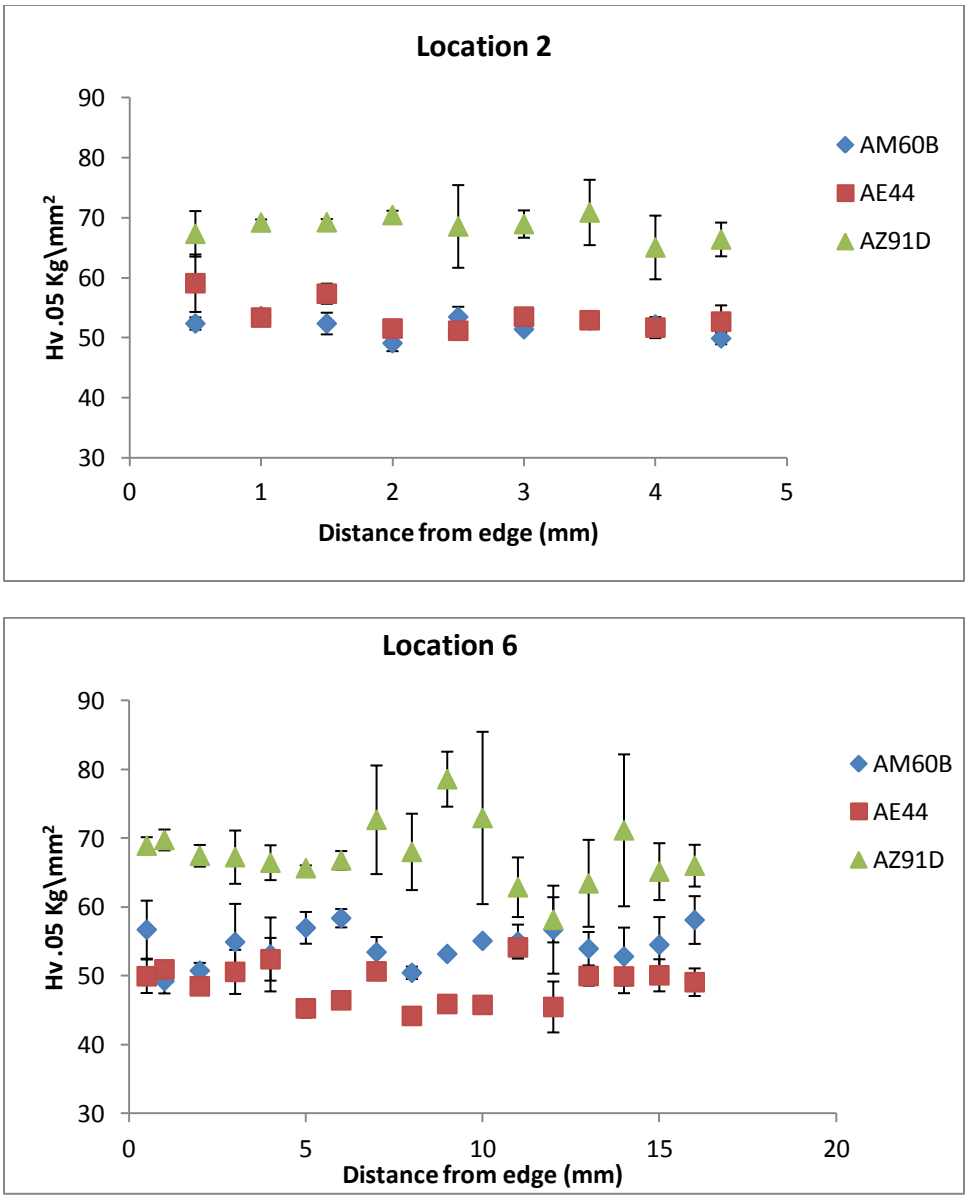

Figure 4-45: Microhardness measurement across the sample at locations 2 and 6 for AZ91D, AM60B and AE44 alloys (pattern B)

As can be seen from Figure 4-45, at location 2 for all three alloys less fluctuation in hardness values is observed. This is due to the fact that eutectic phase particles are more densely placed at this location. At location 2, thickness of half of the wedge is around 4mm. It can be observed from the hardness profiles at location 6 for AZ91D and AE44

alloys, for the first 4mm distance from the edge, these profiles have similarity with location 2. This is because these locations have resemblance in microstructural features. For AM60B alloy, at location 6 fluctuation in hardness profile did not quite match with location 2 even at locations closer to mold wall. This could be attributed to the fact that AM60B has comparatively lower percentage of eutectic in the microstructure (1-2 area% compared to 5-7 area% for AZ91D, and 10-20 area% for AE44), which means the probability of the indenter touching the softer matrix is higher.

For the three alloys, at location 6, closer to the center of the wedge (approximately at a distance of 8-9mm from the edge) the fluctuation of hardness values at the same location becomes more obvious. For example, at these positions some hardness values are observed with error margin of approximately ±7Hv, which indicates the presence of dispersed alternate layer of soft matrix and hard secondary phase particles. Another point is, as the distance between secondary phase particles increase with the decrease of cooling rate, the hardness value of the soft matrix also decreases. For AZ91D, at location 2 the lowest hardness value observed is 65Hv, whereas at location 6 the lowest hardness value is 58Hv. If hardness value of secondary phase particles is considered to be constant, then obviously this change in lower hardness value should be attributed to changing softness of the matrix with cooling rate. Similar trend is also observed in AE44 alloy, lowest hardness value at location 2 is 50Hv, whereas at location 6 the lowest value observed is 42Hv.

4.7 XRD results

XRD analysis was carried out close to the six thermocouple locations for the three alloys to relate formation of phases with microsegregation. The objective was to detect the phases and their relative amount with varying microsegregation. For locations 1 and 6, three set of analyses were carried out at each location, to calculate the error margin.

XRD patterns of these three alloys are presented in Figure 4-46. For AZ91D and AM60B alloys, α-Mg is the dominant phase, and the other phase present in detectable amount is β-$Mg_{17}Al_{12}$. For AE44 alloy, the phases present were α-Mg and $Al_{11}RE_{3.}$ Crystal structure of $Al_{11}Ce_3$ was used to identify $Al_{11}RE_3$ including $Al_{11}Ce_3$ and $Al_{11}La_{3.}$

Weight percentages of secondary phases at these locations were also calculated from XRD results using Rietveld method. These values are presented in Table 4.6. Weight percentage of these phases calculated for equilibrium and Scheil cooling using FactSage is also provided. It should be noted that for the three alloys wt% of secondary phases is lower for Scheil cooling in comparison to equilibrium cooling. For AZ91D and AM60B, wt% of β-$Mg_{17}Al_{12}$ obtained through XRD analysis is much lower in comparison to the theoretically calculated values. In all cases, weight percentage of the secondary phases increase with decreasing cooling rate.

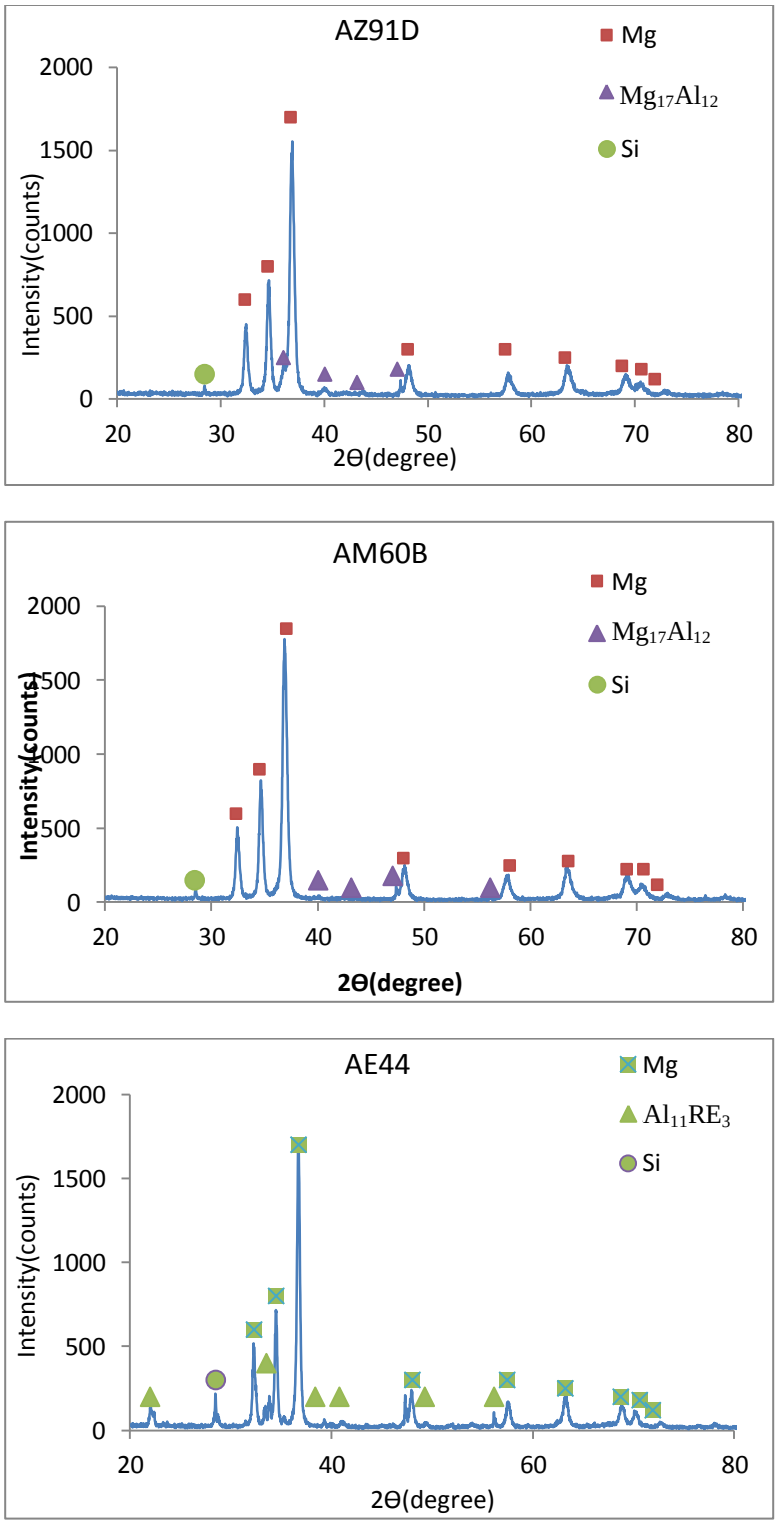

Figure 4-46: XRD pattern for three alloys

Table 4.6: wt% of secondary phases measured by XRD analysis

	AZ91D	AM60B	AE44
	wt% $Mg_{17}Al_{12}$	wt% $Mg_{17}Al_{12}$	wt% $Al_{11}RE_3$
Location 1	1.1±0.3	0.8±0.2	4.0±0.3
Location 2	1.4	1.0	4.0
Location 3	1.3	1.1	4.2
Location 4	2.0	1.3	4.3
Location 5	2.5	1.4	4.6
Location 6	2.6±0.4	1.4±0.3	4.4±0.5
Equilibrium cooling	12	8.0	4.0
Scheil Cooling	10	5.0	3.0

Chapter 5 **Summary and future work**

5.1 Summary

Systematic quantitative microsegregation analyses were carried out for three commercially important magnesium alloys AZ91D, AM60B and AE44 using wedge casting method. Changes in microstructural and morphological features due to variation in cooling rate at different locations of the wedge casting were analyzed. Elemental analysis was carried out in the vicinity of thermocouple locations for all three alloys to obtain the microsegregation trend, solute redistribution profiles, and elemental partition coefficient. Apart from that, solute redistribution profiles were also drawn using Brody-Fleming model, and were compared with the experimentally obtained curves.

For the three alloys, area percentage of secondary phase particles was comparatively more in areas closer to the mold wall at all wedge locations. Secondary dendrite arm spacing increased gradually with the decrease of cooling rate. Average and maximum area of the secondary phase particles increased significantly with decreasing the cooling rate. For AZ91D, β-$Mg_{17}Al_{12}$ phase had partially divorced morphology at fast cooled locations of the wedge and fully divorced morphology at slow cooled locations. For AE44, the secondary precipitates had cluster like morphology at faster cooling rate, and gradually became more dispersed with slower cooling rate.

Columnar to equiaxed transition was not very clear cut as it is in the case of directional solidification. In general, it can be said that at locations 1 and 2, the morphology of the

dendrites were basically columnar. At locations 3 and 4, there was mixed morphology and at locations 5 and 6, fully equiaxed morphology was observed. Microsegregation was more pronounced in equiaxed morphology which is the consequence of slower cooling rate and prolonged back diffusion.

Elemental distribution in α-Mg dendrite obtained through thermodynamic calculation did not match with experimentally obtained values. The lower limit or the initial concentration of the alloying elements could not be clearly identified from these calculations. The predicted upper limit was much lower than the experimentally obtained values.

Experimentally obtained elemental partitioning coefficients and solute redistribution profiles for the major alloying elements at different cooling rates should be very important for microstructural simulation models of these alloys and for the validation of existing models, which would be of great importance for optimizing the casting procedure. Elemental partitioning coefficient of major alloying elements of the investigated alloys decreased with the decrease of cooling rate. Experimentally obtained solute redistribution profiles matched reasonably well with theoretically calculated profiles except at very low solid fraction.

5.2 Recommendations for future work:

- The objective of this research was to find a trend or correlation between cooling rate and microsegregation behavior of magnesium alloys. The cooling rates obtained in gravitational wedge casting were much lower than high pressure die

casting. Hence, it would be interesting to measure the microsegregation trend for high pressure die casting with varying pressure.

- Usually microsegregation measurements are done on directionally solidified samples. According to the literature, directional microsegregation experiments have been done on AZ31 and AM50 alloys. Thus, it would be important to carry out directional solidification experiments for AZ91D, AM60B and AE44 alloys and compare the trend with wedge cast samples.
- Regarding microhardness measurement, all the readings were obtained manually at a distance of 0.25 mm. It is very much time consuming to obtain readings at smaller spacing. Though it gives some indication regarding the microhardness pattern, it would be much easier with an automated microhardness machine to take larger number of readings at much smaller interval.
- Using sophisticated atom probe compositional analysis techniques, investigate the influence of compositional effects on element segregation on an even finer scale (for both as-cast and heat treated materials).

References

1 Boby, A., Pillai, U., Pillai, B. and Pai, B. Developments in Magnesium Alloys for Transport Applications–An Overview. *Indian Foundry Journal*, 2011, **57**(1), 30.

2 Beals, R.S., Tissington, C., Zhang, X., Kainer, K., Petrillo, J., Verbrugge, M. and Pekguleryuz, M. Magnesium global development: Outcomes from the TMS 2007 annual meeting. *JOM Journal of the Minerals, Metals and Materials Society*, 2007, **59**(8), 39-42.

3 Aghion, E., Bronfin, B. and Eliezer, D. The role of the magnesium industry in protecting the environment. *Journal of Materials Processing Technology*, 2001, **117**(3), 381-385.

4 Davies, G. *Materials for automobile bodies*. (Butterworth-Heinemann, 2003).

5 Kulekci, M. Magnesium and its alloys applications in automotive industry. *The International Journal of Advanced Manufacturing Technology*, 2008, **39**(9), 851-865.

6 Mao, H., Chandrasekar, V., Murray, M., Mobley, C., Rodrigo, D., Esdaile, R. and Brevick, J. *Microstructural characteristics of die cast AZ91D and AM60 magnesium alloys*. (SAE, 1996).

7 Quaresma, J., Santos, C. and Garcia, A. Correlation between unsteady-state solidification conditions, dendrite spacings, and mechanical properties of Al-Cu alloys. *Metallurgical and Materials Transactions A*, 2000, **31**(12), 3167-3178.

8 Aune, T.K., Gjestland, H., Haagensen, J.Ø., Kittilsen, B., Skar, J.I. and Westengen, H. *Magnesium Alloys*. (Wiley-VCH Verlag GmbH & Co. KGaA, 2000).

9 Yang, Z., Li, J., Zhang, J., Lorimer, G. and Robson, J. Review on research and development of magnesium alloys. *Acta Metallurgica Sinica (English Letters)*, 2008, **21**(5), 313-328.

10 Pekguleryuz, M.O. Development of creep resistant magnesium diecasting alloys. *Materials science forum*, pp. 131-140 (Trans Tech Publ, 2000).

11 Zhu, S.M., Nie, J.F., Gibson, M.A., Easton, M.A. and Bakke, P. Microstructure and Creep Behavior of High-Pressure Die-Cast Magnesium Alloy AE44. *Metallurgical and Materials Transactions A*, 2012, **43**(11), 4137-4144.

12 Han, Q., Kad ¡¶, B.K. and Viswanathan, S. Design perspectives for creep-resistant magnesium die-casting alloys. *Philosophical Magazine*, 2004, **84**(36), 3843-3860.

13 Chia, T.L., Easton, M.A., Zhu, S.M., Gibson, M.A., Birbilis, N. and Nie, J.F. The effect of alloy composition on the microstructure and tensile properties of binary Mg-rare earth alloys. *Intermetallics*, 2009, **17**(7), 481-490.

14 Li, N.Y. Magnesium advances and applications in North America automotive industry. p. 931 (Trans Tech Publ, 2005).

15 Friedrich, H.E. and Mordike, B.L. *Magnesium Technology*. (Springer, Germany

16 Mordike, B.L. and Ebert, T. Magnesium: Properties -- applications -- potential. *Materials Science and Engineering A*, 2001, **302**(1), 37-45.

17 Pollock, T.M. Weight Loss with Magnesium Alloys. *Science*, 2010, **328**(5981), 986-987.
18 Dahle, A.K., Lee, Y.C., Nave, M.D., Schaffer, P.L. and StJohn, D.H. Development of the as-cast microstructure in magnesium-aluminium alloys. *Journal of Light Metals*, 2001, **1**(1), 61-72.
19 Nave, M., Dahle, A. and StJohn, D. Eutectic growth morphologies in magnesium-aluminium alloys. pp. 233-2422000).
20 Jackson, K.A. Kinetic Processes. 2010.
21 Radhakrishna, K., Seshan, S. and Seshadri, M. Dendrite Arm Spacing and Mechanical Properties of Aluminum Alloy Castings. *Aluminum Metallurgy(Research, Developments and Technology)*, 1979, 123-129.
22 Campbell, J. *Castings*.
23 Lee, C. and Shin, K. Effects of precipitate and dendrite arm spacing on tensile properties and fracture behavior of As-Cast magnesium-aluminum alloys. *Metals and Materials International*, 2003, **9**(1), 21-27.
24 Osorio, W., Goulart, P., Garcia, A., Santos, G. and Neto, C. Effect of dendritic arm spacing on mechanical properties and corrosion resistance of Al 9 Wt Pct Si and Zn 27 Wt Pct Al alloys. *Metallurgical and Materials Transactions A*, 2006, **37**(8), 2525-2538.
25 Turhal, M.Ş. and Savaşkan, T. Relationships between secondary dendrite arm spacing and mechanical properties of Zn-40Al-Cu alloys. *Journal of Materials Science*, 2003, **38**(12), 2639-2646.
26 Seah, K.H.W., Hemanth, J. and Sharma, S.C. Effect of the cooling rate on the dendrite arm spacing and the ultimate tensile strength of cast iron. *Journal of Materials Science*, 1998, **33**(1), 23-28.
27 Cáceres, C.H., Poole, W.J., Bowles, A.L. and Davidson, C.J. Section thickness, macrohardness and yield strength in high-pressure diecast magnesium alloy AZ91. *Materials Science and Engineering: A*, 2005, **402**(1-2), 269-277.
28 Zhou, M., Li, N.Y. and Hu, H. Effect of section thicknesses on tensile behavior and microstructure of high pressure die cast magnesium alloy AM50. pp. 463-468 (Trans Tech Publ, 2005).
29 Aghion, E., Moscovitch, N. and Arnon, A. The correlation between wall thickness and properties of HPDC Magnesium alloys. *Materials Science and Engineering: A*, 2007, **447**(1-2), 341-346.
30 Xie, F.Y., Kraft, T., Zuo, Y., Moon, C.H. and Chang, Y. Microstructure and microsegregation in Al-rich Al-Cu-Mg alloys. *Acta Materialia*, 1999, **47**(2), 489-500.
31 Lathabai, S. and Lloyd, P. The effect of scandium on the microstructure, mechanical properties and weldability of a cast Al-Mg alloy. *Acta Materialia*, 2002, **50**(17), 4275-4292.
32 Ganesan, M., Dye, D. and Lee, P. A technique for characterizing microsegregation in multicomponent alloys and its application to single-crystal superalloy castings. *Metallurgical and Materials Transactions A*, 2005, **36**(8), 2191-2204.
33 Yang, W., Chang, K.-M., Chen, W., Mannan, S. and DeBarbadillo, J. Monte carlo sampling for microsegregation measurements in cast structures. *Metallurgical and Materials Transactions A*, 2000, **31**(10), 2569-2574.

34 Gungor, M. A statistically significant experimental technique for investigating microsegregation in cast alloys. *Metallurgical and Materials Transactions A*, 1989, **20**(11), 2529-2533.
35 Sarreal, J. and Abbaschian, G. The effect of solidification rate on microsegregation. *Metallurgical and Materials Transactions A*, 1986, **17**(11), 2063-2073.
36 Flemings, M.C., Poirier, D.R., Barone, R.V. and Brody, H.D. *J. Iron Steel Inst.* ***208***
1970, 371.
37 Lacaze, J., Benigni, P. and Howe, A. Some Issues Concerning Experiments and Models for Alloy Microsegregation. *Advanced Engineering Materials*, 2003, **5**(1-2), 37-46.
38 Xie, F., Yan, X., Ding, L., Zhang, F., Chen, S., Chu, M.G. and Chang, Y.A. A study of microstructure and microsegregation of aluminum 7050 alloy. *Materials Science and Engineering A*, 2003, **355**(1-2), 144-153.
39 Martorano, M. and Capocchi, J. Effects of processing variables on the microsegregation of directionally cast samples. *Metallurgical and Materials Transactions A*, 2000, **31**(12), 3137-3148.
40 Sasikumar, R., Kraft, T. and Exner, H. Influence of the shape of the cooling curves on microsegregation. *Scripta Metallurgica et Materialia(USA)*, 1993, **28**(2), 235-240.
41 Zheng, X., Luo, A., Zhang, C., Dong, J. and Waldo, R. Directional Solidification and Microsegregation in a Magnesium-Aluminum-Calcium Alloy. *Metallurgical and Materials Transactions A*, 2012, **43**(9), 3239-3248.
42 Mirković, D. and Schmid-Fetzer, R. Directional Solidification of Mg-Al Alloys and Microsegregation Study of Mg Alloys AZ31 and AM50: Part I. Methodology. *Metallurgical and Materials Transactions A*, 2009, **40**(4), 958-973.
43 Mirković, D. and Schmid-Fetzer, R. Directional Solidification of Mg-Al Alloys and Microsegregation Study of Mg Alloys AZ31 and AM50: Part II. Comparison between AZ31 and AM50. *Metallurgical and Materials Transactions A*, 2009, **40**(4), 974-981.
44 Zhang, C., Ma, D., Wu, K.S., Cao, H.B., Cao, G.P., Kou, S., Chang, Y.A. and Yan, X.Y. Microstructure and microsegregation in directionally solidified Mg-4Al alloy. *Intermetallics*, 2007, **15**(10), 1395-1400.
45 Wei, L.-Y. and Warren, R. Microstructural characterisation of several magnesium alloys in AM series. *Materials Science and Technology*, 2007, **23**, 745-752.
46 Barbagallo, S., Laukli, H., Lohne, O. and Cerri, E. Divorced eutectic in a HPDC magnesium-aluminum alloy. *Journal of Alloys and Compounds*, 2004, **378**(1-2), 226-232.
47 Han, Q., Kenik, E., Agnew, S. and Viswanathan, S. Solidification behaviour of commercial magnesium alloys; Magnesium Technology 2001, 11.-15.02. 2001, New Orleans, The Minerals. *Metals & Materials Society, Warrendale, S*, 2001, 81-86.
48 Zhang, Z., Couture, A., Tremblay, R. and Dube, D. Microstructure and mechanical properties of permanent mold and die casting of AZ 91 magnesium alloy. pp. 397-4061999).
49 Ditze, A. and Schwerdtfeger, K. Strip casting of magnesium with the single belt process. *Scandinavian journal of metallurgy*, 2003, **32**(6), 311-316.

50 **Guo, S., Le, Q., Han, Y., Zhao, Z. and Cui, J.** The effect of the electromagnetic vabration on the microstructure, segregation, and mechanical properties of As-cast AZ80 magnesium alloy billet. *Metallurgical and Materials Transactions A*, 2006, **37**(12), 3715-3724.
51 **Kleiner, S., Beffort, O., Wahlen, A. and Uggowitzer, P.** Microstructure and mechanical properties of squeeze cast and semi-solid cast Mg-Al alloys. *Journal of Light Metals*, 2002, **2**(4), 277-280.
52 **Song, G. and Atrens, A.** Understanding Magnesium Corrosion—A Framework for Improved Alloy Performance. *Advanced Engineering Materials*, 2003, **5**(12), 837-858.
53 **Song, G.** Recent Progress in Corrosion and Protection of Magnesium Alloys. *Advanced Engineering Materials*, 2005, **7**(7), 563-586.
54 **Zhao, M.-C., Liu, M., Song, G. and Atrens, A.** Influence of the [beta]-phase morphology on the corrosion of the Mg alloy AZ91. *Corrosion Science*, 2008, **50**(7), 1939-1953.
55 **Poirier, D.R.** (MIT, Cambridge, MA, 1966).
56 **Brody, H.D.** Microsegregation. *ASM Handbook: Casting*, pp. 338-3472008).
57 **Xie, F.** Solidification modeling and experimental investigation of Al- rich Al-Cu-Mg-Zn alloys. *Metallurgical Engineering*, p. 179 (University of Wisconsin-Madison, 1999).
58 **Scheil, E.** Bemerkungen zur schichtkristallbildung. *Zeitschrift f ¼r Metallkunde*, 1942, **34**(3), 70-72.
59 **Clyne, T. and Kurz, W.** Solute redistribution during solidification with rapid solid state diffusion. *Metallurgical and Materials Transactions A*, 1981, **12**(6), 965-971.
60 **Bower, T., Brody, H. and Flemings, M.** Measurements of solute redistribution in dendritic solidification. *Transaction of the Metallurgical Society of AIME*, 1966, **236**, 624-633.
61 **Ohnaka, I.** Mathematical analysis of solute redistribution during solidification with diffusion in solid phase. *Transactions of the Iron and Steel Institute of Japan*, 1986, **26**(12), 1045-1051.
62 **Kobayashi, S.** A Mathematical Model for Solute Redistribution during Dendritic Solidification. *Trans. Iron Steel Inst. Jpn.*, 1988, **28**(7), 535-542.
63 **Nastac, L. and Stefanescu, D.M.** An analytical model for solute redistribution during solidification of planar, columnar, or equiaxed morphology. *Metallurgical Transactions A*, 1993, **24**(9), 2107-2118.
64 **Kraft, T., Rettenmayr, M. and Exner, H.** An extended numerical procedure for predicting microstructure and microsegregation of multicomponent alloys. *Modelling and Simulation in Materials Science and Engineering*, 1999, **4**(2), 161.
65 **Xie, F.Y., Kraft, T., Zuo, Y., Moon, C.H. and Chang, Y.A.** Microstructure and microsegregation in Al-rich Al-Cu-Mg alloys. *Acta Materialia*, 1999, **47**(2), 489-500.
66 **Du, Q. and Jacot, A.** A two-dimensional microsegregation model for the description of microstructure formation during solidification in multicomponent alloys: Formulation and behaviour of the model. *Acta Materialia*, 2005, **53**(12), 3479-3493.
67 **Boettinger, W.J., Kattner, U.R. and Banerjee, D.K.** Analysis of solidification path and microsegregation in multicomponent alloys. *Thomas BG, Beckermann C.*

Modelling of Casting, Welding and Advanced Solidification Processed-VIII (1), pp. 159-170 (Warrendale, PA: TMS, 1998).
68 Flemings, M.C. *Solidification Processing*. (McGraw-Hill, 1974).
69 Flemings, M.C. Solidification processing. *Metallurgical and Materials Transactions B*, 1974, **5**(10), 2121-2134.
70 Kearsey, R.M. Compositional effects on microsegregation behaviour in single crystal superalloy systems. *Mechanical and aerospace engineering*, p. 362 (Carleton University, Ottawa, Ontario, 2004).
71 Huang, Y., Dieringa, H., Hort, N., Maier, P., Kainer, K. and Liu, Y.-L. Evolution of microstructure and hardness of AE42 alloy after heat treatments. *Journal of Alloys and Compounds*, 2008, **463**(1), 238-245.
72 Patel, H., Chen, D., Bhole, S. and Sadayappan, K. Microstructure and tensile properties of thixomolded magnesium alloys. *Journal of Alloys and Compounds*, 2010, **496**(1), 140-148.
73 Cáceres, C.H., Griffiths, J.R., Pakdel, A.R. and Davidson, C.J. Microhardness mapping and the hardness-yield strength relationship in high-pressure diecast magnesium alloy AZ91. *Materials Science and Engineering: A*, 2005, **402**(1-2), 258-268.
74 Weiler, J., Wood, J., Klassen, R., Berkmortel, R. and Wang, G. Variability of skin thickness in an AM60B magnesium alloy die-casting. *Materials Science and Engineering: A*, 2006, **419**(1), 297-305.
75 Wang, X.S. and Fan, J.H. SEM online investigation of fatigue crack initiation and propagation in cast magnesium alloy. *Journal of Materials Science*, 2004, **39**(7), 2617-2620.
76 H. Putz, a.K.B. Pearson's Crystal Data, Crystal Structure Database for Inorganic Compounds, CD-ROM software version 1.3. .
77 Rzychon, T., Kielbus, A., Cwajna, J. and Mizera, J. Microstructural stability and creep properties of die casting Mg-4Al-4RE magnesium alloy. *Materials Characterization*, 2009, **60**(10), 1107-1113.
78 Zhang, J., Leng, Z., Liu, S., Zhang, M., Meng, J. and Wu, R. Structure stability and mechanical properties of Mgâ€“Al-based alloy modified with Y-rich and Ce-rich misch metals. *Journal of Alloys and Compounds*, 2011
509(20), L187-L193.
79 Zhang, J., Yu, P., Liu, K., Fang, D., Tang, D. and Meng, J. Effect of substituting cerium-rich mischmetal with lanthanum on microstructure and mechanical properties of die-cast Mg-Al-RE alloys. *Materials & Design*, 2009, **30**(7), 2372-2378.
80 Zhang, J., Leng, Z., Zhang, M., Meng, J. and Wu, R. Effect of Ce on microstructure, mechanical properties and corrosion behavior of high-pressure die-cast Mgâ€“4Al-based alloy. *Journal of Alloys and Compounds*, 2011, **509**(3), 1069-1078.
81 Zhang, J., Zhang, M., Meng, J., Wu, R. and Tang, D. Microstructures and mechanical properties of heat-resistant high-pressure die-cast Mg-4Al-XLa-0.3Mn (x=1, 2, 4, 6) alloys. *Materials Science and Engineering: A*, 2010, **527**(10-11), 2527-2537.
82 Kiebus, A. Microstructure of AE44 magnesium alloy before and after hot chamber die casting. *Journal of Achievements in Materials and Manufacturing Engineering*, 2007, **20**, 459-462.

83 Rzychon, T. and Kiebus, A. Effect of rare earth elements on the microstructure of Mg-Al alloys. *Journal of Achievements in Materials and Manufacturing Engineering*, 2006, **18**, 135-138.
84 Rzychon T., Kiebus, A. and Dercz, G. Structural and quantitative analysis of die cast AE44 magnesium alloy. *Journal of Achievements in Materials and Manufacturing Engineering*, 2007, **22**(2), 43-46.
85 Zhang, J., Zhang, D., Tian, Z., Wang, J., Liu, K., Lu, H., Tang, D. and Meng, J. Microstructures, tensile properties and corrosion behavior of die-cast Mg-4Al-based alloys containing La and/or Ce. *Materials Science and Engineering: A*, 2008, **489**, 113-119.
86 Rzychon, T. and Kiebus, A. The influence of wall thickness on the microstructure of HPDC AE44 alloy. *Archives of Materials Science*, 2007, **472**, 472.
87 Shang, S., Zhang, H., Ganeshan, S. and Liu, Z.-K. The development and application of a thermodynamic database for magnesium alloys. *JOM*, 2008, **60**(12), 45-47.
88 TerBush, J., Saddock, N., Jones, J. and Pollock, T. Partitioning of Solute to the Primary <i>α</i>-Mg Phase in Creep-Resistant Mg-Al-Ca–Based Cast Alloys. *Metallurgical and Materials Transactions A*, **41**(9), 2435-2442.
89 Hehmann, F., Sommer, F. and Predel, B. Extension of solid solubility in magnesium by rapid solidification. *Materials Science and Engineering: A*, 1990, **125**(2), 249-265.
90 Lacaze, J. and Lesoult, G.R.J. Experimental investigation of the development of microsegregation during solidification of an Al---Cu---Mg---Si aluminium alloy. *Materials Science and Engineering: A*, 1993, **173**(1-2), 119-122.
91 Kuisma-Kursula, P. Accuracy, precision and detection limits of SEM–WDS, SEM–EDS and PIXE in the multi-elemental analysis of medieval glass. *X-Ray Spectrometry*, 2000, **29**(1), 111-118.
92 Zhao, Y.-Z., Zhao, Y.-H., Li, Q., Chen, S.-L., Zhang, J.-Y. and Chou, K.-C. Effects of step size and cut-off limit of residual liquid amount on solidification simulation of Al-Mg-Zn system with Scheil model. *Intermetallics*, 2009, **17**(7), 491-495.
93 T. Rzychon, A.K.b. The influence of wall thickness on the microstructure of HPDC AE44 alloy. *Archives of Materials Science and Engineering*, 2007, **Volume 28**(Issue 8), 471-474.

Appendix

A.1 Microstructural mapping of AZ91D alloy

AZ91D location 1

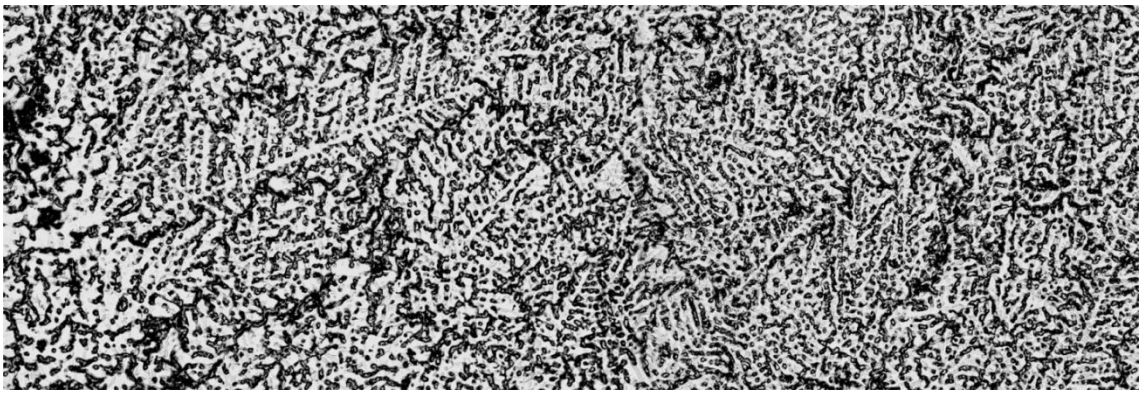

Figure 5-1: Edge of the wedge

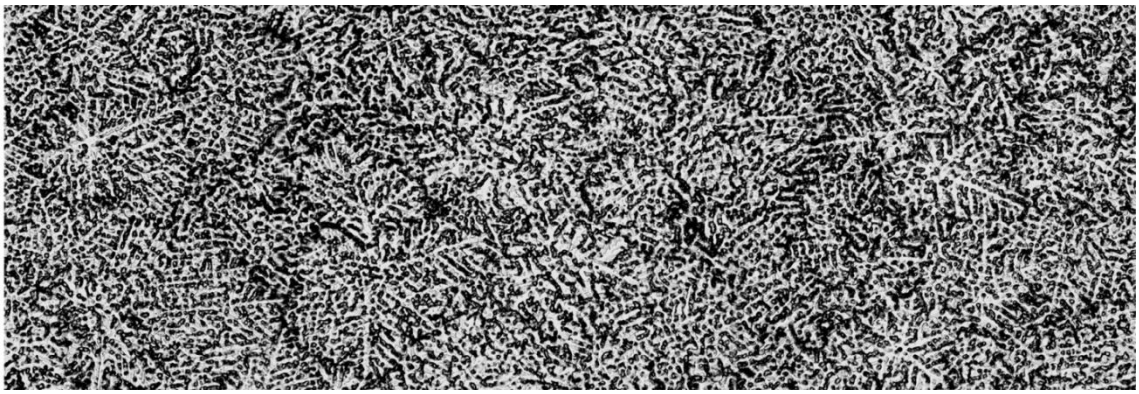

Figure 5-2: Columnar to equiaxed transition

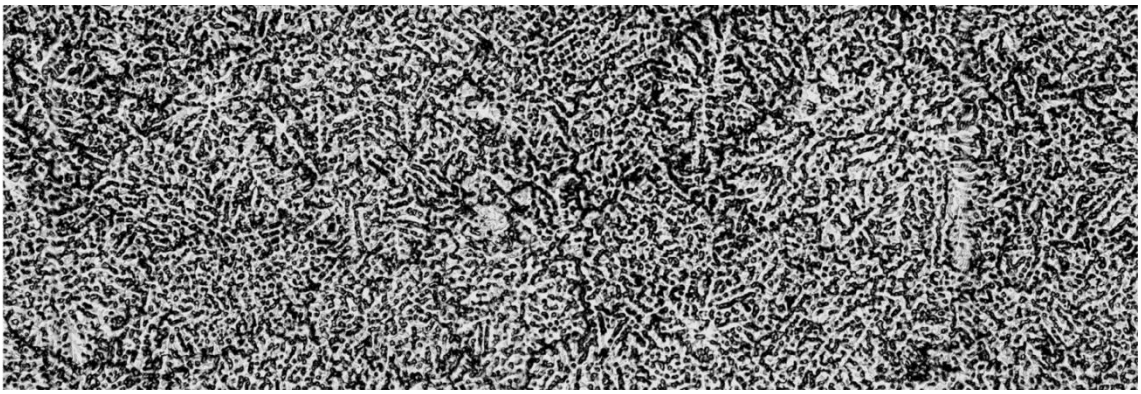

Figure 5-3: Center of the wedge

AZ91D location 2

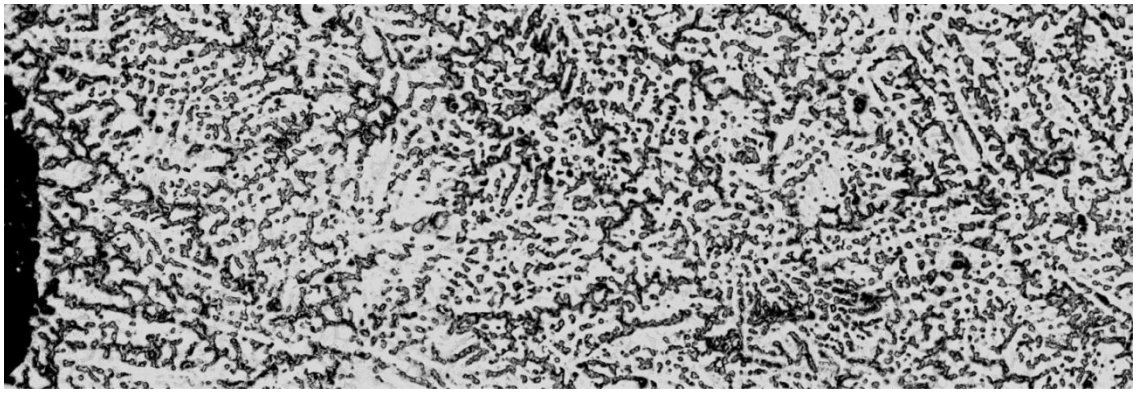

Figure 5-4: Edge of the wedge

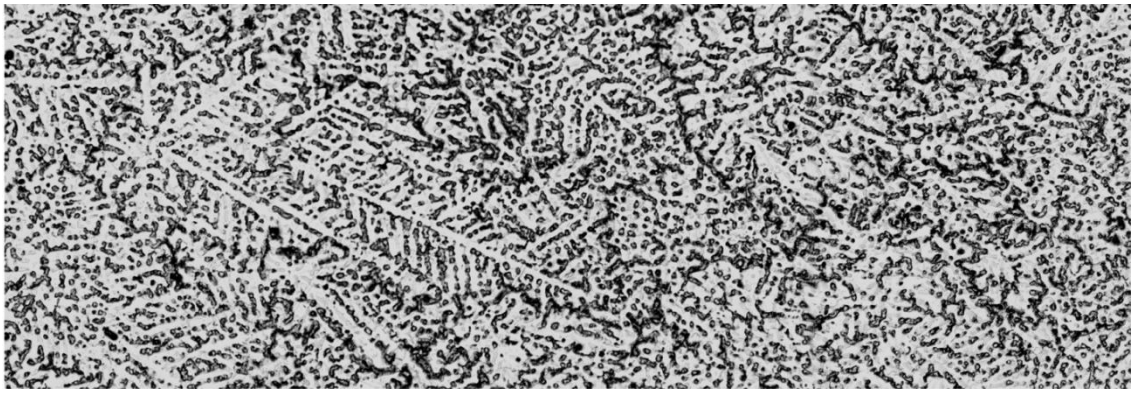

Figure 5-5: Columnar to equiaxed transition

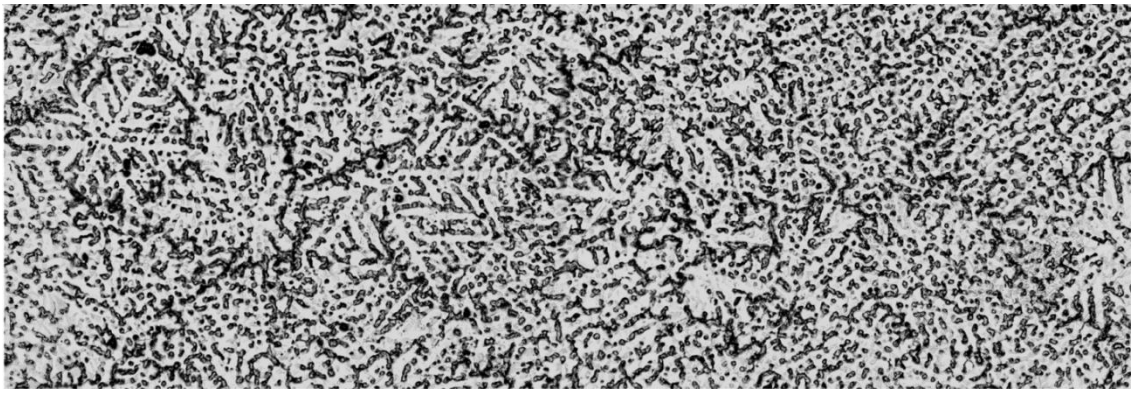

Figure 5-6: Center of the wedge

AZ91D location 3

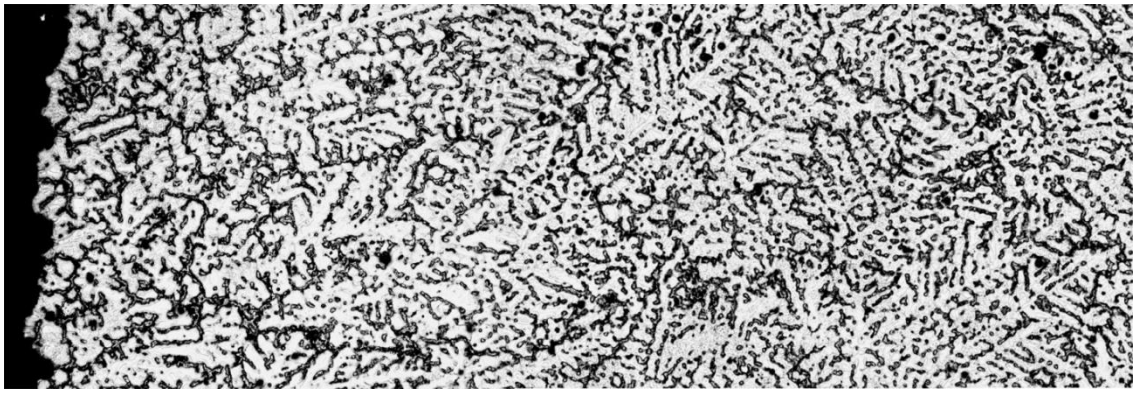

Figure 5-7: Edge of the wedge

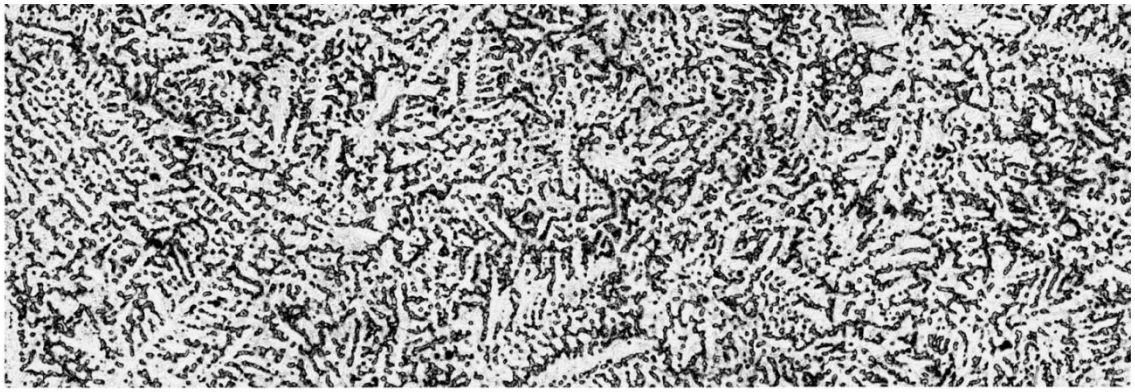

Figure 5-8: Columnar to equiaxed transition

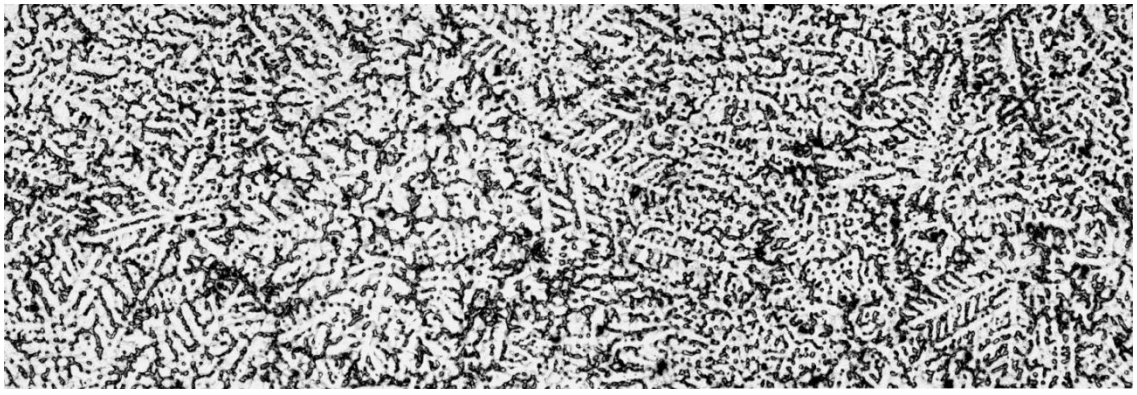

Figure 5-9: Center of the wedge

AZ91D location 4

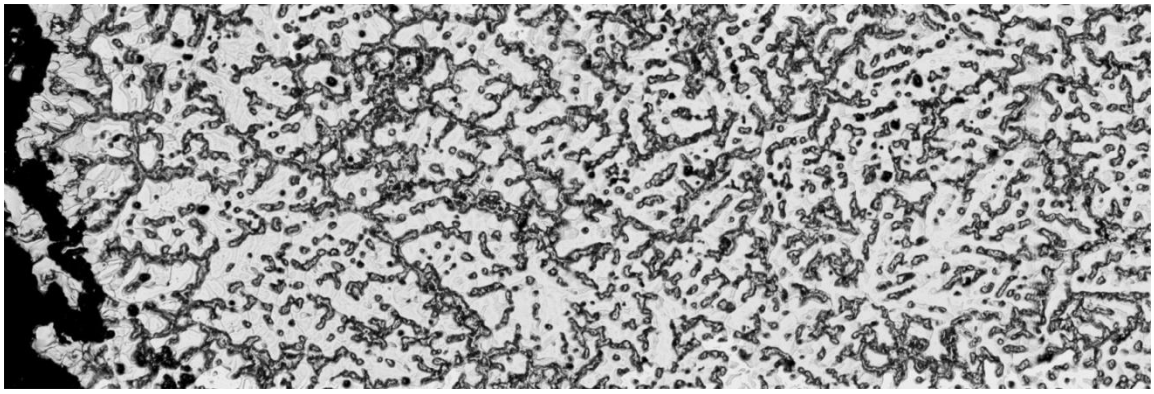

Figure 5-10: Edge of the wedge

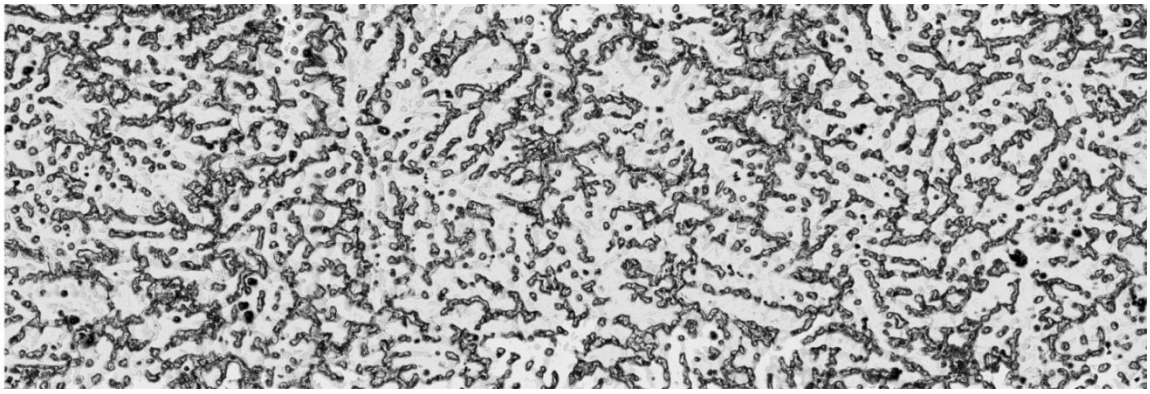

Figure 5-11: Columnar to equiaxed transition

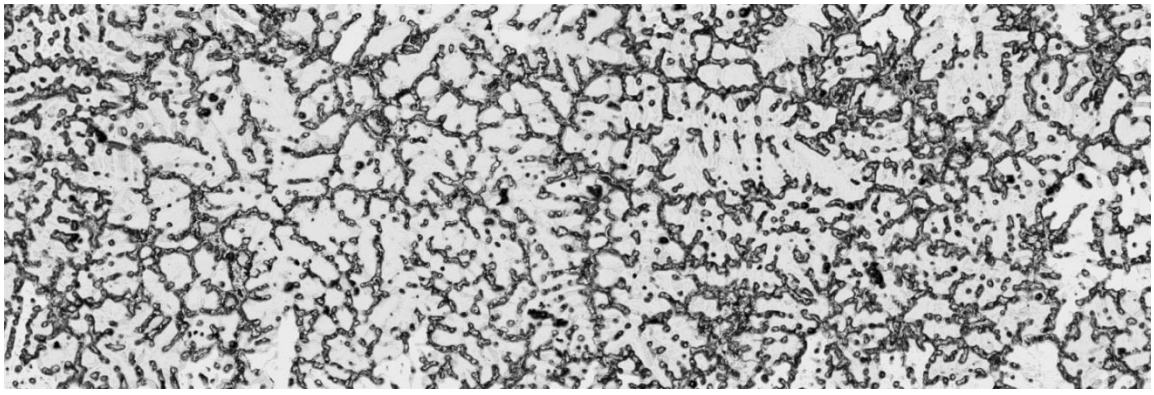

Figure 5-12: Center of the wedge

AZ91D location 5

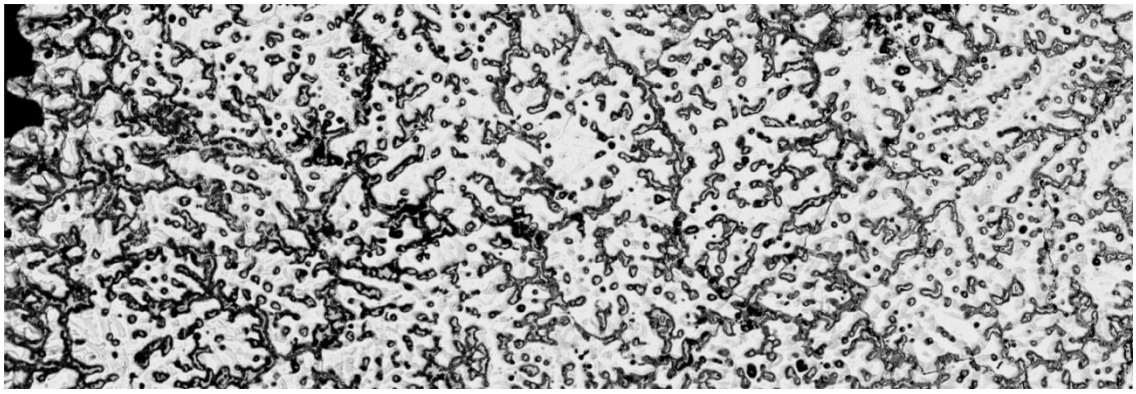

Figure 5-13: Edge of the wedge

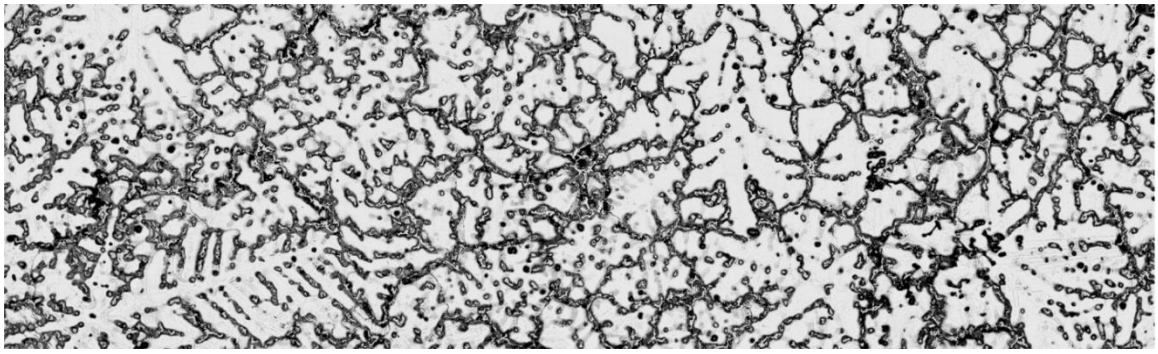

Figure 5-14: Columnar to equiaxed transition

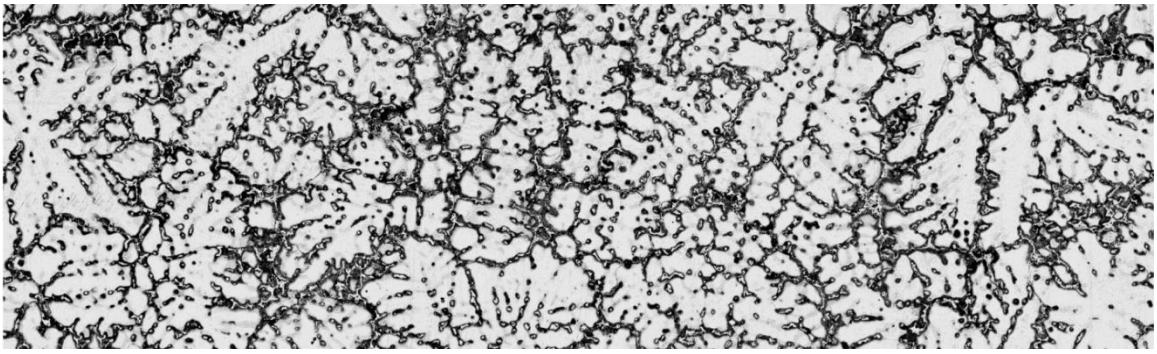

Figure 5-15: Center of the wedge

AZ91D location 6

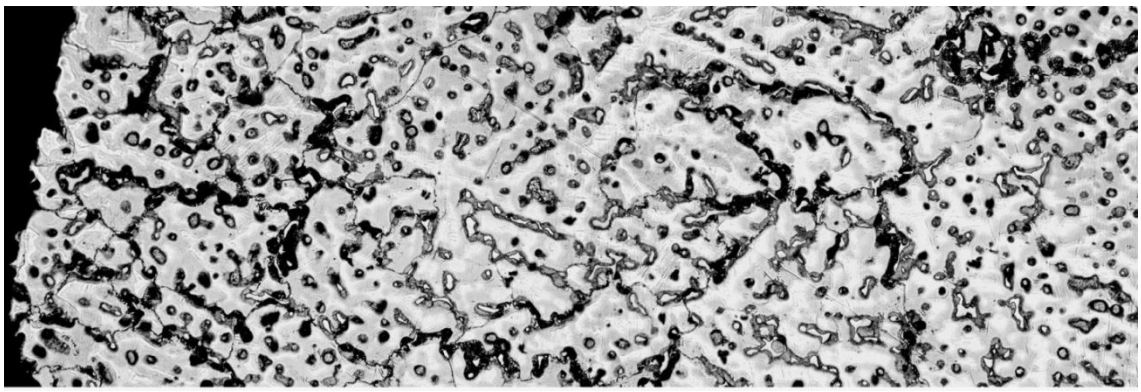

Figure 5-16: Edge of the wedge

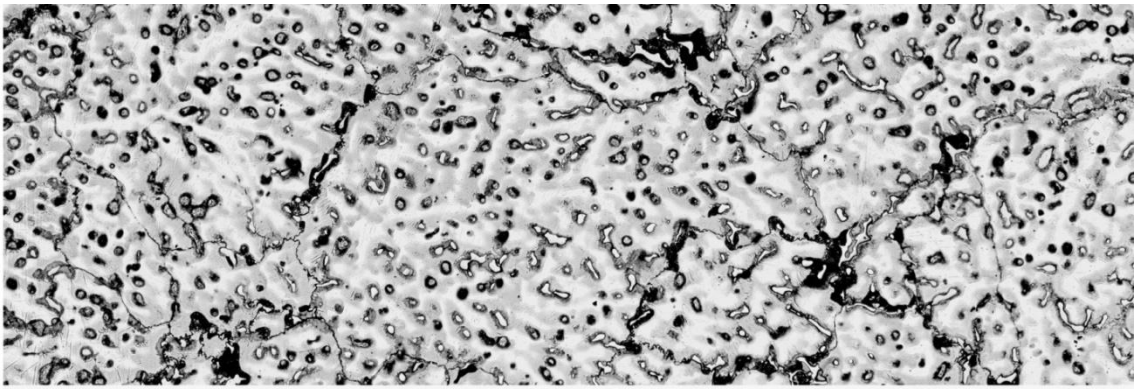

Figure 5-17: Columnar to equiaxed transition

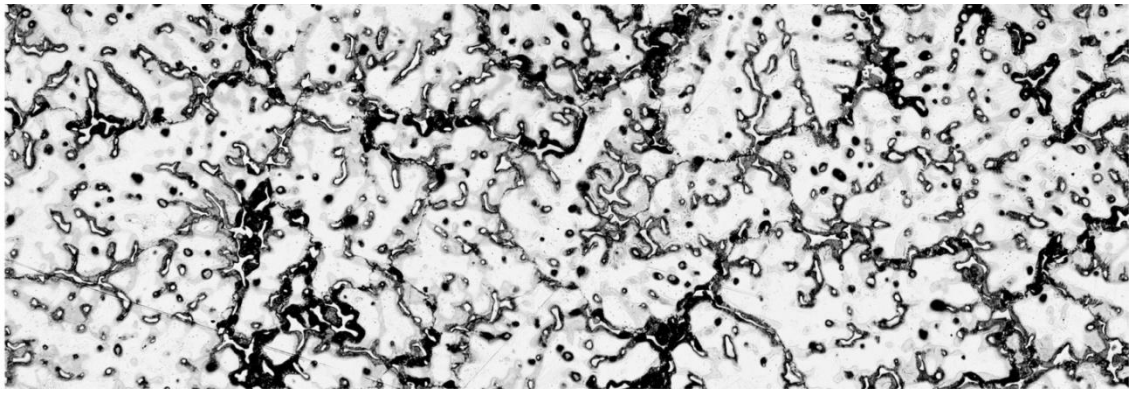

Figure 5-18: Center of the wedge

A.2 Microstructural mapping of AM60B alloy

AM60B location 1

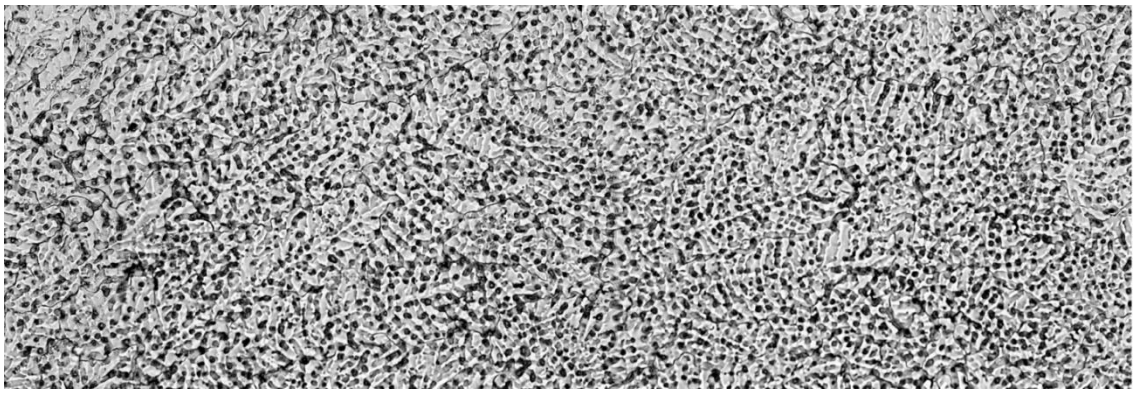

Figure 5-19: Edge of the wedge

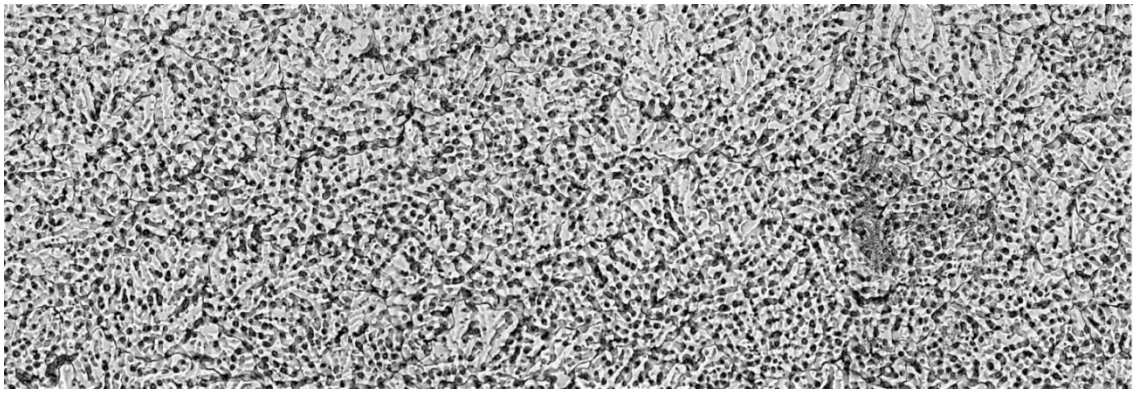

Figure 5-20: Columnar to equiaxed transition

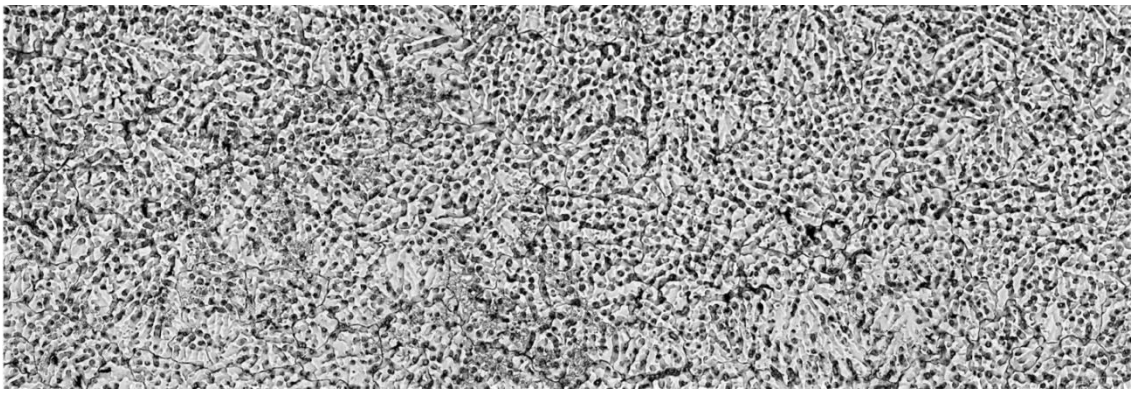

Figure 5-21: Center of the wedge

AM60B location 2

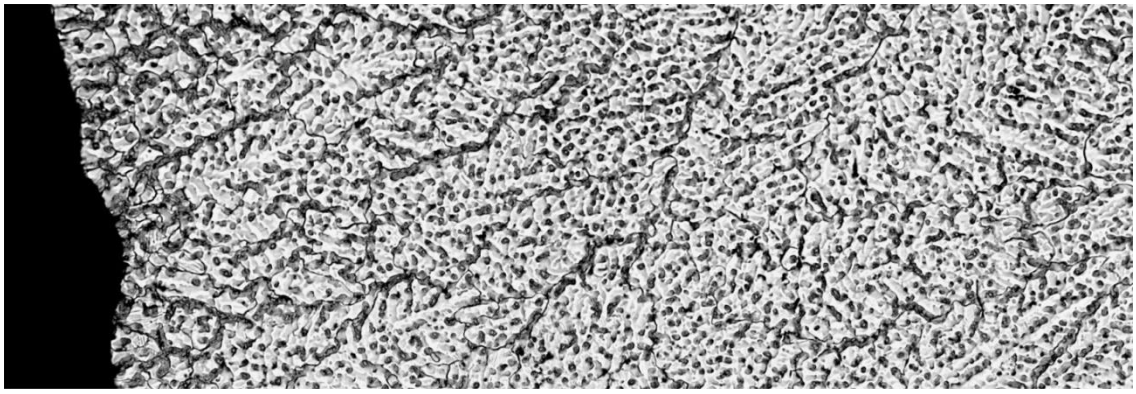

Figure 5-22: Edge of the wedge

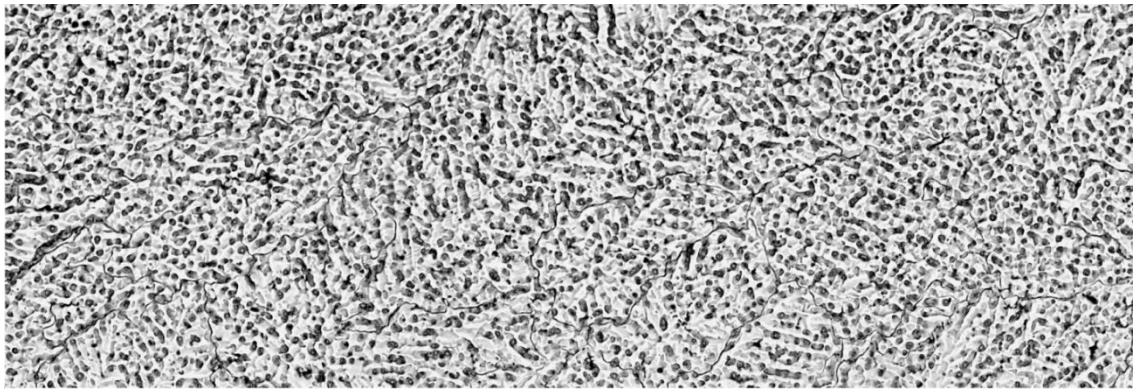

Figure 5-23: Columnar to equiaxed transition

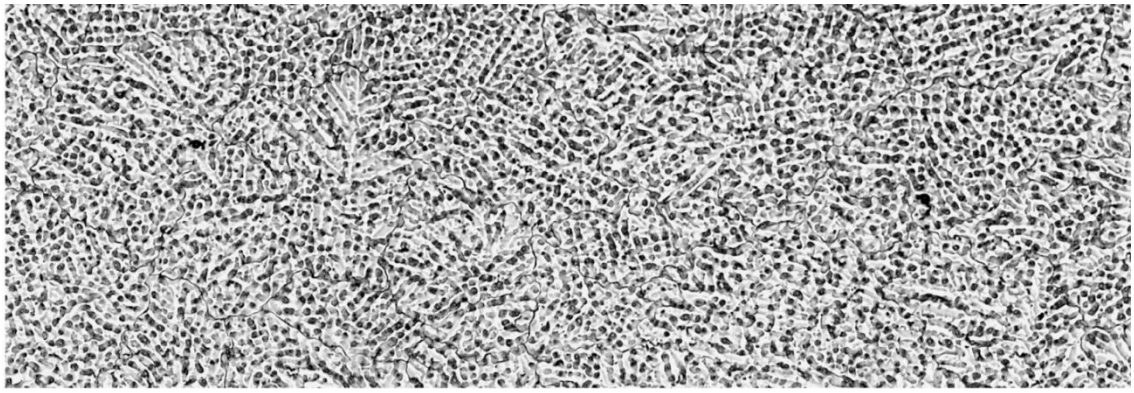

Figure 5-24: Center of the wedge

AM60B location 3

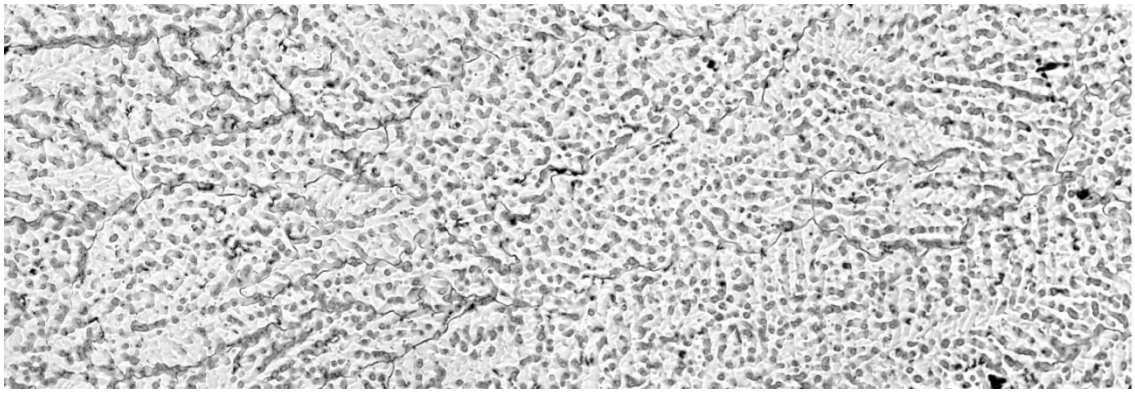

Figure 5-25: Edge of the wedge

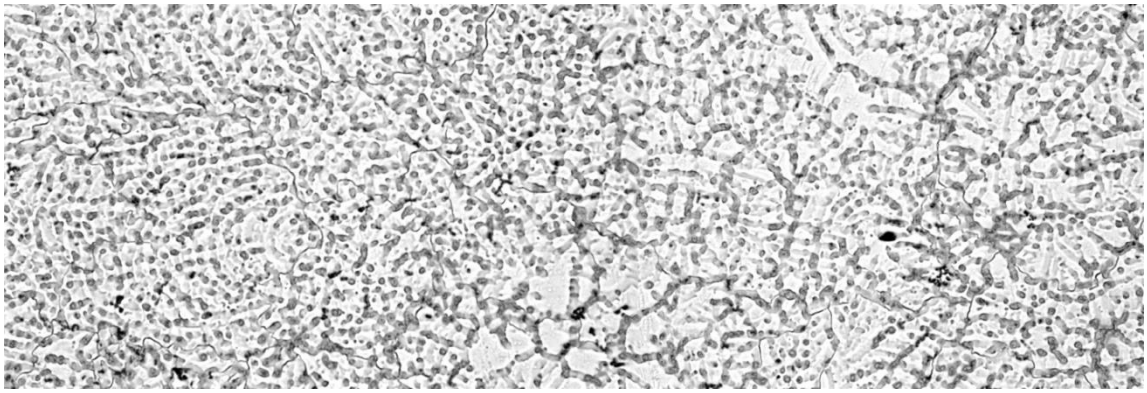

Figure 5-26: Columnar to equiaxed transition

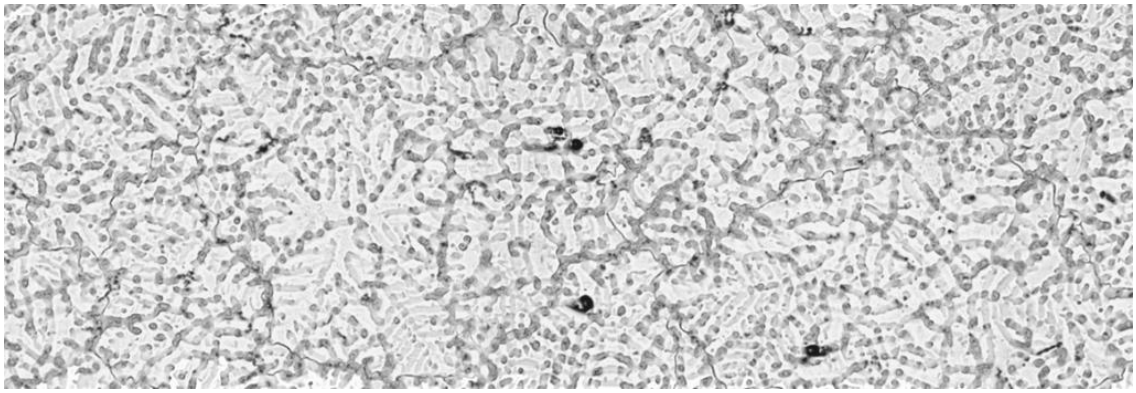

Figure 5-27: Center of the wedge

AM60B location 4

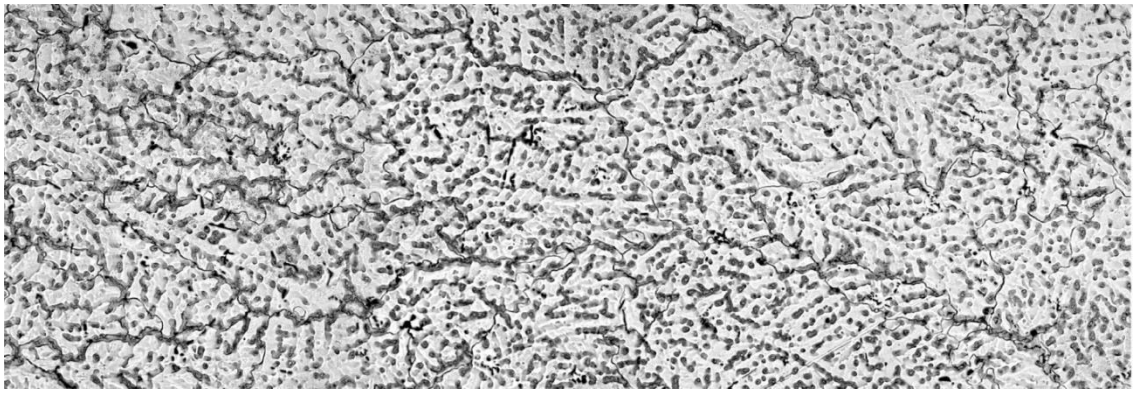

Figure 5-28: Edge of the wedge

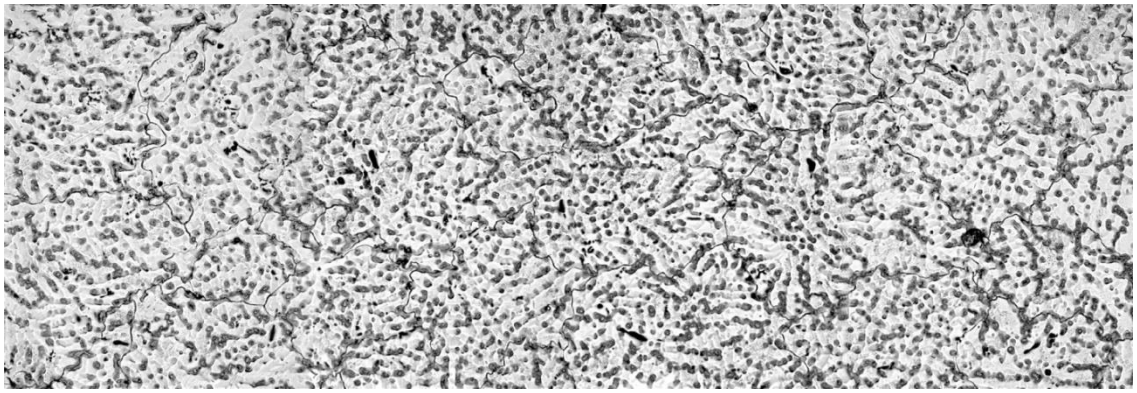

Figure 5-29: Columnar to equiaxed transition

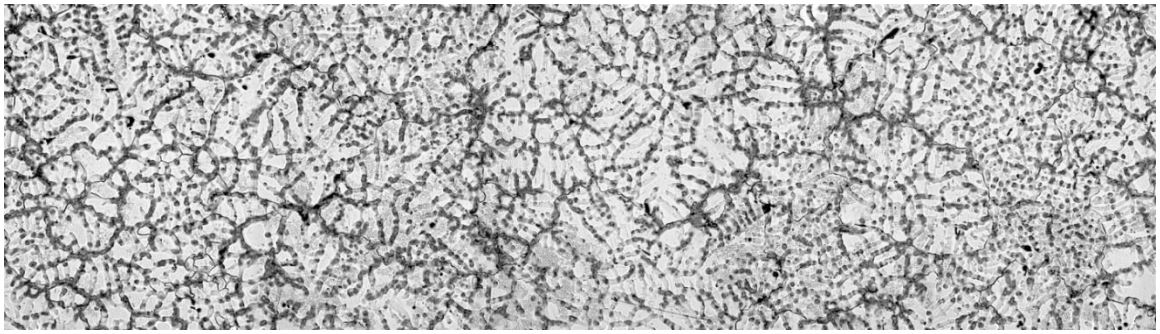

Figure 5-30: Center of the wedge

AM60B location 5

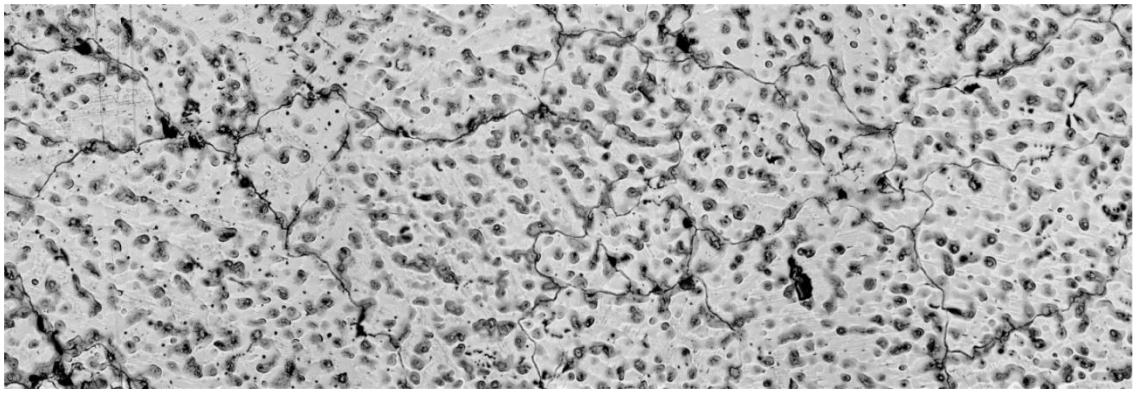

Figure 5-31: Edge of the wedge

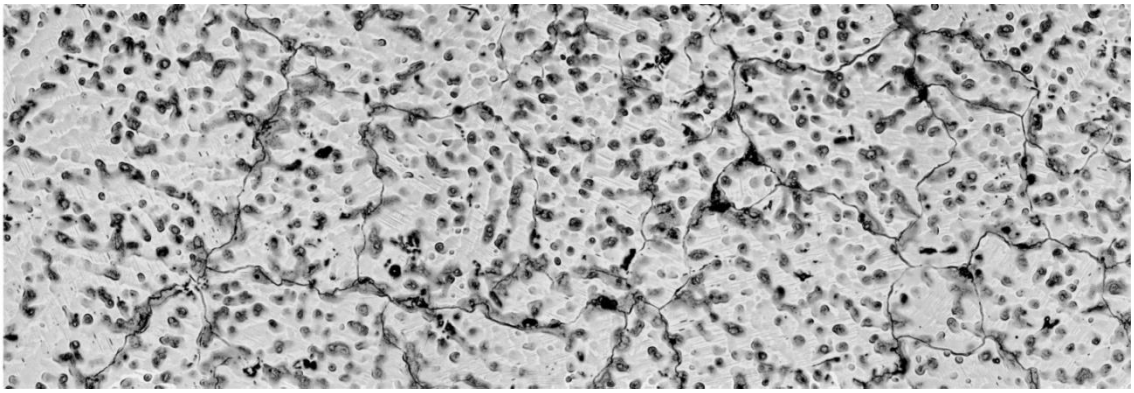

Figure 5-32: Columnar to equiaxed transition

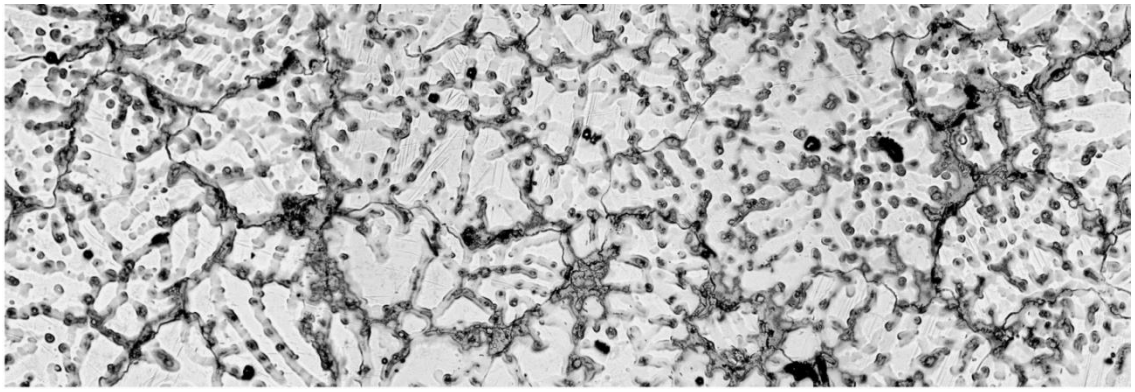

Figure 5-33: Center of the wedge

AM60B location 6

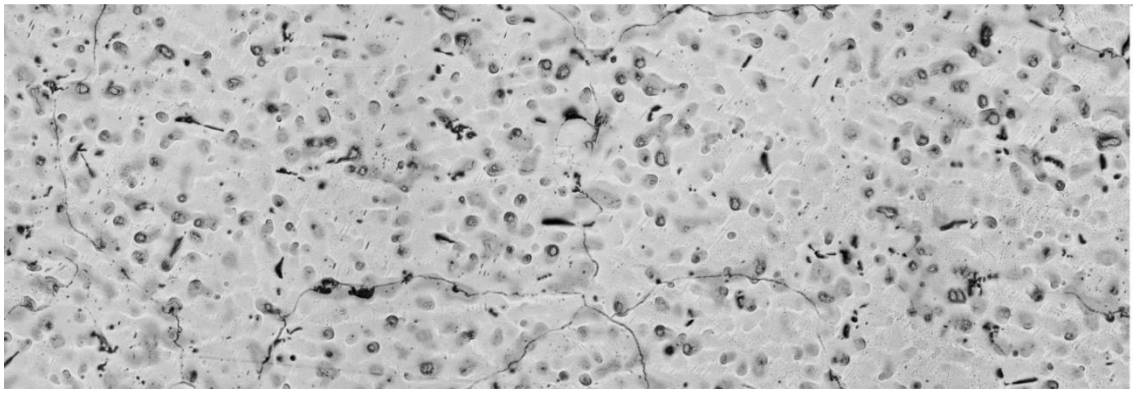

Figure 5-34: Edge of the wedge

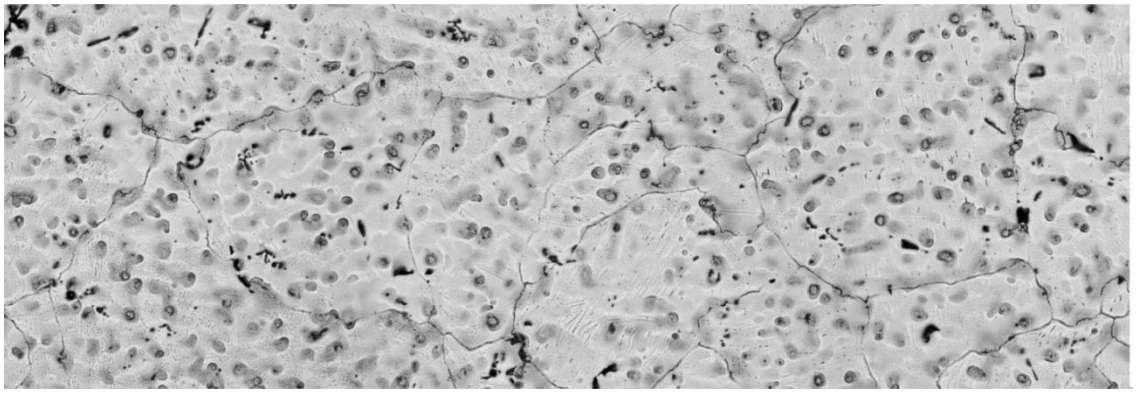

Figure 5-35: Columnar to equiaxed transition

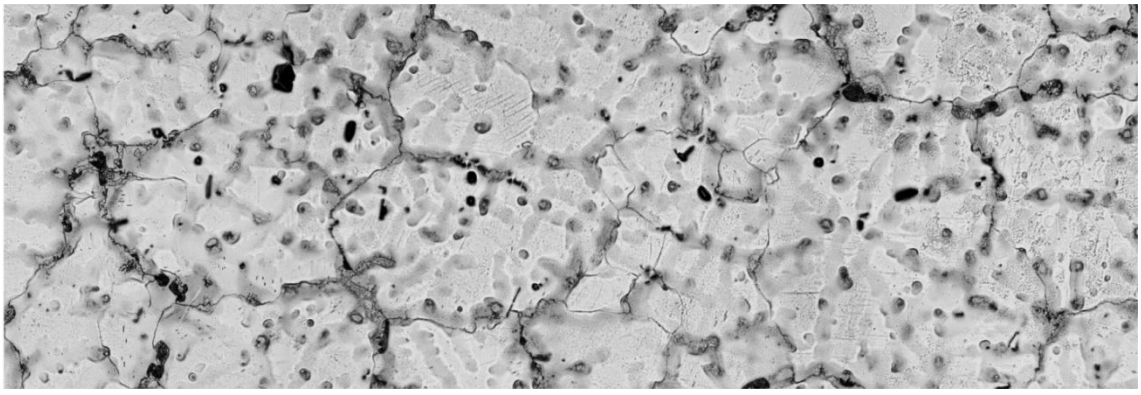

Figure 5-36: Center of the wedge

A.3 Microstructural mapping of AE44 alloy

AE44 location 1

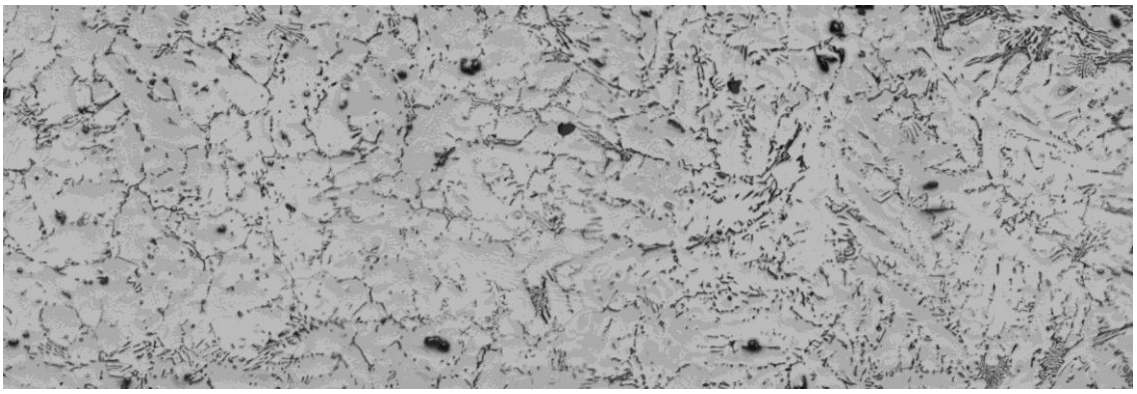

Figure 5-37: Edge of the wedge

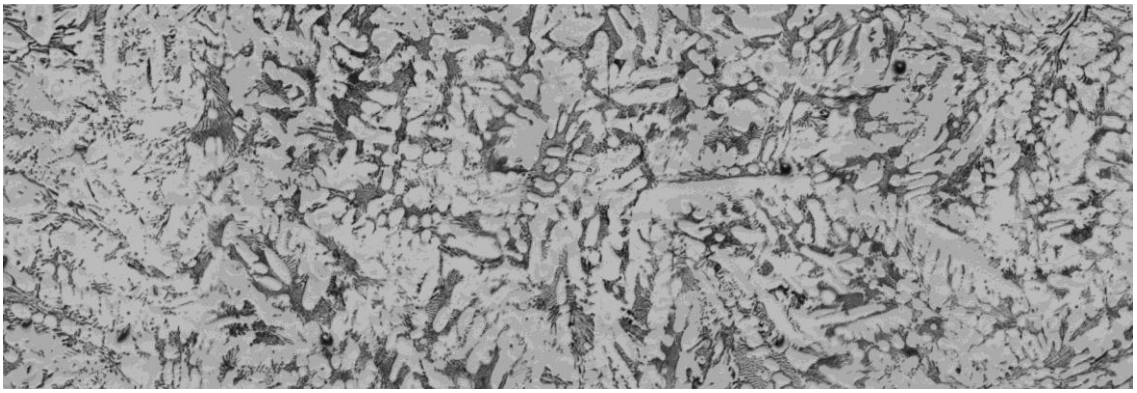

Figure 5-38: Columnar to equiaxed transition

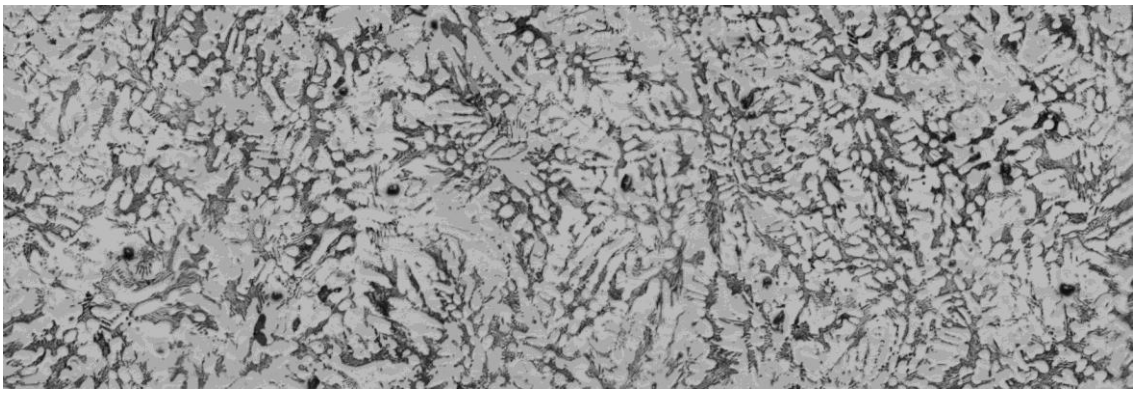

Figure 5-39: Center of the wedge

AE44 location 2

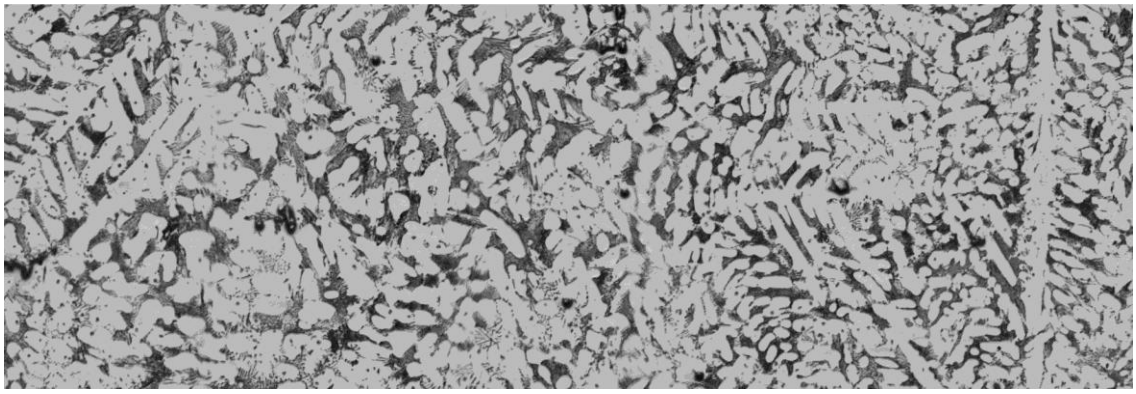

Figure 5-40: Edge of the wedge

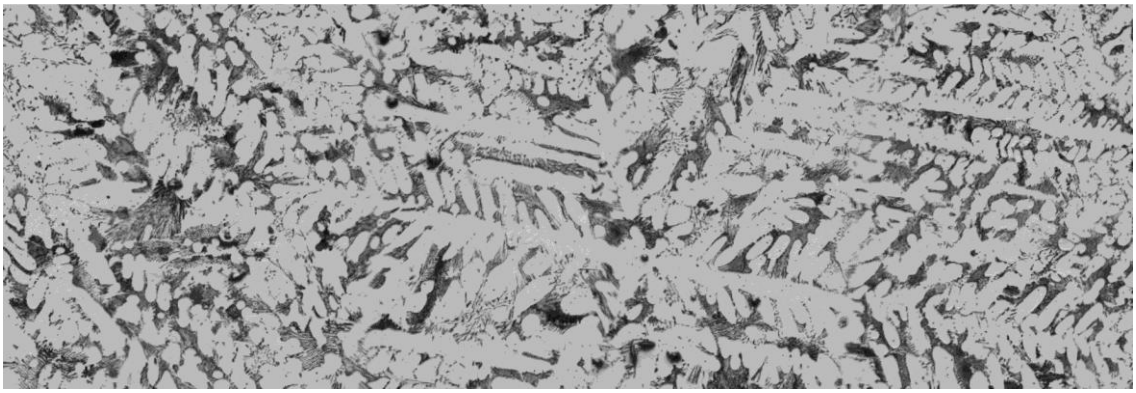

Figure 5-41: Columnar to equiaxed transition

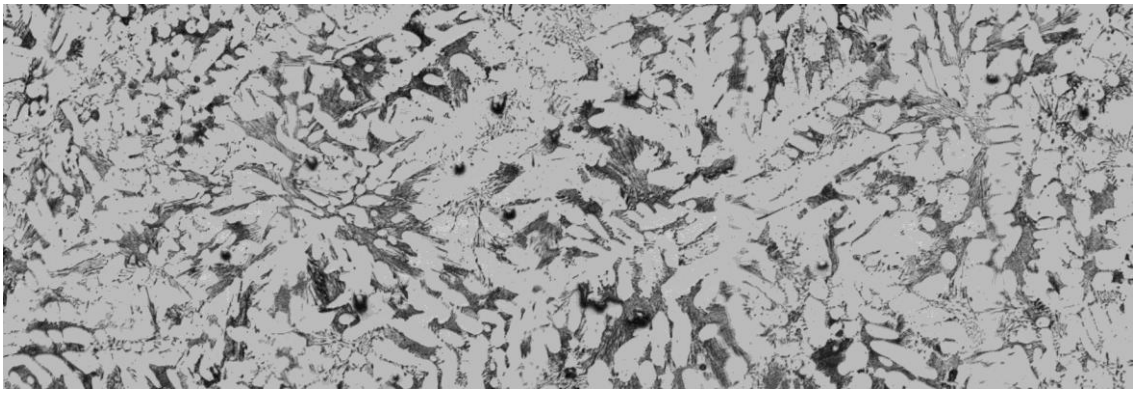

Figure 5-42: Center of the wedge

AE44 location 3

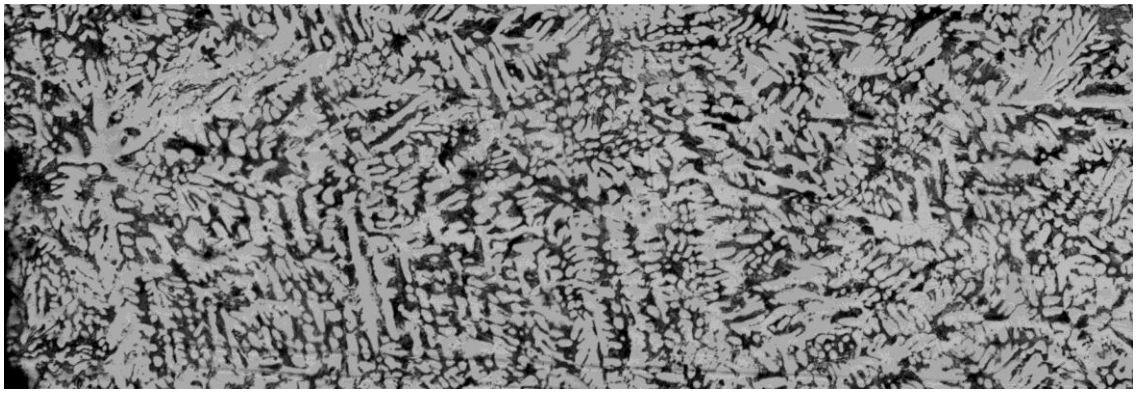

Figure 5-43: Edge of the wedge

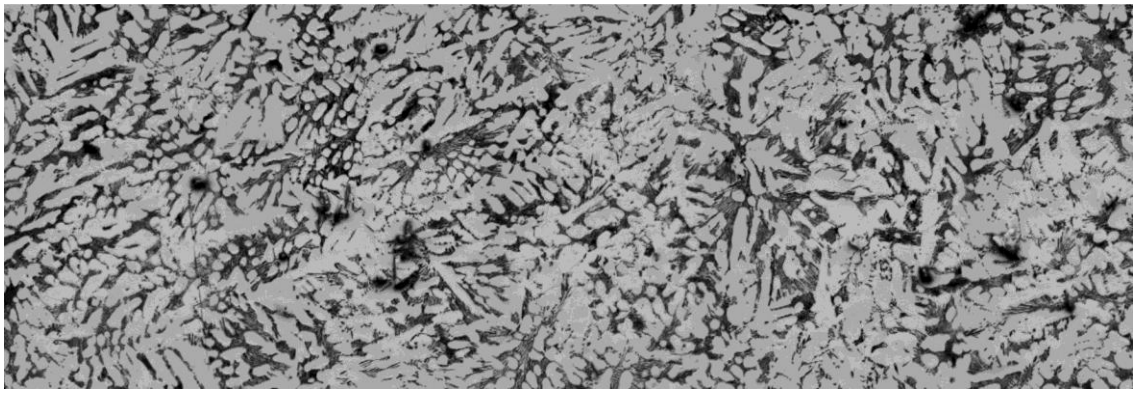

Figure 5-44: Columnar to equiaxed transition

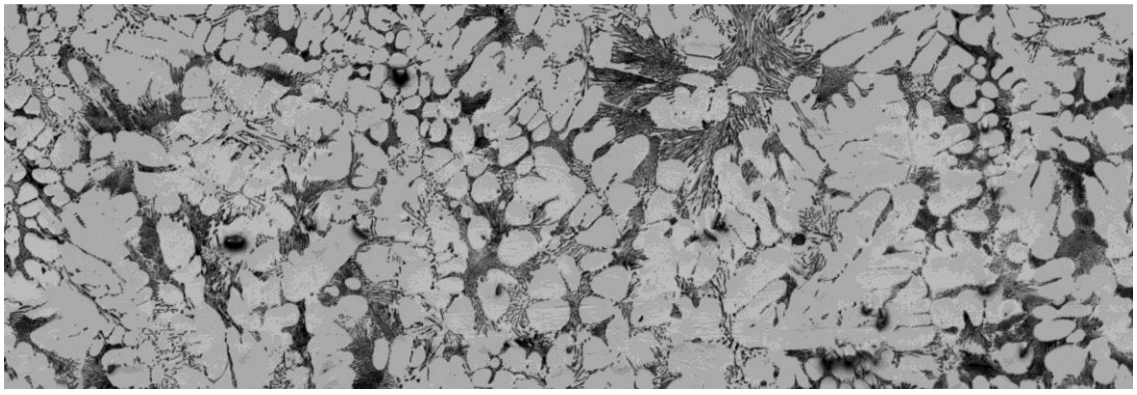

Figure 5-45: Center of the wedge

AE44 location 4

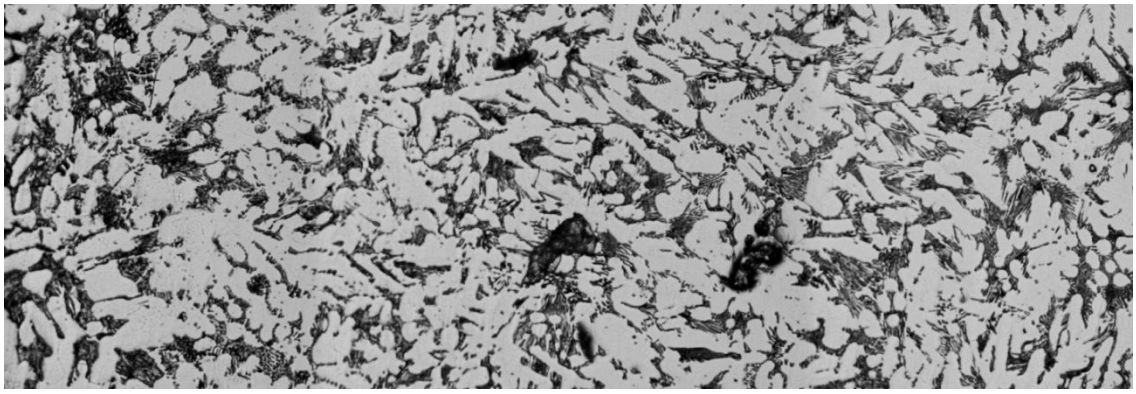

Figure 5-46: Edge of the wedge

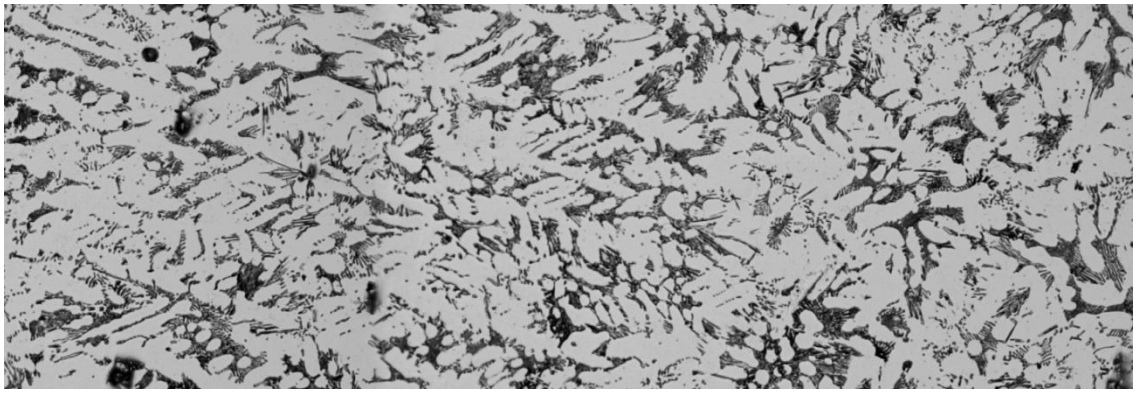

Figure 5-47: Columnar to equiaxed transition

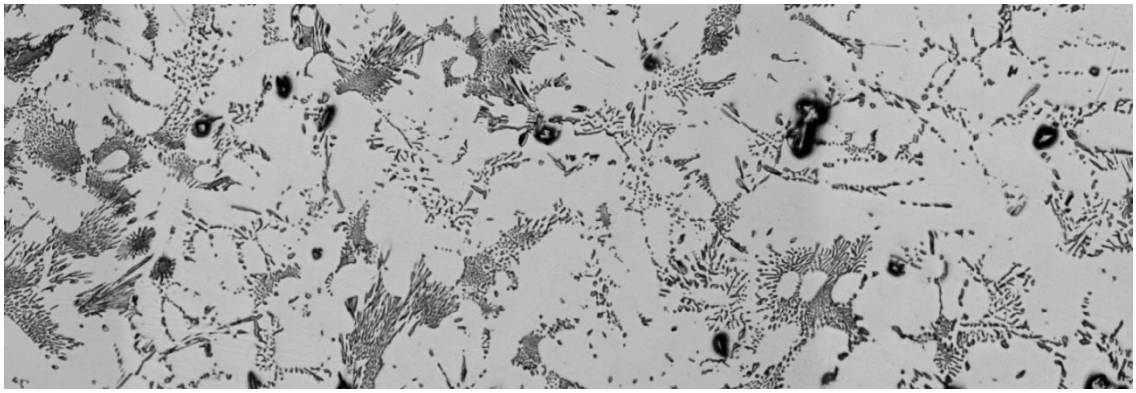

Figure 5-48: Center of the wedge

AE44 location 5

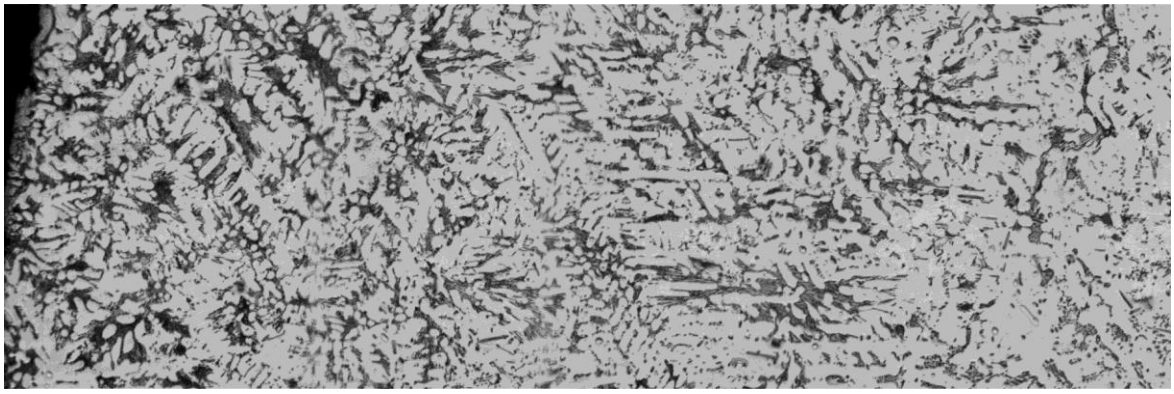

Figure 5-49: Edge of the wedge

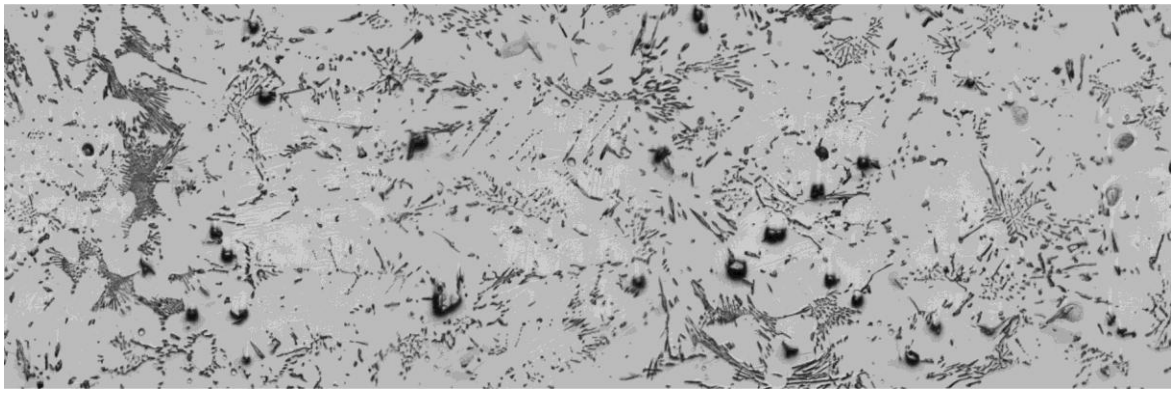

Figure 5-50: Columnar to equiaxed transition

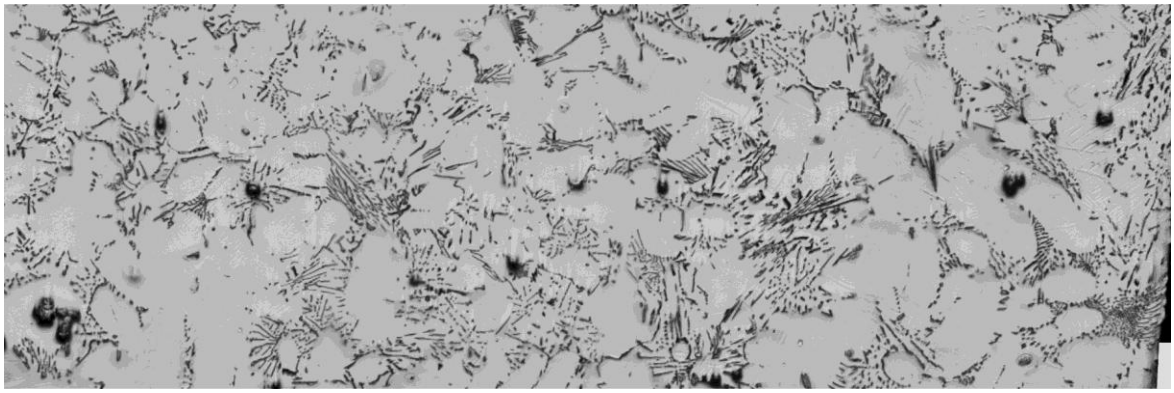

Figure 5-51: Center of the wedge

AE44 location 6

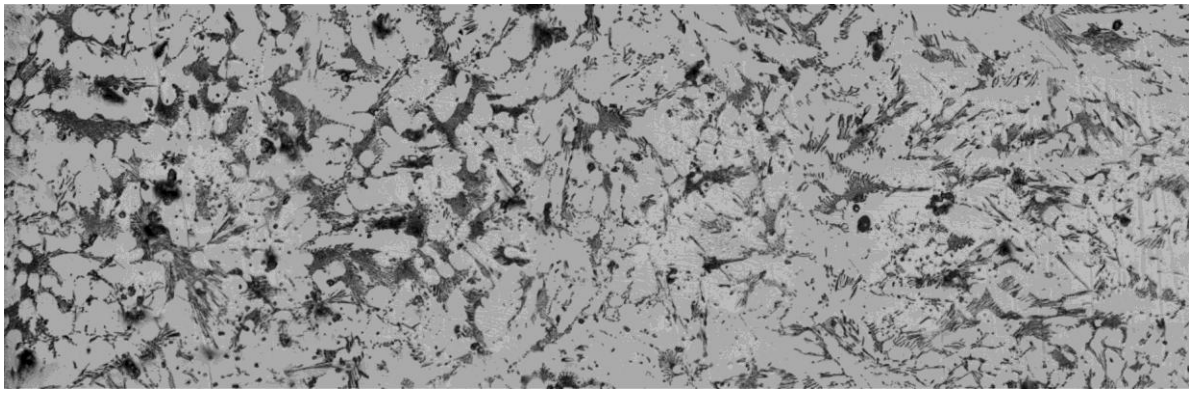

Figure 5-52: Edge of the wedge

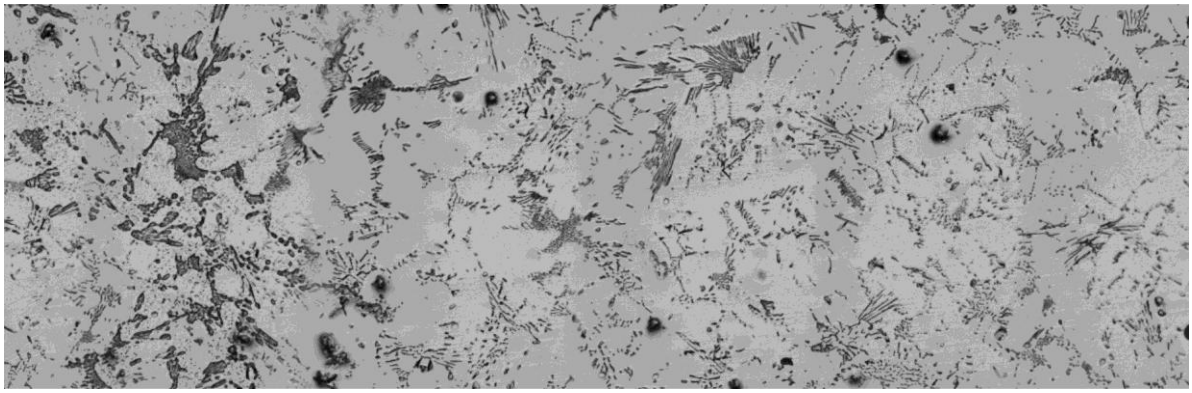

Figure 5-53: Columnar to equiaxed transition

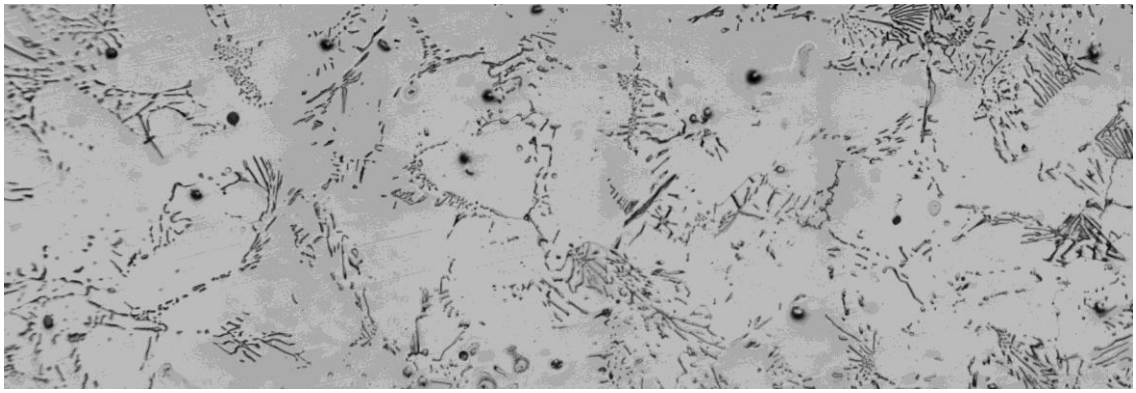

Figure 5-54: Center of the wedge

A.4 Particle distribution in AZ91D alloy

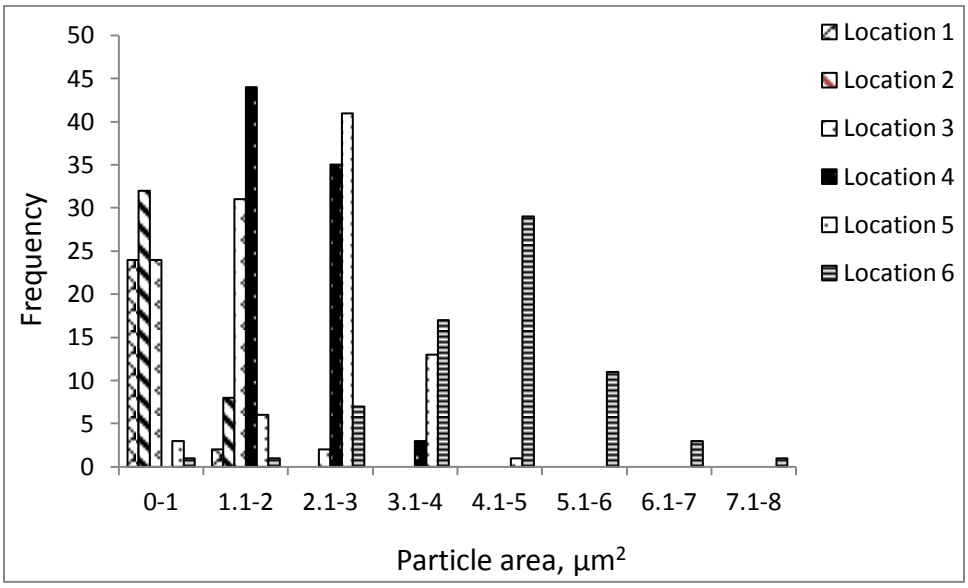

Figure 5-55: Average particle area distribution for AZ91D alloy in different wedge locations

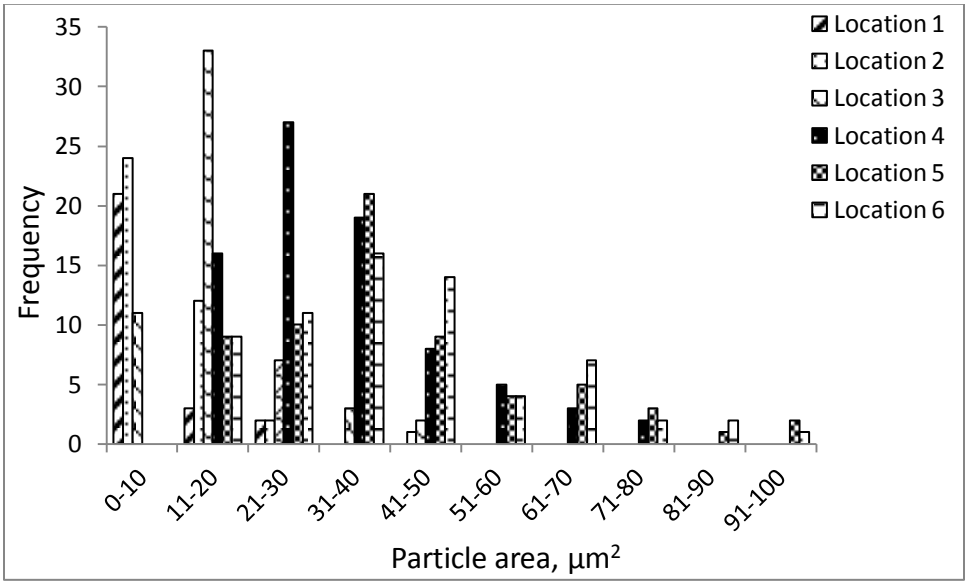

Figure 5-56: Large particle area distribution for AZ91D alloy in different wedge locations

A.5 Particle distribution in AM60B alloy

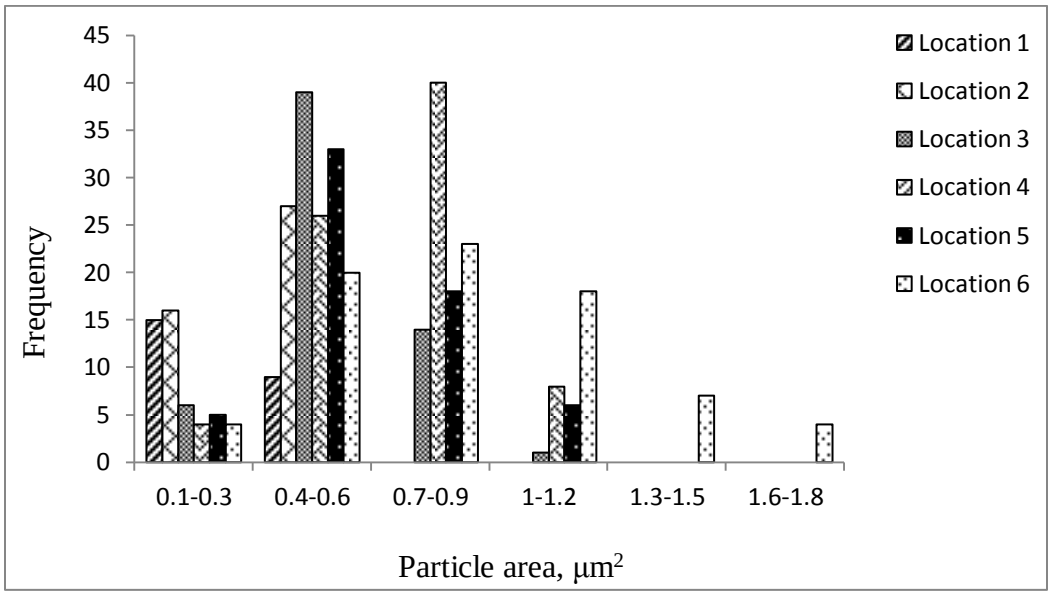

Figure 5-57: Average particle area distribution in different locations of wedge of AM60B alloy

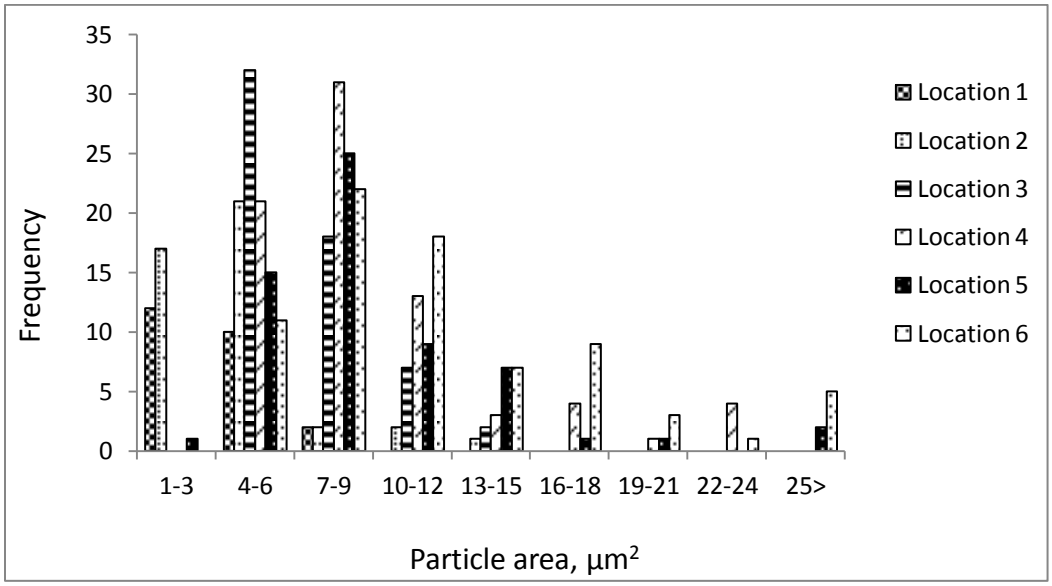

Figure 5-58: Large particle area distribution at different locations of the wedge of AM60B alloy

A.6 Particle distribution in AE44 alloy

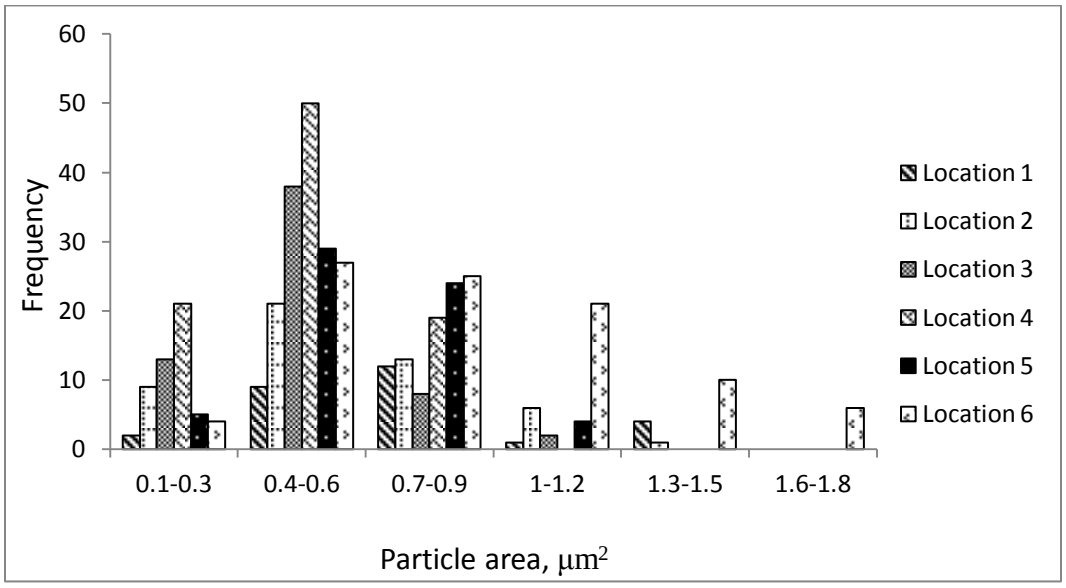

Figure 5-59: Distribution of average particle area in different locations of wedge of AE44 alloy

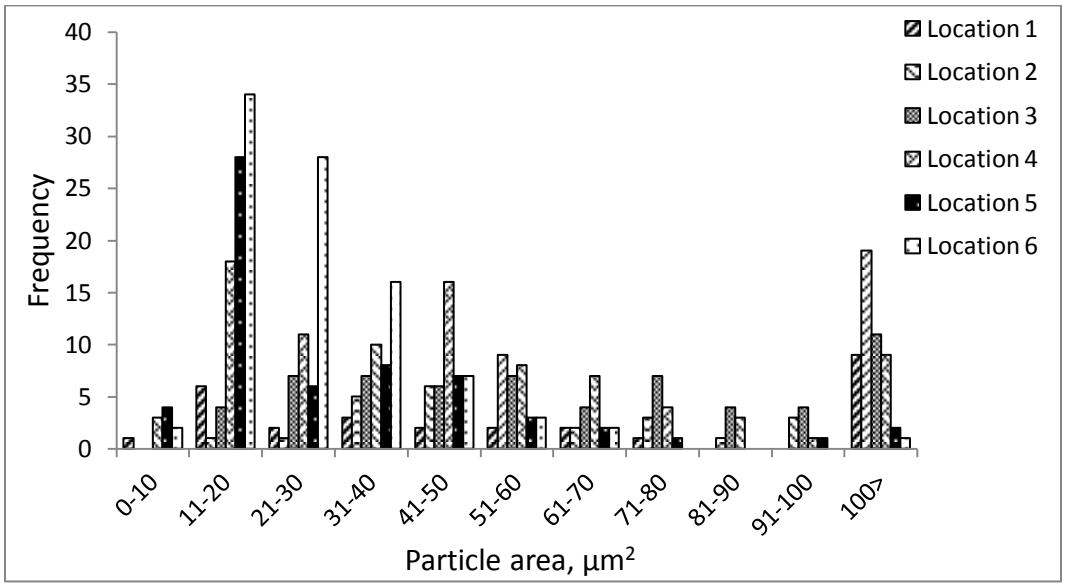

Figure 5-60: Distribution of large particle area at different locations in the wedge of AE44 alloy

A.7 Solute redistribution in AZ91D alloys

Location 2

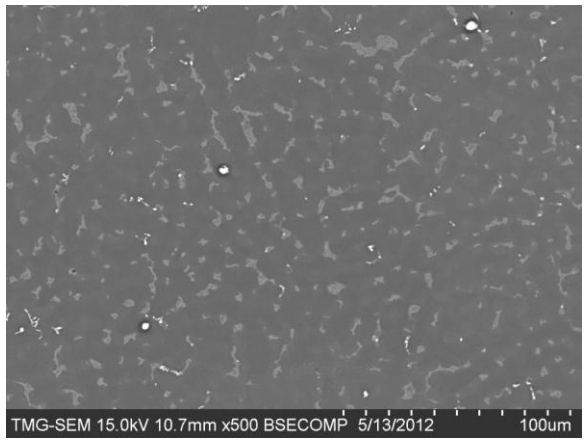

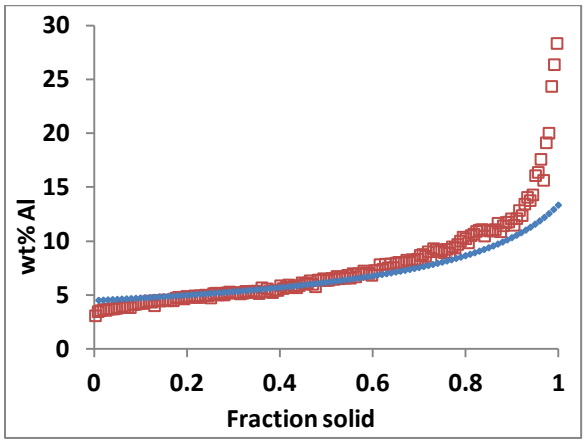

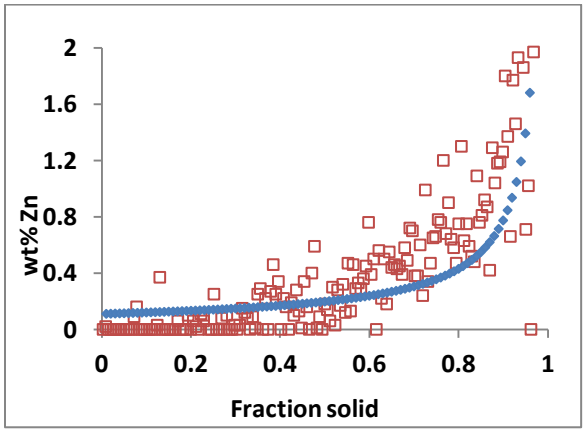

Figure 5-61: Solute redistribution in location 2

Location 3

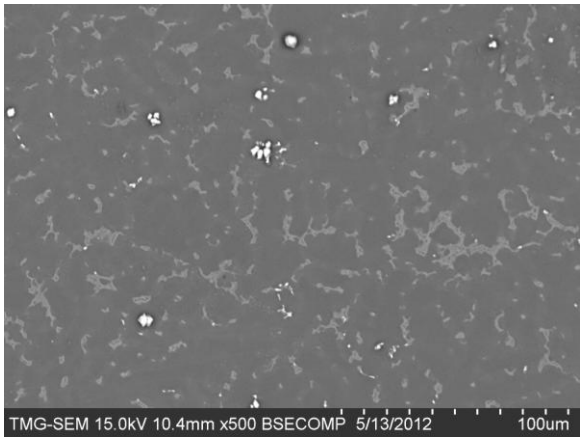

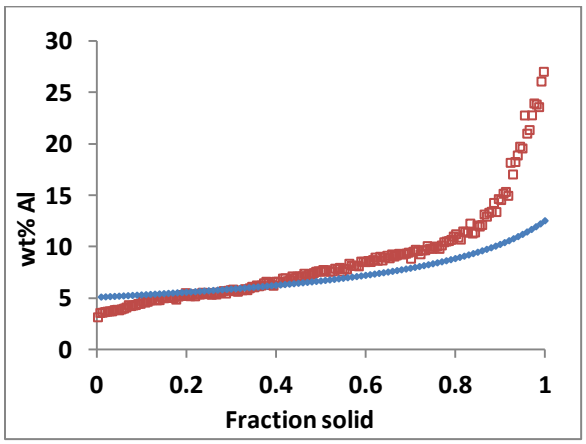

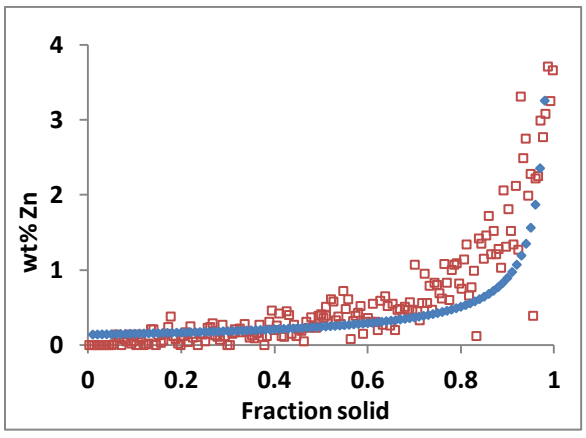

Figure 5-62: Solute redistribution in location 3

Location 4

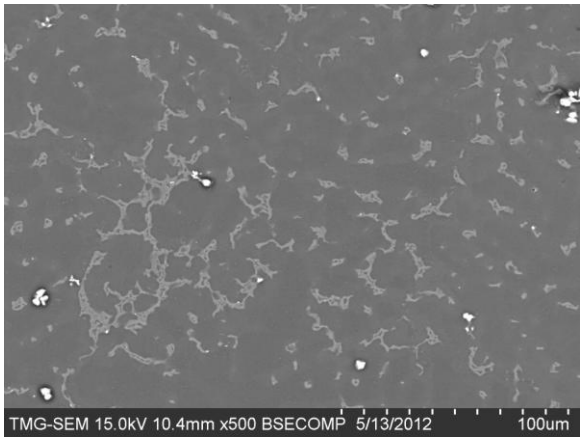

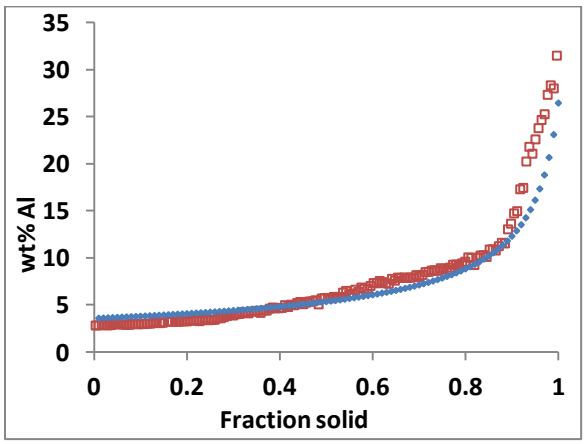

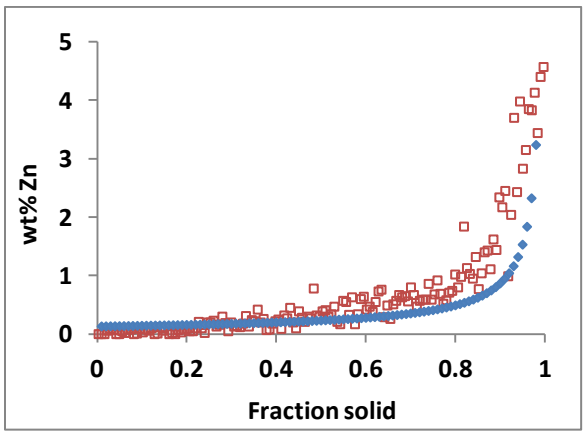

Figure 5-63: Solute redistribution in location 4

Location 5

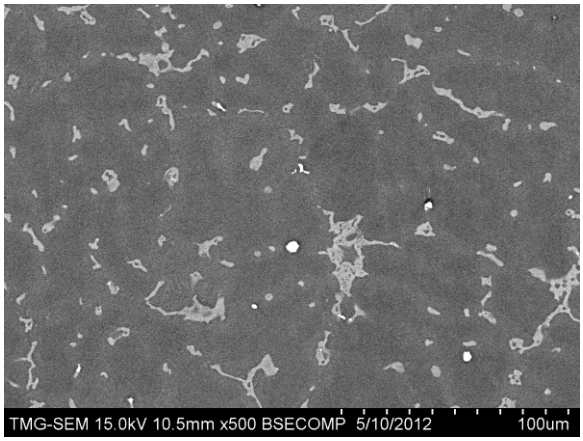

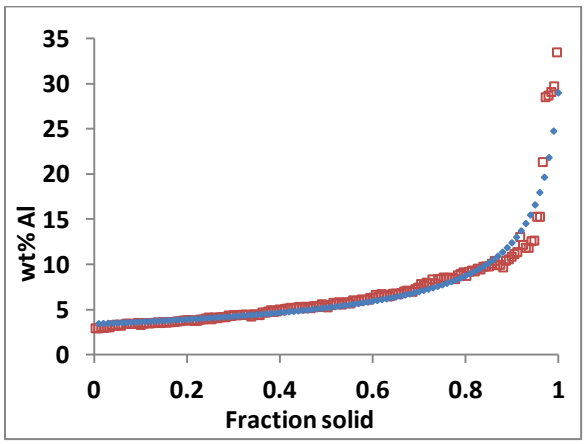

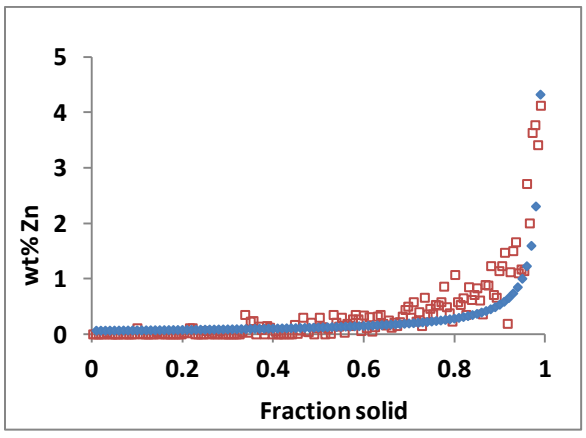

Figure 5-64: Solute redistribution in location 5

Location 6

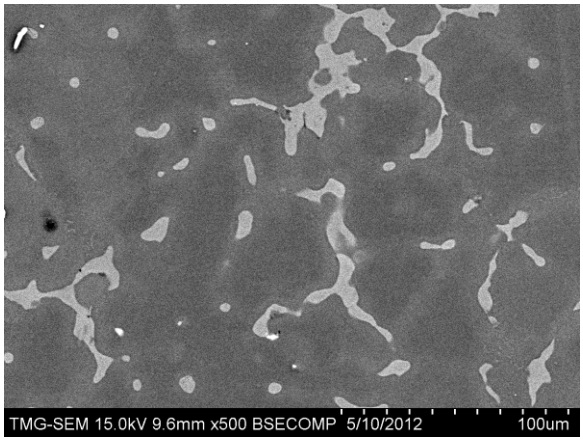

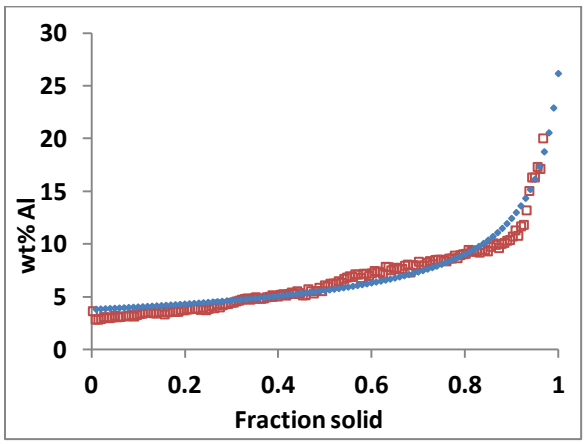

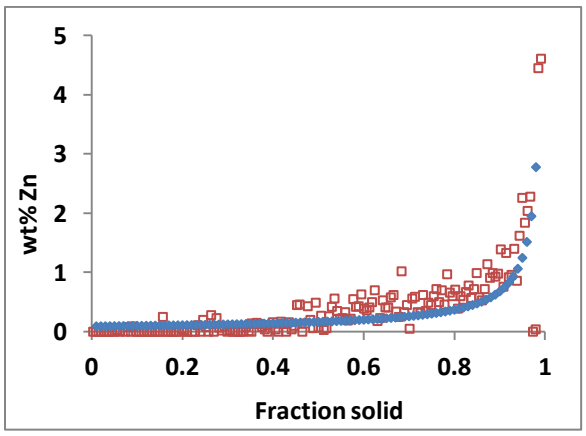

Figure 5-65: Solute redistribution in location 6

A.8 Solute redistribution in AM60B alloy

Location 2

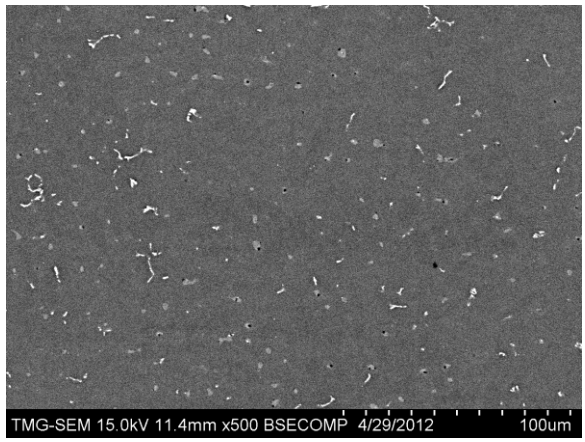

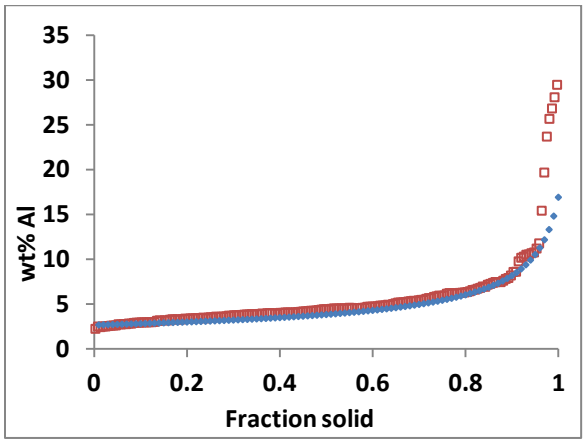

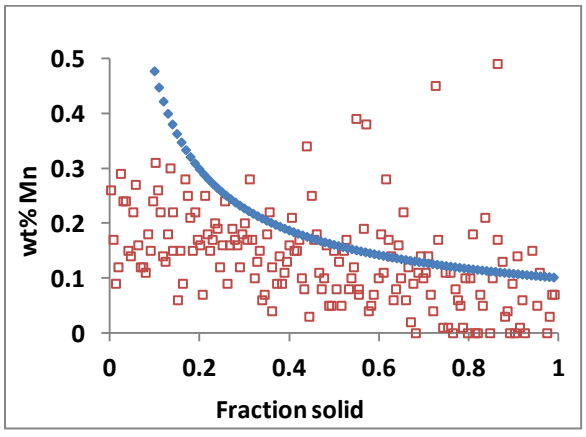

Figure 5-66: Solute redistribution in location 2

Location 3

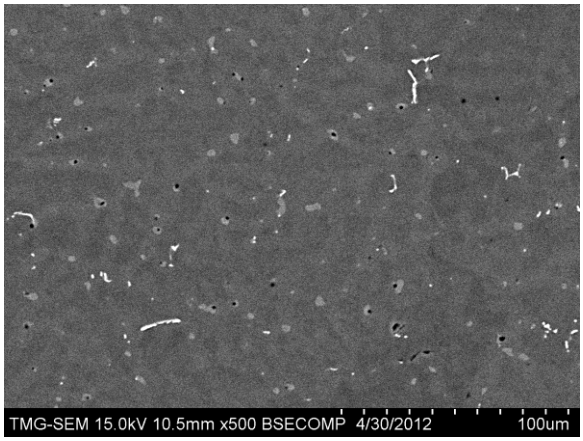

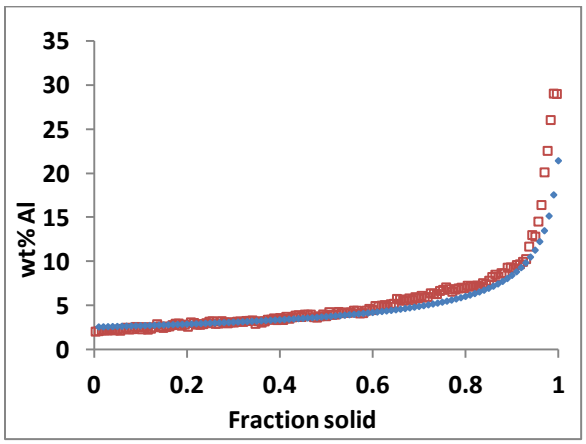

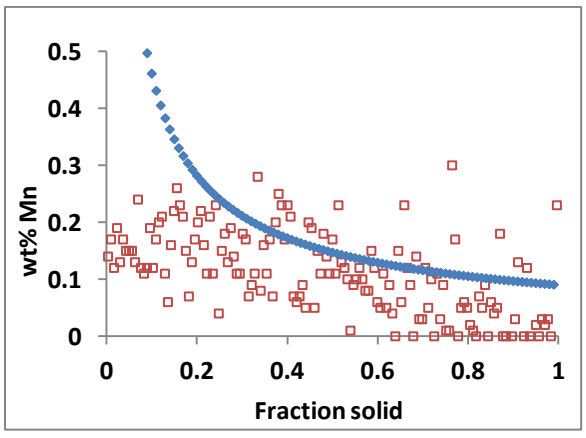

Figure 5-67: Solute redistribution in location 3

Location 4

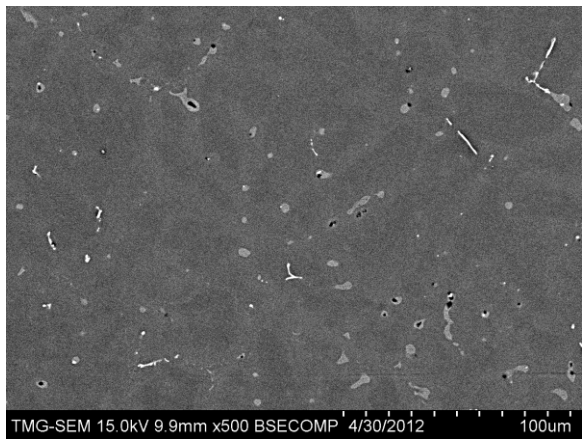

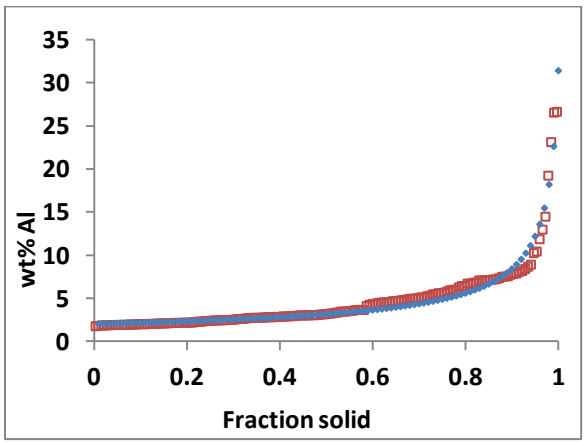

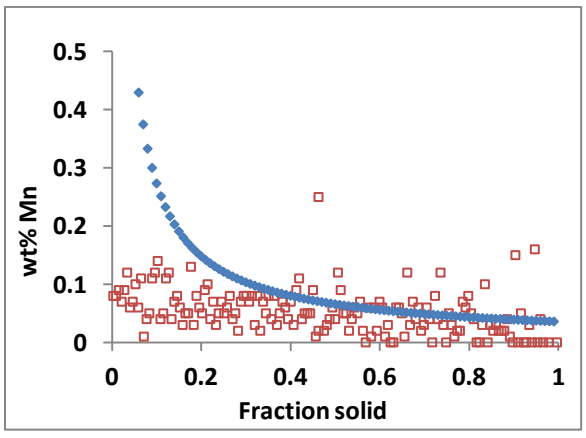

Figure 5-68 : Solute redistribution in location 4

Location 5

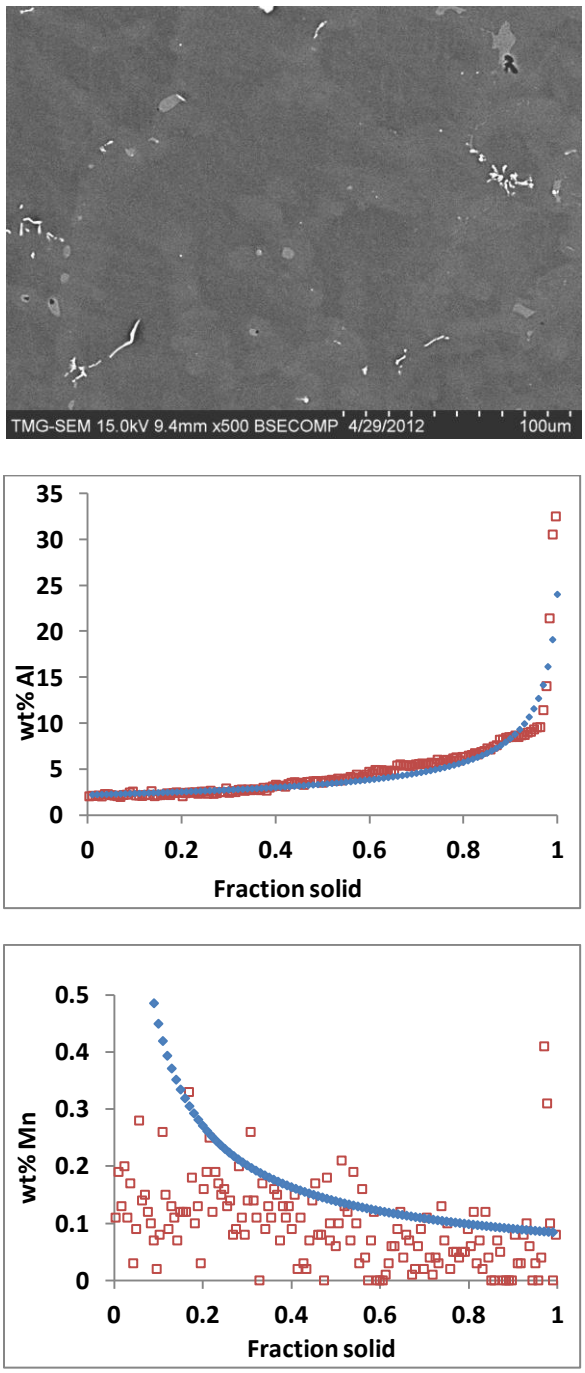

Figure 5-69 : Solute redistribution in location 5

Location 6

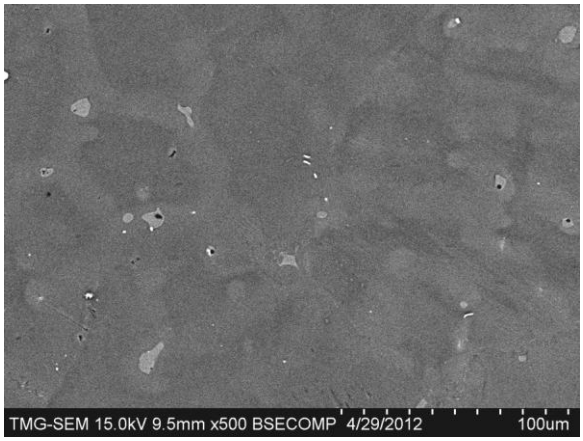

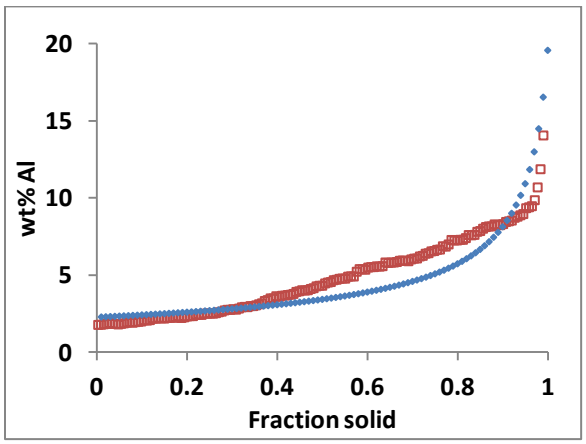

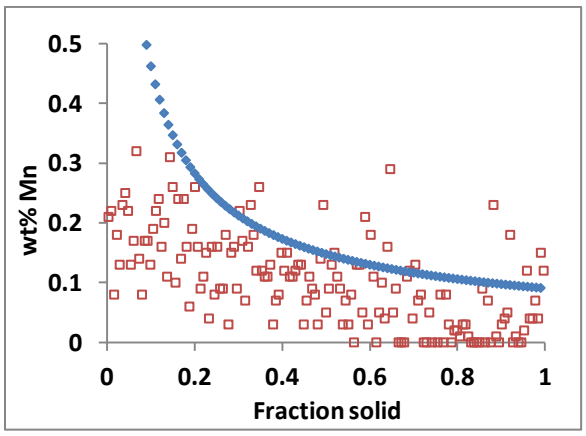

Figure 5-70: Solute redistribution in location 6

A.9 Solute redistribution in AE44 alloy

Location 2

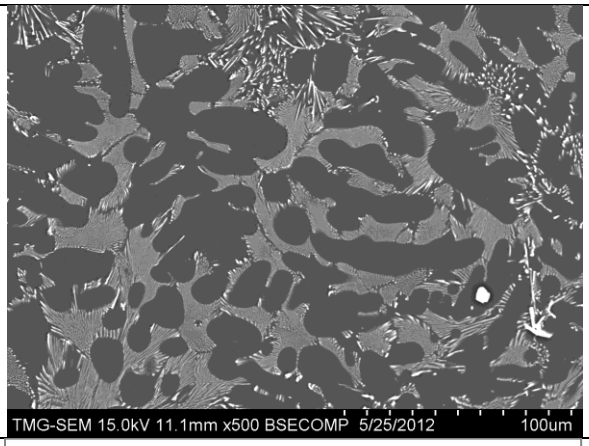

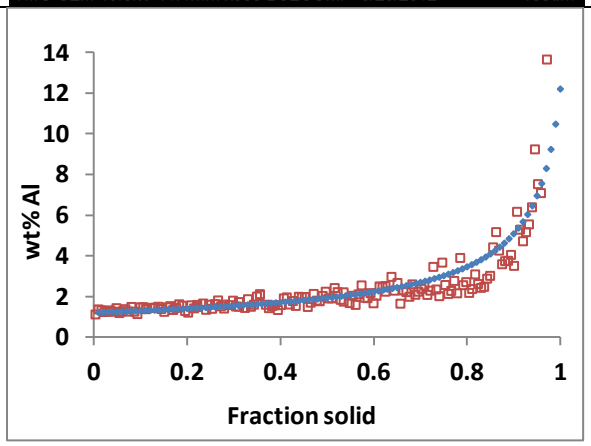

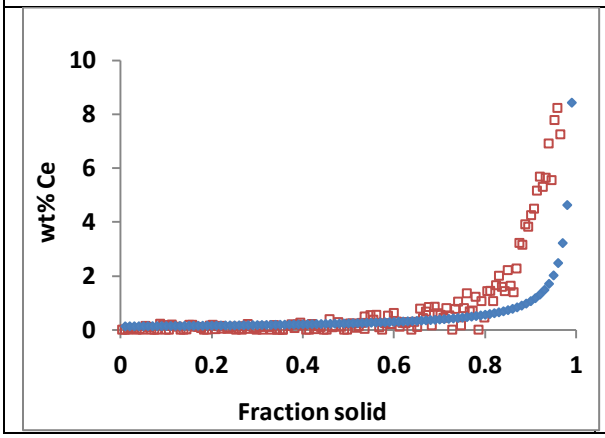

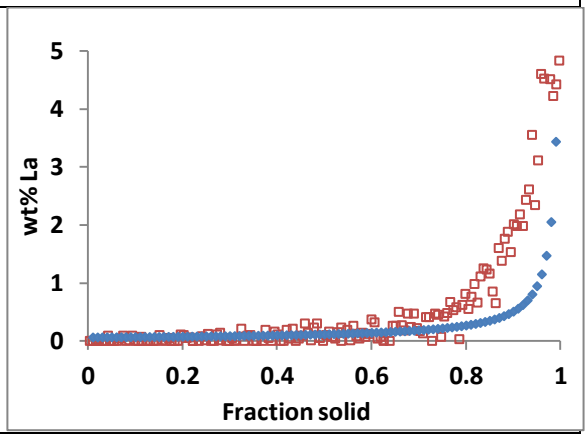

Figure 5-71: Solute redistribution in location 2

Location 3

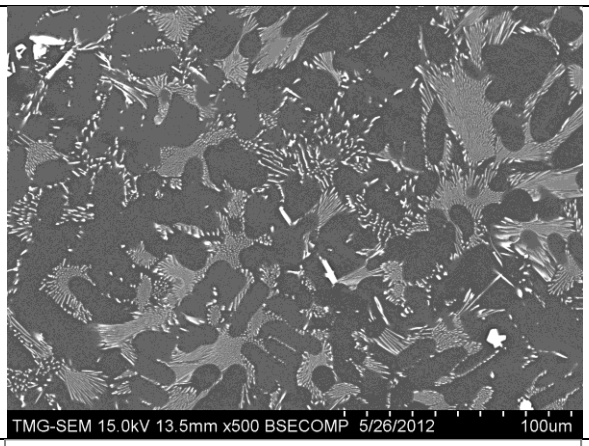

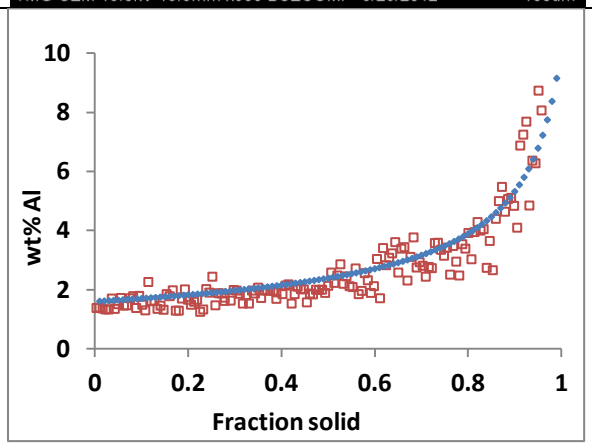

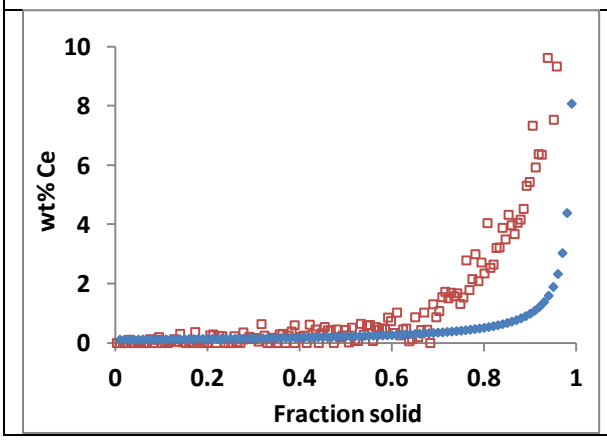

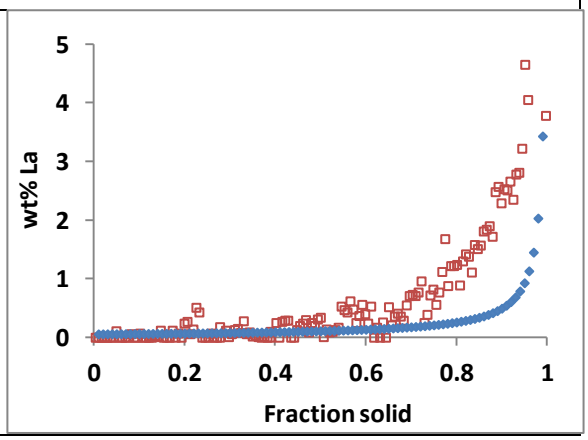

Figure 5-72: Solute redistribution in location 3

Location 4

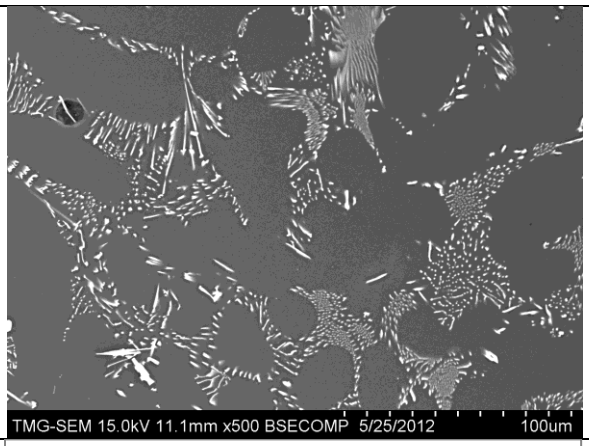

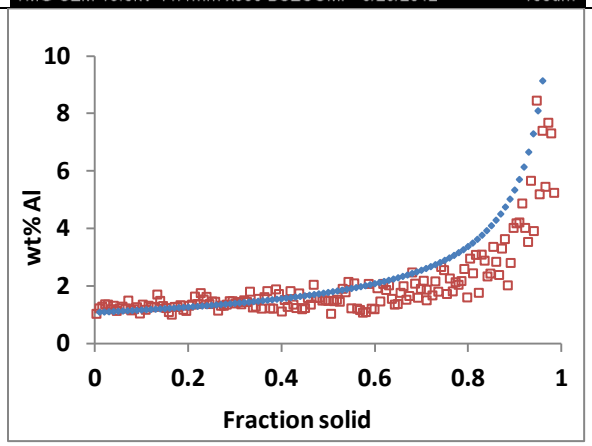

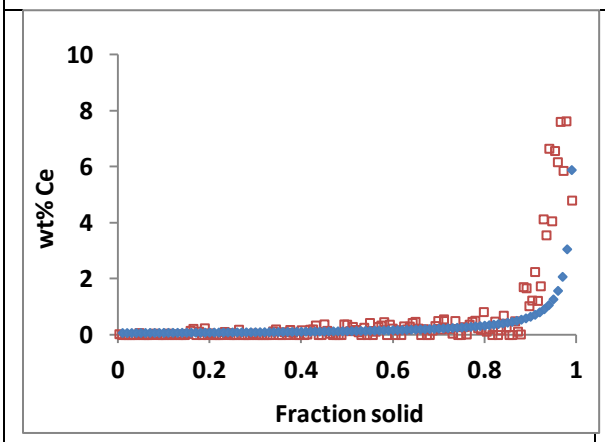

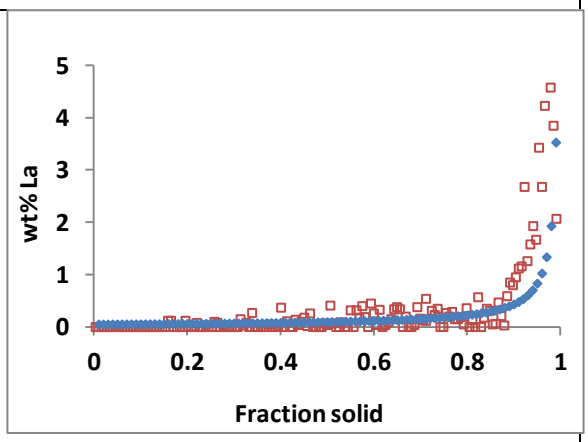

Figure 5-73: Solute redistribution in location 4

Location 5

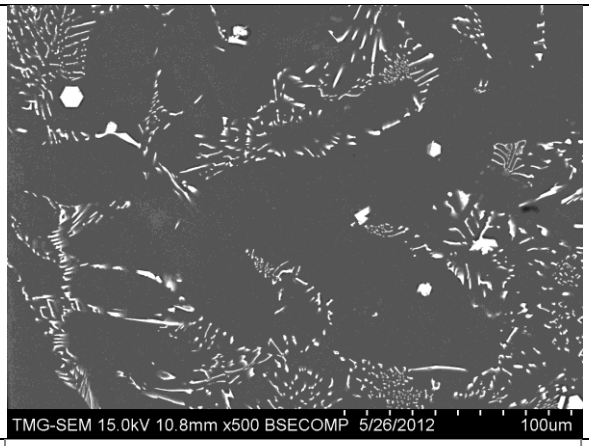

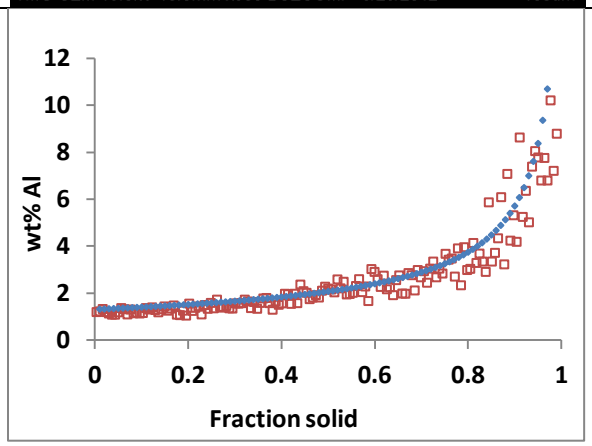

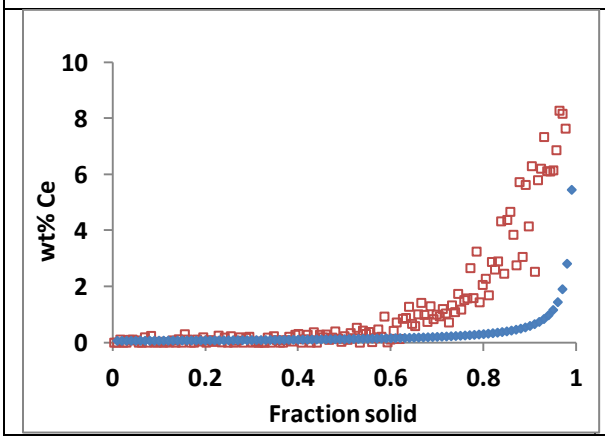

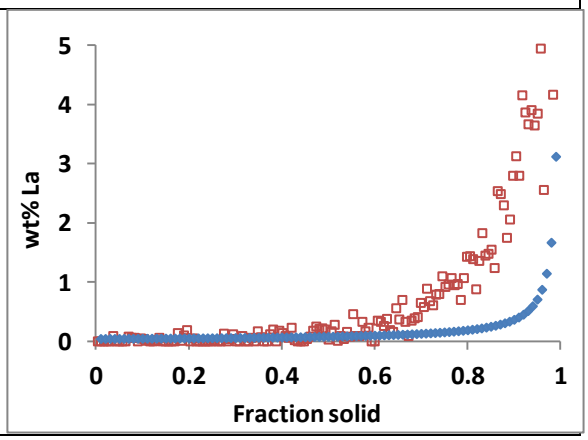

Figure 5-74 : Solute redistribution in location 5

Location 6

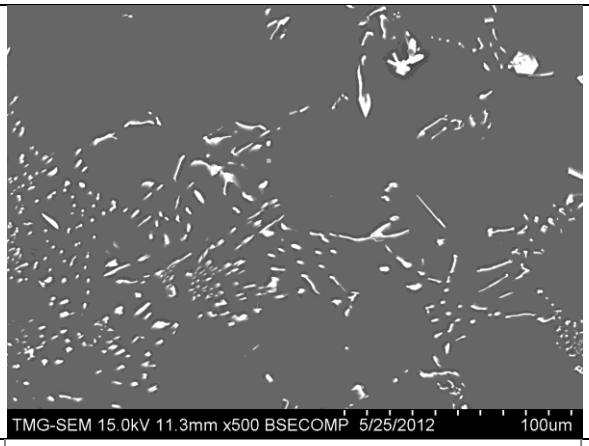

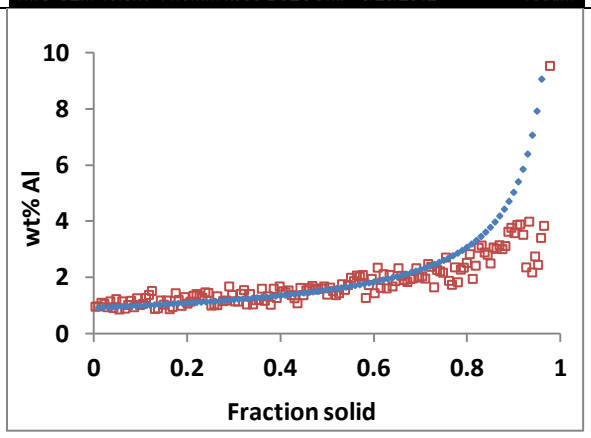

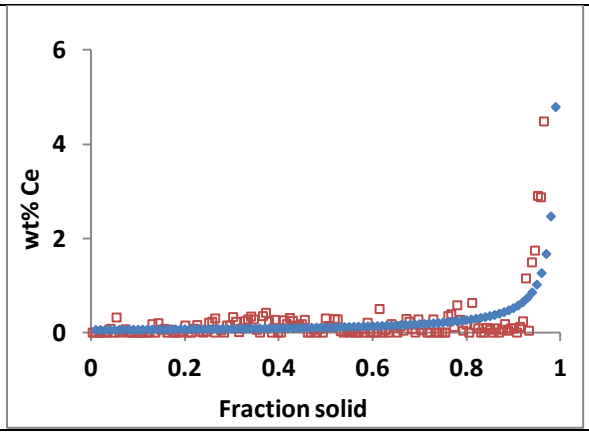

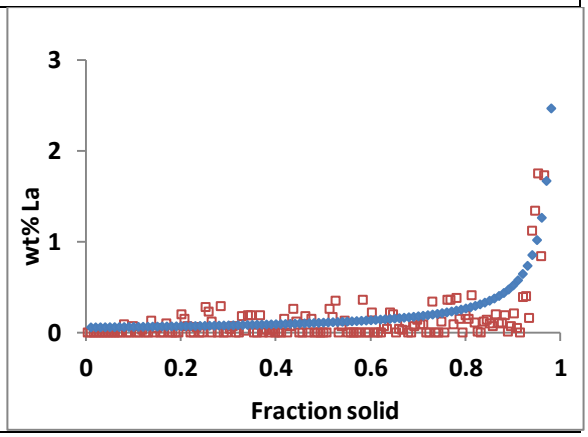

Figure 5-75: Solute redistribution in location 6

A.10 Microhardness measurement across the sample for AZ91D alloy

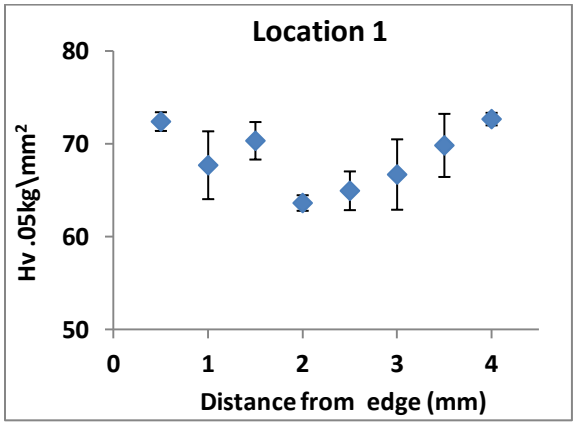

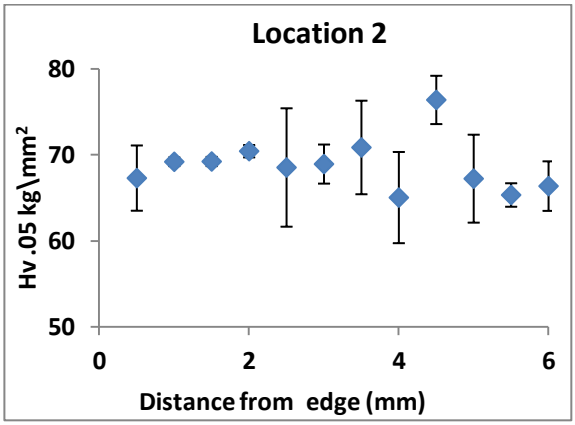

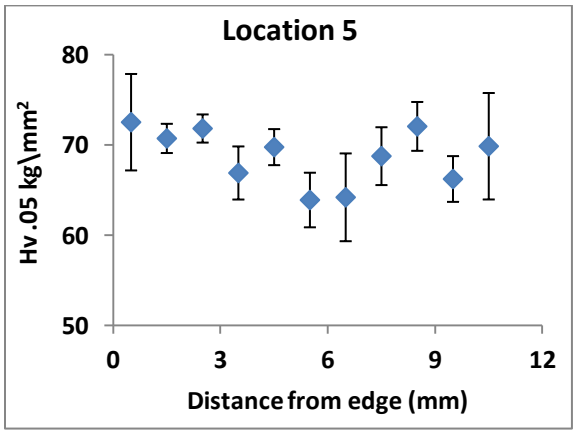

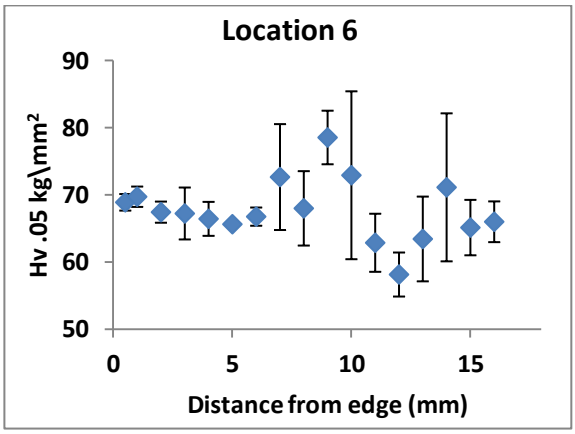

A.11 Microhardness measurement across the sample for AM60B alloy

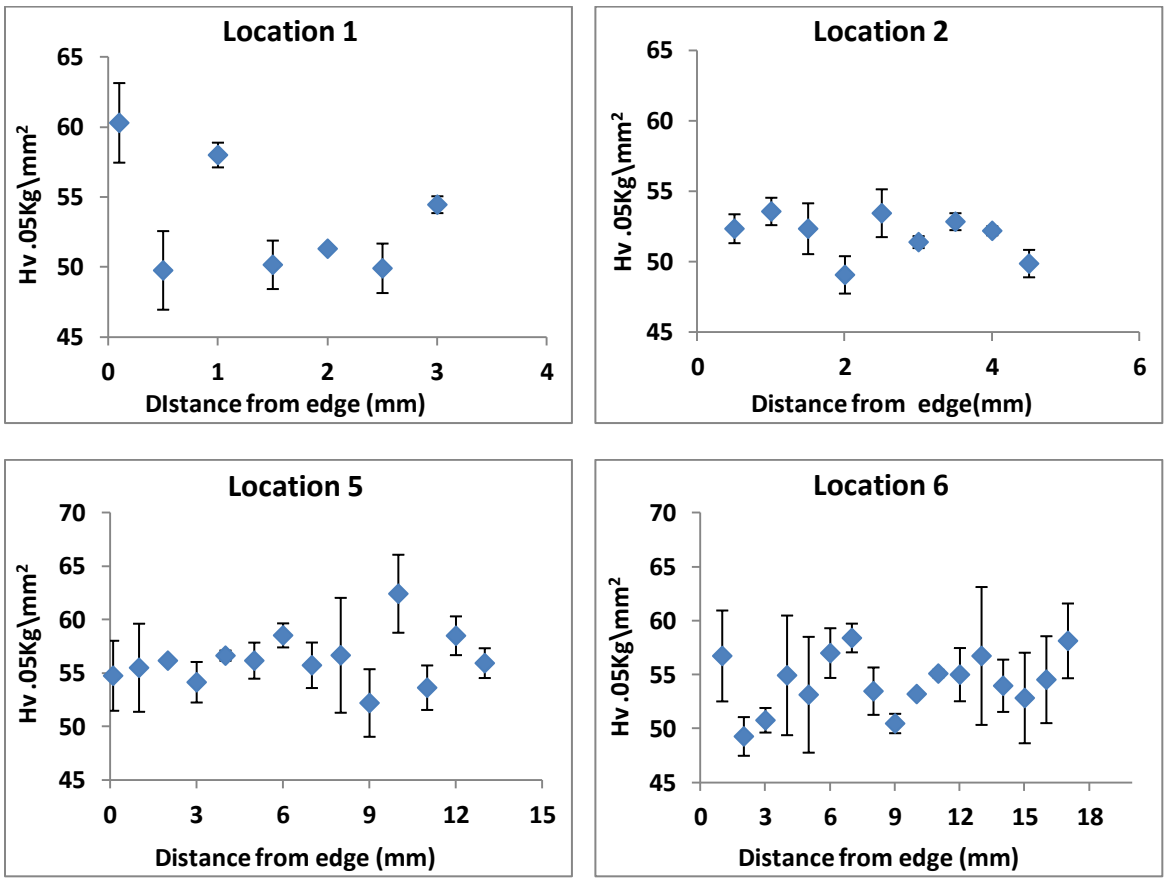

A.12 Microhardness measurement across the sample for AE44 alloy